POLITECNICO
MILANO 1863

SCUOLA DI INGEGNERIA INDUSTRIALE
E DELL'INFORMAZIONE

Mid-fidelity aerodynamic analysis and design of a fixed-wing eVTOL for the Martian atmosphere

Tesi di Laurea Magistrale in
Aeronautical Engineering - Ingegneria Aeronautica

Author: **Christian Bonaventura**

Student ID: 214652
Advisor: Prof. Alberto Guardone
Academic Year: 2023-2024

Abstract

A mid-fidelity aerodynamic model is adopted for the assessment of the preliminary design of a fixed-wing eVTOL UAV operating in the Martian atmosphere. The present work targets the design of specific rotors and the evaluation of the UAV performance during hover, transition, and cruise phases, with a thorough examination of the aerodynamic loads. The propulsive system has been optimized to meet the operational requirements of a 20 kg drone capable of traveling up to 70 km on Mars. Additionally, the stability of the drone has been assessed, as well as the potential impact of aeroelastic phenomena on the wing structure in Martian atmospheric conditions. The results indicate that developing a drone for operations on Mars represents a significant challenge, particularly regarding batteries and structural materials. Nevertheless, this goal is achievable in the coming decades with continuous technological advancements. The development of such drones is essential for the success of future exploratory missions, opening new opportunities for scientific breakthroughs.

Keywords: Mars, Martian atmosphere, eVTOL, UAV

Abstract in lingua italiana

Questa tesi si colloca nel contesto del crescente interesse verso l'esplorazione di Marte, proponendo un approccio a media fedeltà per il design preliminare di un eVTOL UAV ad ala fissa, progettato per operare nell'atmosfera marziana. Continuando il lavoro di due tesi precedenti, sono stati progettati rotori specifici e analizzate le fasi di hover, transizione e crociera, accompagnate da un'analisi approfondita dei carichi aerodinamici. È stata necessaria l'ottimizzazione del sistema propulsivo per soddisfare i requisiti operativi di un drone del peso di circa 20 kg, capace di coprire distanze fino a 70 km su Marte. Successivamente, è stata valutata la stabilità del drone e l'impatto di possibili fenomeni aeroelastici sulla struttura dell'ala in condizioni atmosferiche marziane. I risultati ottenuti evidenziano che lo sviluppo di un drone per l'operatività su Marte rappresenta una sfida significativa, richiedendo l'adozione di batterie e materiali all'avanguardia. Tuttavia, con i continui progressi tecnologici, questo obiettivo appare sempre più realizzabile nei prossimi decenni. La costruzione di tali droni è essenziale per il successo delle future missioni esplorative, aprendo nuove opportunità per scoperte scientifiche rilevanti.

Parole chiave: Marte, atmosfera marziana, eVTOL, UAV

Contents

Abstract **i**

Abstract in lingua italiana **iii**

Contents **v**

1 Introduction **1**
1.1 Martian environment 2
1.1.1 General overview 2
1.1.2 Atmospheric model 4
1.2 Overview of previous works 6
1.3 Goals 8

2 Numerical modeling **11**
2.1 DUST 11
2.2 MBDyn 11
2.3 UAV modeling 11
2.3.1 CAD model 12
2.3.2 Surface mesh 13

3 Isolated rotor design **17**
3.1 Thrust requirements 17
3.2 Preliminary sizing 17
3.3 Rotor solidity and blade average lift coefficient 18
3.4 Blade twist angle and rotor collective pitch angle 20
3.5 Blade planform and chord distribution 20
3.6 Blade Reynolds and Mach numbers 22
3.7 Blade airfoils 23
3.8 DUST model 25

3.9 Time and spatial convergence at hovering . . . 26
3.10 Cruise . . . 32
3.11 Transition . . . 36

4 Full model aerodynamic analysis 47
4.1 Rotors positioning . . . 47
4.2 Trim settings . . . 49
4.3 Thrust, torque, and shaft power analysis . . . 50
4.4 Airplane mode - Cruise . . . 52
4.4.1 Loads on the wing . . . 52
4.4.2 Loads on the rotors . . . 54
4.5 Transition mode . . . 56
4.6 Helicopter mode - Hover . . . 58

5 Propulsive system 61

6 Stability analysis 69
6.1 Numerical model . . . 69
6.2 Calculation of static stability derivatives . . . 71
6.2.1 Static angle of attack . . . 71
6.2.2 Static angle of sideslip . . . 72
6.3 Calculation of dynamic stability derivatives . . . 73
6.3.1 Roll oscillation . . . 73
6.3.2 Pitch oscillation . . . 75
6.3.3 Yaw oscillation . . . 77
6.3.4 Vertical plunge oscillation . . . 79
6.3.5 Lateral plunge oscillation . . . 80
6.4 Eigenvalues and flying qualities . . . 80

7 Aeroelastic analysis 85
7.1 DUST - MBDyn coupling . . . 85
7.2 Structural characteristics . . . 85
7.3 Coupled model . . . 88
7.4 Results . . . 89

8 Conclusions and future developments 93

Bibliography 95

A Empirical extension of lift, drag, and pitching moment coefficients **99**

B MIL-STD - Flying qualities **103**

List of Figures **107**

List of Tables **111**

List of Symbols **113**

1 Introduction

Back in 1971, NASA started the Mars Exploration Program with the Mars Mariner Missions and is currently active with the Mars 2020: Perseverance Rover Mission. This last mission seeks signs of ancient life on Mars and hopes to take several samples of rocks and terrain back to Earth. The peculiarity of the Perseverance Rover Mission is the employment of the first rotorcraft ever used on Mars and out of the Terrestrial atmosphere, Ingenuity (Figure 1.1), to explore surrounding areas. The helicopter successfully performed 72 flights in 3 years, for about 128 minutes and 11 miles, exceeding all expectations [20].

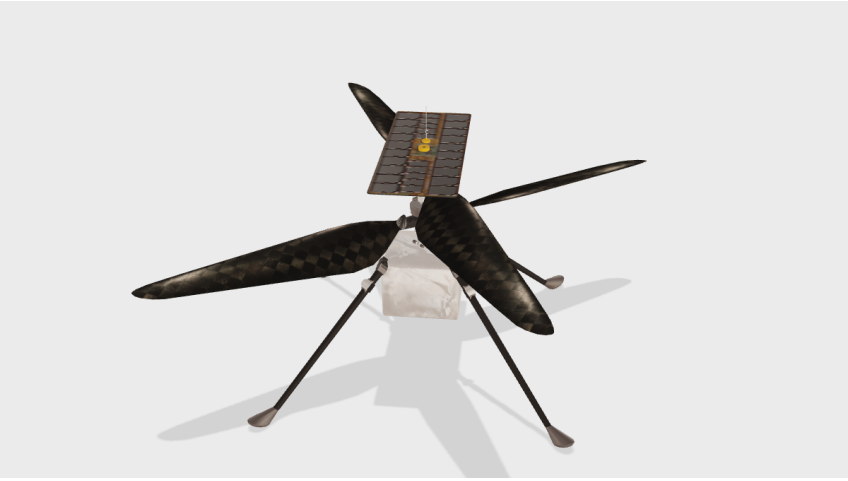

Figure 1.1: Ingenuity Mars Helicopter [20]

Ingenuity UAV consists of two contra-rotating rotors of approximately 1.2 m diameter, which provide vertical and horizontal thrust, a solar panel to recharge the battery pack, sensors and cameras stored inside a cubic fuselage, and four legs. According to NASA, the state-of-the-art technology was used to minimize the overall mass (1.8 kg) and dimensions, leading to a production cost of about 81 million dollars. 2.7 billion dollars is instead the estimated cost of the entire mission [20].

1.1. Martian environment

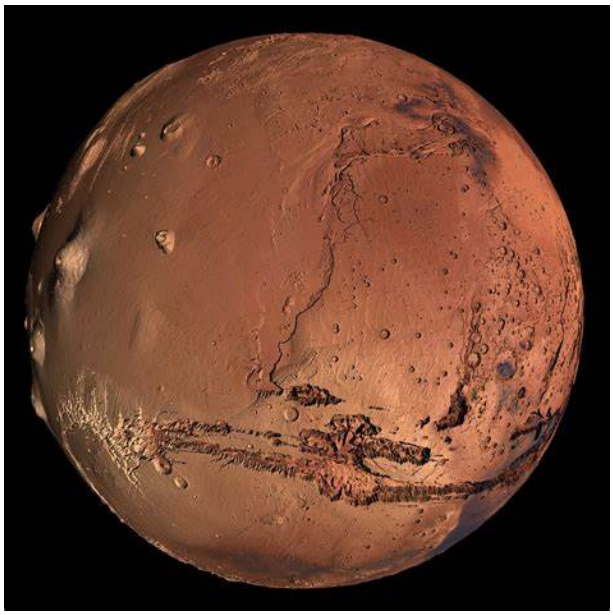

Figure 1.2: Mars

1.1.1. General overview

Mars, often referred to as the "Red Planet" due to the vast amount of ferric oxide dust on its surface, is the fourth planet from the Sun, located at an average distance of 228 million km, and the second smallest planet of the entire Solar System. With a diameter of approximately 6,779 km, it is about half the size of the Earth.

Its orbital period is approximately 687 Earth days, nearly twice as long as a year on Earth, while a Martian day lasts 24.6 hours. The axial tilt is about 25.2°, similar to Earth's 23.5° tilt, giving it seasonal changes similar to those on Earth, although Martian seasons last nearly twice as long due to its extended year.

Mars has two natural moons called Phobos and Deimos. Both have irregular shapes, resembling other asteroids in the Solar System. Phobos, the largest one, measures about 22 km at its widest point and orbits Mars at a very close distance of approximately 6,000 km in 7 hours and 39 minutes. Deimos has an average diameter of about 12 km and orbits Mars at 23,500 km in approximately 30 hours.

The Red Planet is classified as a terrestrial planet primarily composed of silicate, rocks, and metals. Like Earth, Mars' internal structure is divided into layers. The outermost layer, the crust, is, on average, 42-56 km thick, with a minimum of 6 km in the plain

Isidis Planitia and a maximum of 117 km in the volcanic plateau Tharsis. The most abundant elements in the Martian crust are silicon, oxygen, iron, magnesium, aluminum, calcium, and potassium. So far, no samples of Martian soil have been returned to Earth but have only been analyzed in situ with rovers. However, the goal remains to carry out a sample-return mission successfully.

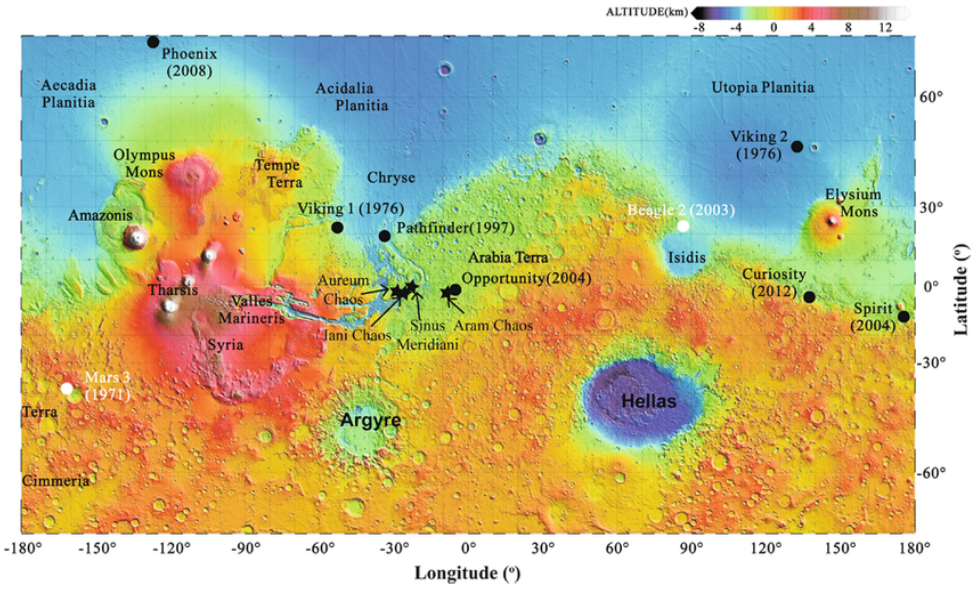

Figure 1.3: Mars topographic map

The surface of Mars features a massive presence of volcanoes such as Olympus Mons, Mars's tallest volcano, with its 21.9 km height. In the southern hemisphere, Hellas Planitia is a meteoritic crater extending over 2,300 km from east to west and 7 km in depth. Planum Boreum and Planum Australe are the two polar plains covered by seasonal polar ice caps made of frozen water and frozen carbon dioxide.

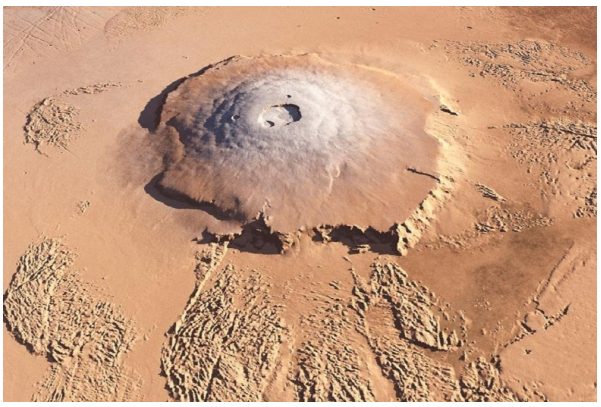

(a) Olympus Mons

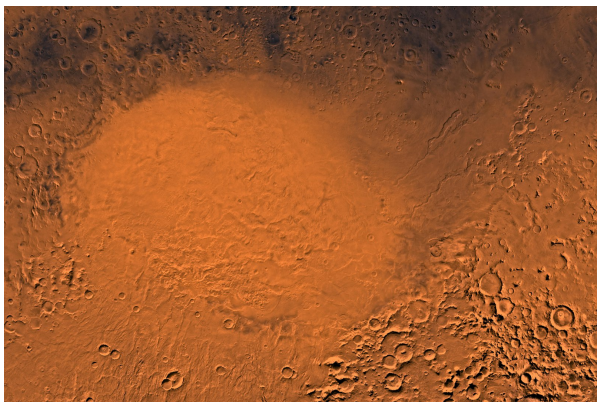

(b) Hellas Planitia

Figure 1.4: Mars main topographic features

The Red Planet mass is approximately $6.4 \cdot 10^{23}$ kg and the average density is 3.93 kg/m^3. It results in a gravity acceleration of approximately 3.72 m/s^2, 38% of the terrestrial gravity acceleration.

1.1.2. Atmospheric model

The atmosphere of Mars is primarily composed of carbon dioxide, making up about 95.1% of its volume, with minor amounts of nitrogen (2.6%), argon (1.9%), and trace gases like oxygen and carbon monoxide.

With an average atmospheric pressure of only 610 Pa, less than 1% of Earth's at sea level, the atmosphere provides minimal protection from UV and radiation, posing challenges for potential human habitation. At the surface, it ranges from approximately 30 Pa at high altitudes like Olympus Mons to about 1,155 Pa at the deepest point, the Hellas Planitia.

The temperature on Mars varies significantly due to its thin atmosphere and low capacity to retain heat, from -125 °C at the poles in winter to around 20 °C near the equator during summer.

The atmospheric density is also very low. The average value, slightly affected by altitude and temperature, is approximately 0.0144 kg/m^3, 1.2% of Earth's at sea level.

Seasonal shifts are especially pronounced in the southern hemisphere, where Mars's elliptical orbit brings it closer to the Sun during southern summer, making this season significantly warmer. During this period, temperatures and solar heating increase, causing atmospheric expansion, dust storms, and changes in pressure. In winter, especially at the poles, the colder temperatures cause the carbon dioxide in the atmosphere to freeze and form polar ice caps. This seasonal ice deposition in colder seasons and sublimation in warmer seasons cause pressure fluctuations across the surface, affecting atmospheric circulation patterns and winds.

NASA developed a simple numerical model of the atmosphere of Mars [21] that has been implemented in MATLAB and adopted in this thesis. It is reported in Equation 1.1, Equation 1.2 and Equation 1.3.

$$\text{For } h \leq 7,000 \text{ m:} \begin{cases} T = -31 - 0.000998\, h \\ P = 0.699 \exp(-0.00009\, h) \end{cases} \tag{1.1}$$

$$\text{For } h > 7,000 \text{ m:} \begin{cases} T = -23.4 - 0.00222\, h \\ P = 0.699 \exp(-0.00009\, h) \end{cases} \tag{1.2}$$

$$\rho = \frac{P}{R_{gas}(T + 273.15)} \tag{1.3}$$

where h is the altitude in [m], T is the temperature in [°C], P is the pressure in [kPa] and R_{gas} is the gas constant in [kJ/kgK]. Accounting for the molecular weight of the Martian atmosphere, which is approximately 43.3 g/mol, R_{gas} is 0.1921.

The dynamic viscosity is only a function of the temperature, according to Sutherland's law expressed by Equation 1.4.

$$\mu = \mu_0 \left(\frac{T}{T_0}\right)^{\frac{3}{2}} \frac{(T_0 + S)}{(T + S)} \tag{1.4}$$

where μ is the dynamic viscosity in [Pas], T is the temperature in [K], μ_0 is a constant ($1.48 \cdot 10^{-5}$ Pas), T_0 is a constant (293.15 K) and S is a constant (240 K).

The trends of temperature, pressure, density and dynamic viscosity with changing altitude are illustrated in Figure 1.5.

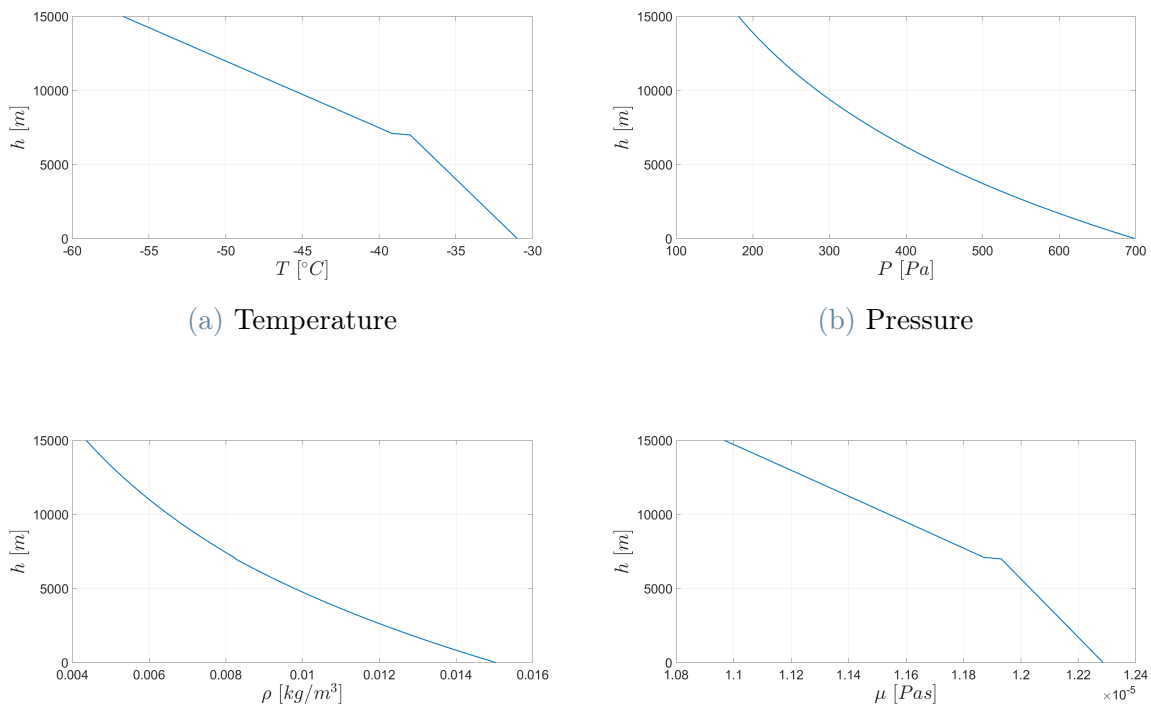

(a) Temperature

(b) Pressure

(c) Density

(d) Dynamic viscosity

Figure 1.5: Trends of atmospheric variables

With the assumption of a polytropic ideal gas, the speed of sound can be calculated with

the expression reported in Equation 1.5, with all parameters expressed in SI units.

$$c = \sqrt{\gamma R_{gas} T} \tag{1.5}$$

The carbon dioxide molecule is linear and can be therefore subject to three translational motions, two rotational motions and two vibrational motions (stretching and bending). According to the equipartition principle, the energy is equally distributed among the active modes. On Mars, with a low temperature and low pressure environment all the previous modes are excited. The specific heat ratio γ, namely the ratio between the isobaric and the isochoric specific heat, with active vibrational modes is hence equal to $\frac{9}{7}$, instead of $\frac{7}{5}$. The theoretical speed of sound calculated on the ground is 244 m/s, consistent with the 240 m/s obtained by NASA with experiments on Mars [17].

1.2. Overview of previous works

This thesis is the continuation of two previous works, which dealt with the conceptual and preliminary design of a fixed-wing eVTOL UAV for the Martian atmosphere [2] and the aerodynamic study and optimization of low-Reynolds 2D airfoils [19]. Firstly, a massive use of MATLAB [16] codes was made to impose performance requirements and design specifications, which have been gathered in Table 1.1 and Table 1.2 for completeness.

Performance requirement	Constraint
Stalling speed	$\leq$ 75 m/s
Cruising speed	$\geq$ 90 m/s
Take-off and landing	Vertical
Rate of climb	$\geq$ 22 m/s
Angle of climb	$\geq 12°$
Service ceiling	$\geq$ 3000 m
Limit load factor	$\geq$ 1.4

Table 1.1: Performance requirements

Design specification	Constraint
Maximum take-off mass	= 20 kg
Payload mass	= 2 kg
Range	$\geq$ 200 km
Wingspan	$\leq$ 3.5 m
Fuselage length	$\leq$ 4.0 m
Propulsion	Fully electric
Recharge time	$\leq$ 2 sols

Table 1.2: Design specifications

The payload mass consists of a miniaturized gas chromatograph (CG) and a mass spectrometer (MS), used to conduct experiments with samples collected on the ground, and possibly sensors and cameras for high-quality video recordings of the planet.

In [2], an optimal design point was retrieved using a Sizing Matrix Plot, with a wing

loading of 29.2 N/m^2 and a power loading of 0.021 N/W. Since the maximum take-off mass of the drone was fixed, it led to a wing surface of 2.53 m^2 and a maximum shaft power of 3,500 W. It is important to point out that the required shaft power at hovering was estimated with blade element and momentum theory, resorting to semi-empirical models from Stepniewsky [25]. In addition, only the number of rotors and their diameter were computed. After that, the battery pack and the solar panels were designed to meet the requirements of mission range and recharge time. Finally, the open-source software OpenVSP [18] was used to perform the mass breakdown, to estimate the aerodynamic characteristics of the drone and to check its static and dynamic stability.

In [19], the low-Reynolds Ishii airfoil was optimized through genetic algorithm and adjoint method with SU2 [11] software for several combinations of Reynolds and Mach numbers, to be used for both wing and rotor blades. An example of an optimized airfoil is shown in Figure 1.6 and Figure 1.7.

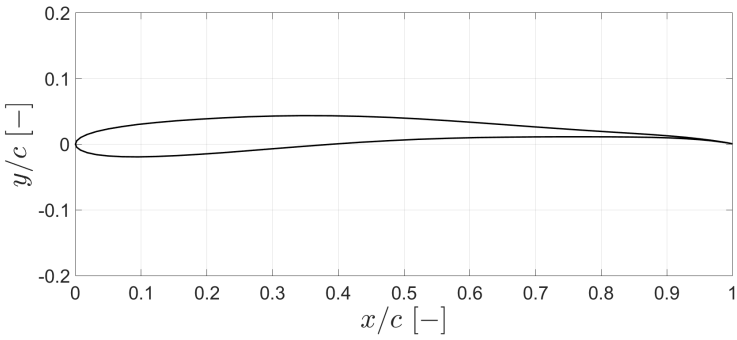

Figure 1.6: Airfoil optimized for Re = 10,000 and Ma = 0.6 - shape

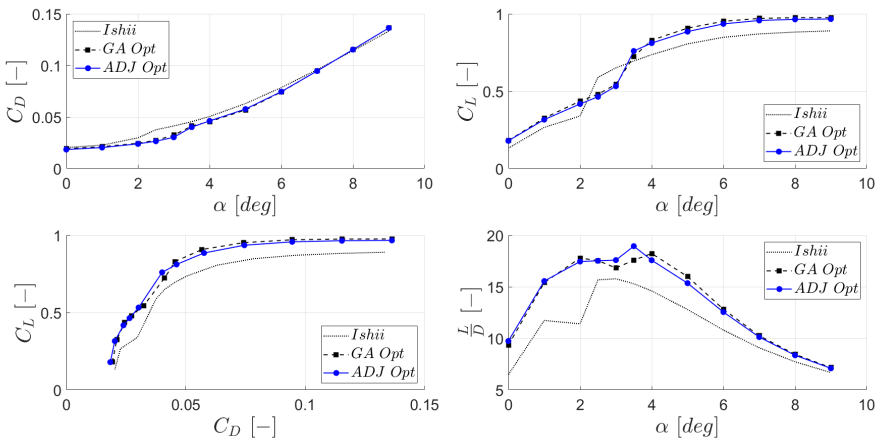

Figure 1.7: Airfoil optimized for Re = 10,000 and Ma = 0.6 - aerodynamic parameters

The preliminary configuration of the drone, which for different reasons has been subject to some changes during this work, is displayed in Figure 1.8.

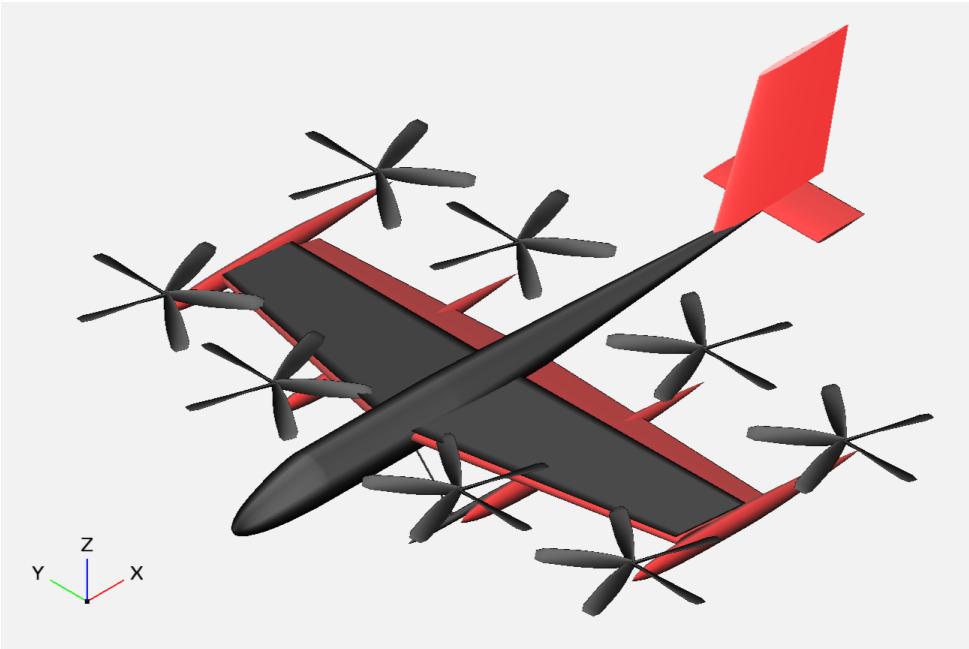

Figure 1.8: Preliminary configuration of the drone

With an estimated maximum lift-to-drag ratio of about 11, the mission range of the drone resulted in about 375 km, a very promising outcome.

1.3. Goals

The introduction of fixed-wing, electric vertical take-off and landing (eVTOL), unmanned aerial vehicles (UAV) may allow for exploring larger portions of Mars compared to a multi-rotor configuration, exploiting the enormous advantages of an airplane wing to conduct an efficient flight for greater distances and still taking off and landing vertically in almost every location. This thesis aims to consolidate the previous works' outcomes while introducing improvements and conducting further analyses to advance the project. Several aspects have been addressed

- design of fixed and tilting rotors with mid-fidelity approach
- full model aerodynamic analysis at hovering, transition, and cruising phases
- study of the loads generated by rotors and wing
- estimation of stability derivatives and flying qualities

- investigation of aeroelastic effects
- materials and propulsive system

2 | Numerical modeling

Different software tools have been used in the present work, including the mainstream open-source software OpenVSP [18] and Gmsh [9], commercial software MATLAB [16] and SolidWorks [6], and open-source software developed by Politecnico di Milano's Department of Aerospace Science and Technology, namely, DUST [5] and MBDyn [4], which have been extensively used in the present thesis.

2.1. DUST

DUST is intended to provide reliable solutions to complex configurations with interactional aerodynamics, such as the one occurring in the Martian drone. The core features of the software are the flexible definition of the geometry, from parametric definition to external mesh import, the particle wake to simulate interactions with solid bodies, and the mid-fidelity aerodynamic analysis available on commercial laptops, with no need for high-performance computers. For more details about the numerical approach implemented in DUST, including the Vortex Particle Method, the reader is referred to [31] [27].

2.2. MBDyn

MBDyn is a multibody dynamics analysis software. It features the simulation of multi-component systems, including rigid and flexible bodies subject to kinematic constraints and hydraulic and electric elements. It can be coupled with external software, such as DUST, to perform aeroelastic simulations.

2.3. UAV modeling

In DUST, there are several aerodynamic elements available: Surface Panel (SP), Vortex Lattice (VL), Lifting Line (LL), and Non-Linear Vortex Lattice (NL-VL). Combining them makes it possible to enhance the fidelity level of the aerodynamic simulations.

Considering the Martian UAV under development, there is the need to model the solid

body, including the fuselage and the lifting surfaces, and the rotors. The first step, described in this chapter, consists of modeling the UAV body with its tridimensional shape to accurately compute the interaction with the rotors' wake. Firstly, a CAD model of the UAV external shape has been developed with SolidWorks. Afterward, a surface mesh has been generated with Gmsh and imported into DUST with a CGNS file format. Finally, the Surface Panel elements have been employed. DUST also supports a user-friendly and quick parametric geometry definition for lifting surfaces. For bluff bodies, such as nacelles and fuselage, an imported surface mesh is used.

2.3.1. CAD model

The CAD model requires the airfoil curves to be generated with MATLAB and imported into SolidWorks. The wing airfoil is the low-Reynolds airfoil optimized at Re = 100,000 and Ma = 0.30, since the UAV is designed to fly in cruise at 90 m/s at an altitude of 1,000 m, with Re ≈ 90,000 and Ma ≈ 0.37. The horizontal and vertical tails feature a NACA0006. The CAD model is not intended to reproduce a detailed structural design with spars, ribs, thin panels, and junctions. It is used only to represent the external shape of the UAV, which is necessary for the surface mesh. The structural design of the UAV might be the purpose of future work. Figure 2.1 and Figure 2.2 show the 3D CAD model and the relative technical drawings with some dimensions.

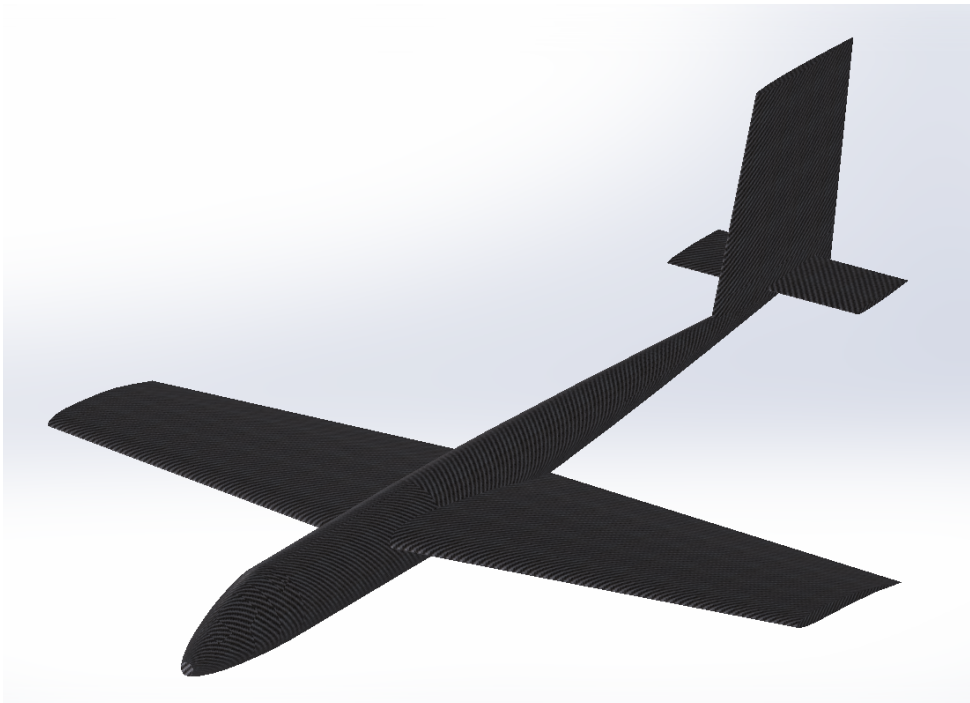

Figure 2.1: 3D CAD model

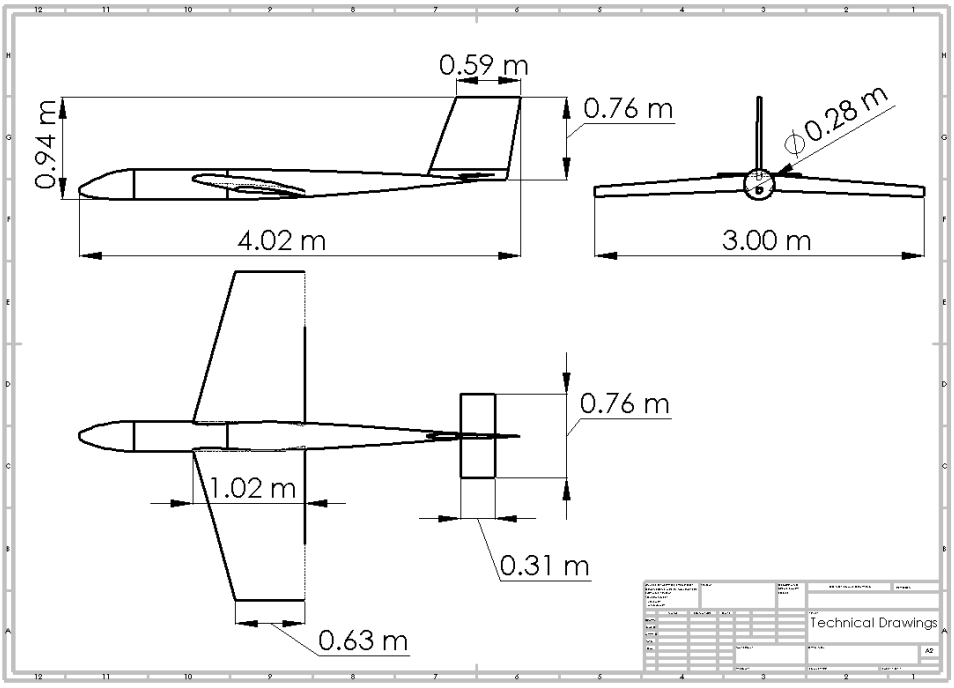

Figure 2.2: Technical drawings

2.3.2. Surface mesh

The CAD model is imported into Gmsh with a STEP file format containing information about points, curves, surfaces, and corresponding connections to create the surface mesh. Figure 2.3 shows the curves among different extrusions and lofts. The sequence of commands has been set to obtain a clear array of lines and allow the creation of a structured mesh on the lifting surfaces. In particular, the vertical tail has been divided into two different blocks: the lower part, where the horizontal tail is attached, features an unstructured mesh while the upper part is clean and a structured mesh is possible.

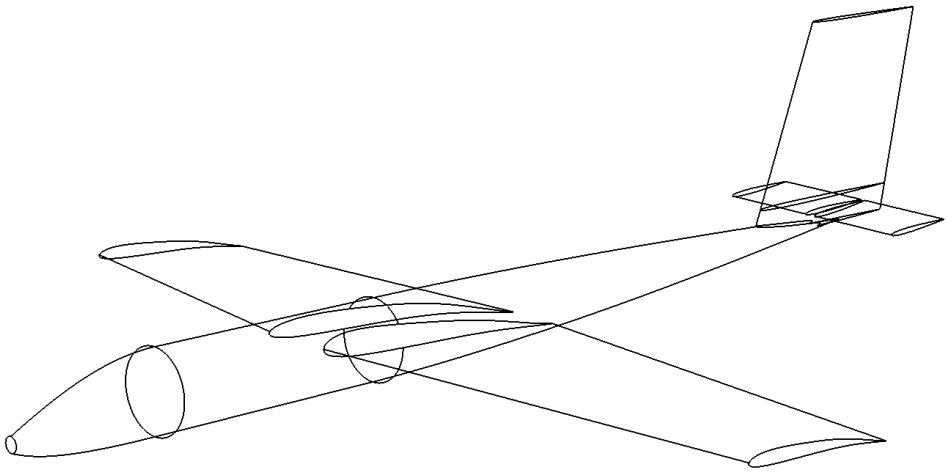

Figure 2.3: STEP file curves

DUST automatically recognizes a trailing edge when the angle between the normal vectors of two adjacent panels is large. If the leading edge of the lifting surfaces is not sufficiently refined it may be confused with trailing edge panels. Thus, the distribution of panels in the chordwise direction is not uniform but progressive, with more panels at the leading edge. In the spanwise direction it has been kept constant. Regarding the number of panels, the Airbus Vahana model has been taken as reference [27]. Vahana is an eVTOL, single-seat, tilt-wing demonstrator produced by Airbus, whose model was used to validate the DUST codes. Overall, 10,838 surface panels were used for the body. Considering that the Martian UAV is half the size, an approximately equal number of panels has been employed to be conservative. Table 2.1 lists the number of panels for each component.

Component	**Mesh type**	**Chordwise panels**	**Spanwise panels**	**Overall panels**
Wing (half)	Structured	30	50	$\approx$ 6,000
H. tail (half)	Structured	22	20	$\approx$ 1,800
V. tail	Structured[1]	30	40	$\approx$ 2,400
Fuselage	Unstructured[2]	/	/	$\approx$ 3,200
Full model	/	/	/	$\approx$ 13,400

Table 2.1: Mesh elements

[1]The upper part is structured, the lower part is unstructured and included in the fuselage.
[2]Except for 100 panels for the structured fuselage nose.

Most of the 13,400 panels are quadrangles, approximately 12,000, while the remaining elements are triangles. Figure 2.4 shows the full model mesh created for DUST simulations.

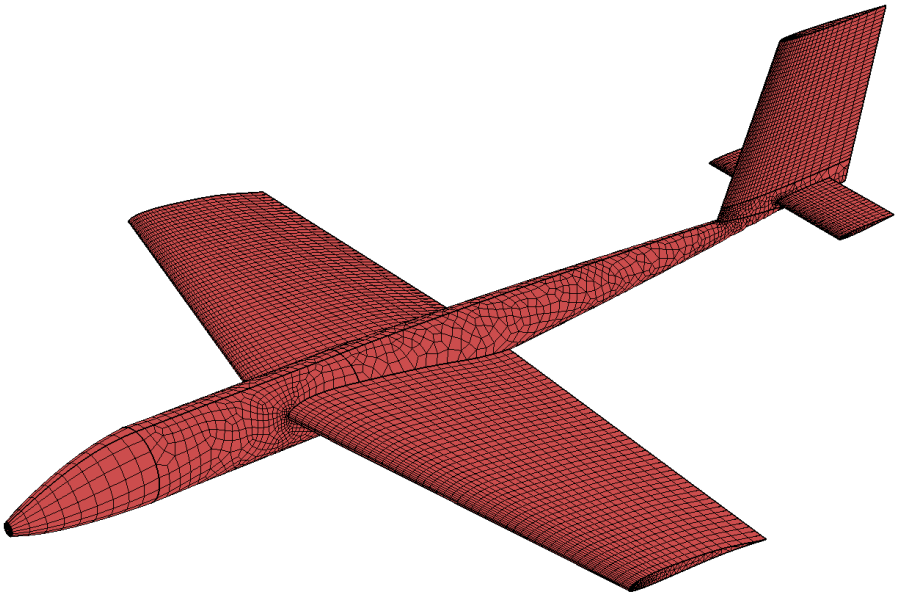

Figure 2.4: Full model surface mesh

Figure 2.5 provides a clearer image of the surface mesh on the wing. The aspect ratio of the panels is approximately 1 for the whole mid part of the wing while necessarily increases towards the leading and trailing edges.

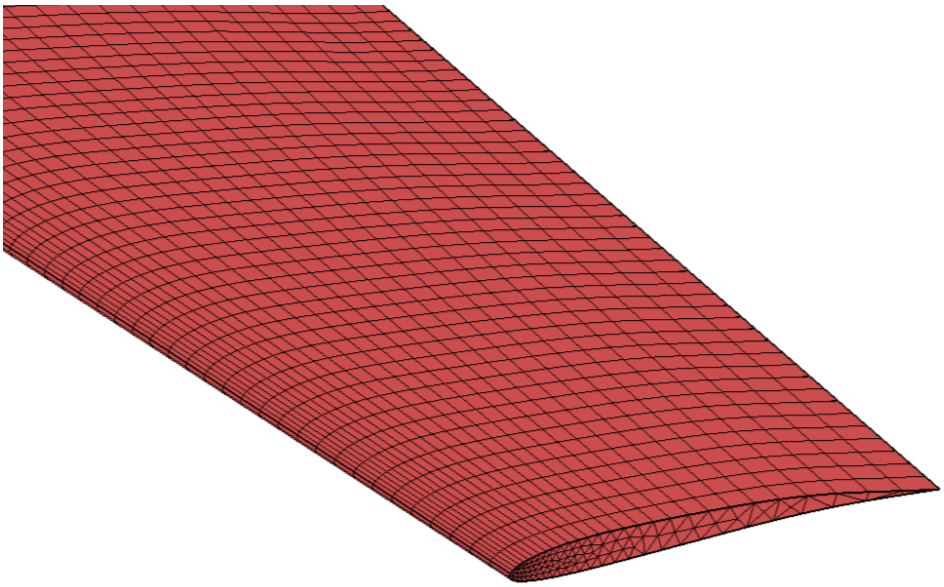

Figure 2.5: Wing surface mesh

3 Isolated rotor design

This chapter aims to provide a complete description of the process adopted to size an isolated rotor and to perform mid-fidelity aerodynamic simulations with DUST. The rotorcraft design book Stepniewski [25] has been intensively used for this purpose, together with scientific articles about Ingenuity [30] and the Advanced Mars Rotorcraft [14].

3.1. Thrust requirements

The maximum take-off mass of the UAV was fixed to 20 kg, as reported in Table 1.2. The gravity acceleration on Mars is about 3.72 m/s^2, leading to a maximum take-off weight of about 75 N.

In cruise at 90 m/s the UAV was estimated in [2] to be trimmed with a drag coefficient of about 0.05, according to an analysis conducted with OpenVSP, for an overall drag of about 7 N. When a rate of climb of 32 m/s is considered, the required thrust rises to 36 N. Table 3.1 summarizes the thrust requirements the propulsive system must satisfy to guarantee hover, cruise, and climb phases.

Flight phase	**Thrust requirement [N]**
Hover	75
Cruise	7
Climb	36

Table 3.1: Thrust requirements

3.2. Preliminary sizing

The number of rotors and the diameter of each rotor were calculated in [2], by trying to minimize the shaft power at hovering, with an empirical expression from Stepniewski [25]. Reasonably, to obtain symmetry around the center of gravity and to cancel out all the torques, the available number of rotors was four, eight, twelve, ... Choosing four rotors

would minimize the induced power contribution at hovering but also requires more space, especially in the tilted configuration. Finally, eight rotors with 36 in (0.91 m) diameter were selected. The overall shaft power at hovering was estimated to be 3,400 W.

3.3. Rotor solidity and blade average lift coefficient

First, three non-dimensional coefficients must be introduced to define the performance of the rotors. Equation 3.1 lists the thrust, torque, and shaft power coefficients, according to Stepniewski [25].

$$\begin{cases} C_T = \dfrac{T}{\pi R^2 \rho V_T^2} \\ C_Q = \dfrac{Q}{\pi R^3 \rho V_T^2} \\ C_P = \dfrac{P_s}{\pi R^2 \rho V_T^3} \end{cases} \tag{3.1}$$

where R is the rotor radius in [m], ρ is the atmosphere density in [kg/m^3] and V_T is the blade tip speed in [m/s].

The rotor solidity, defined as the ratio between the area of all blades and the disk area, plays an important role when the blade average lift coefficient has to be calculated. Equation 3.2 shows the simplest relation among the blade average lift coefficient $\overline{C_l}$, the rotor thrust coefficient C_T, and the rotor solidity σ.

$$\overline{C_l} = 6\frac{C_T}{\sigma} \tag{3.2}$$

The rotor solidity is inversely proportional to the blade's average lift coefficient. Since, in the low-Reynolds regime, the airfoils can only operate at relatively low lift coefficients to prevent stall, high rotor solidity must be employed, as confirmed by [14].

The previous equation, however, does not take two important phenomena into account: the cutout effect and the tip loss. The cutout effect reflects the negligible contribution to thrust generation of the inner part of the blade, from the root section to approximately 15% of the radius, due to low relative speed. The tip loss is related to the decreased angle of attack at the blade tip, caused by the induced velocity field. This means that the outer portion of the blade, approximately the last 5%, also does not provide significant contributions. When these two phenomena are considered, Equation 3.2 is modified into Equation 3.3.

$$\overline{C_l} = 6\frac{C_T}{\sigma}(r_e^3 - r_i^3) \tag{3.3}$$

where r_i and r_e are, respectively, the non-dimensional cutout radius and effective radius. Typically, r_i is less than 0.2, and it has a negligible effect on the blade average lift coefficient. Conversely, when r_e is less than 0.95, the blade average lift coefficient is hugely affected. For rectangular blades, r_e can be estimated with expressions provided by a generic method, Sissingh's method, and Wald's method [25], reported in Equation 3.4.

$$\begin{cases} r_e^{Generic} = 1 - 0.5\dfrac{\pi\sigma}{N_b} \\ r_e^{Sissingh} = 1 - 3.56\dfrac{\sigma}{N_b} \\ r_e^{Wald} = 1 - 0.98\sqrt{\dfrac{C_T}{N_b}} \end{cases} \tag{3.4}$$

where N_b is the number of blades of the rotor.

The rotor solidity has been fixed to 0.30, and five blades have been adopted for each rotor. This choice follows section 3.5. The blade average lift coefficient can also be used to calculate the ideal sectional lift coefficient, according to Equation 3.5.

$$C_{l_r} = \frac{2}{3}\frac{\overline{C_l}}{r} \tag{3.5}$$

where r is a non-dimensional spanwise coordinate.

Figure 3.1 shows the sectional lift coefficient obtained with these methods.

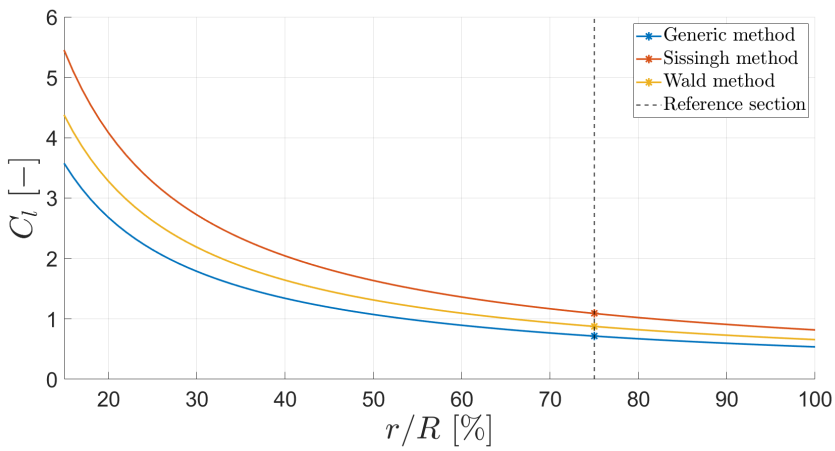

Figure 3.1: Blade ideal lift coefficient vs Spanwise location

These distributions are said to be optimal because they create a constant induced velocity field, which is a synonym of minimized induced power at hovering. However, it is practically impossible to reproduce such distributions. It is instead fundamental to

obtain similar lift coefficient values at the reference section, located at 75% of the radius. According to the generic method, it is 0.80, 1.23 for Sissingh, and 0.98 for Wald.

3.4. Blade twist angle and rotor collective pitch angle

The optimal lift coefficient distribution is correlated to a twist angle distribution, which is reported in Equation 3.6 and Figure 3.2.

$$\theta_r = \frac{2}{3}\frac{\overline{C_l}}{a_r r} + 0.289\frac{\sqrt{\overline{C_l}\sigma}}{r_e r} \tag{3.6}$$

where a_r is the blade airfoil lift curve slope in [1/rad], set to 5.18 from optimized airfoils (section 3.7).

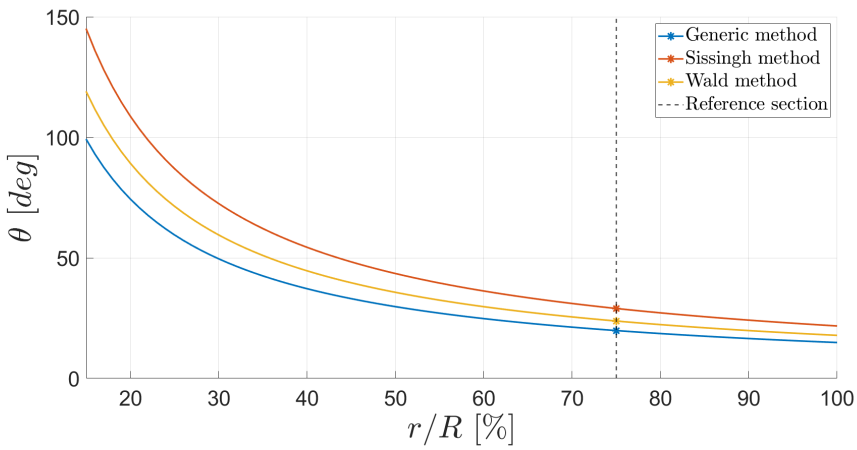

Figure 3.2: Blade ideal twist angle vs Spanwise location

It is not feasible to have such large twist angles at the root. What matters is to stick to the twist angles from the reference section to the tip section, where the trend appears linear. A collective pitch of 28° (root section) has been initially selected to meet the hover requirement and a modest linear twist of -10° has been applied from root to tip.

3.5. Blade planform and chord distribution

Both blade planform and chord distribution are related to the number of blades per rotor. Considering the fixed rotor solidity value, few blades mean a large chord, large local Reynolds number, and low aspect ratio. On the other hand, many blades mean small chords, low local Reynolds number, high aspect ratio, and possible structural problems. A total number of five blades per rotor has been considered a good trade-off, with the

average chord being about 20% of the radius, with a moderate aspect ratio (5.33) and a not-too-low Reynolds number. The blade planform is shown in Figure 3.3. At the root section, the chord has been reduced to make space for the blade attachment with the hub, while at the tip section, a slight sweep angle of 10.6° has been adopted to delay the drag rise phenomenon at transonic Mach number. However, according to the Advanced Mars Rotorcraft blade optimization [14], the sweep angle did not bring significant performance improvement.

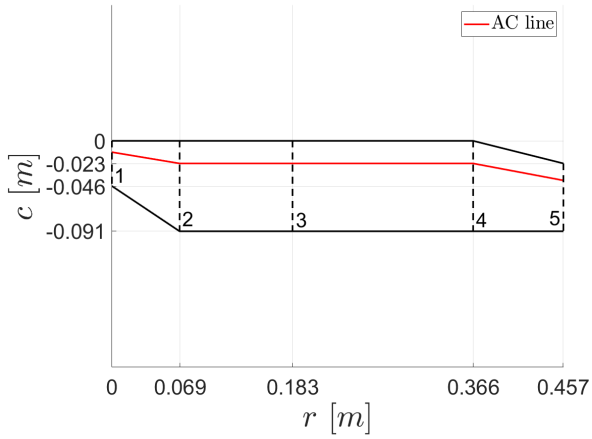

Figure 3.3: Blade planform

Five sections along the blade span have been explicitly drawn and numbered from 1 to 5. As explained in section 3.7, different airfoils have been used along the blade span at these sections. In addition, the blade portion between sections 1 and 2, representing the cutout effect zone, has never been modeled with DUST to prevent numerical issues. Figure 3.4 illustrates the blade chord distribution as percentage of the blade radius, instead of the top view.

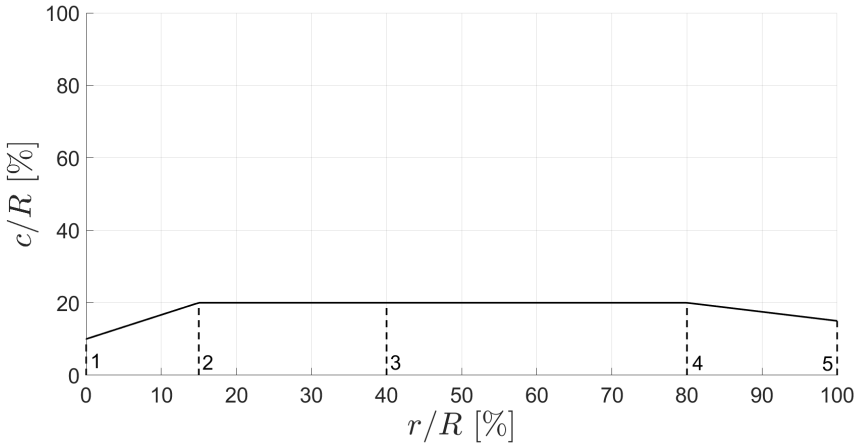

Figure 3.4: Blade chord distribution vs Spanwise location

3.6. Blade Reynolds and Mach numbers

Some remarks regarding the sectional Reynolds and Mach numbers have also been made. The blade tip Mach number has been fixed at 0.78 from the start, similarly to Ingenuity [30]. In addition, two different altitudes have been considered: 0 m and 1,000 m (cruising altitude). Figure 3.5 shows how the Reynolds and the Mach numbers vary along the blade span when the tip Mach number is fixed at its maximum allowed.

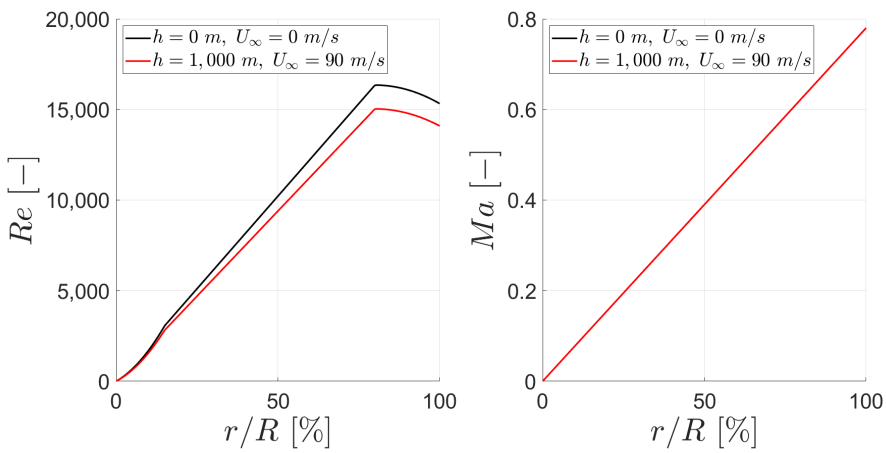

Figure 3.5: Blade Reynolds and Mach number distribution vs Spanwise location

The altitude change causes a variation of kinematic viscosity, which is reflected in a slight variation of Reynolds number distribution. Moreover, the sweep angle at the tip implies a reduction of Reynolds number.

3.7. Blade airfoils

According to Figure 3.5, different airfoils have been selected among those optimized in a previous work [19]. Table 3.2 contains the choices made.

Section	Optimized for Reynolds:	Optimized for Mach:
1, 2	10,000	0.1
3	10,000	0.3
4, 5	10,000	0.6

Table 3.2: Blade airfoil characteristics

The three optimized airfoils feature some differences regarding the shape, especially the camber line, as shown in Figure 3.6a, Figure 3.6b, and Figure 3.6c.

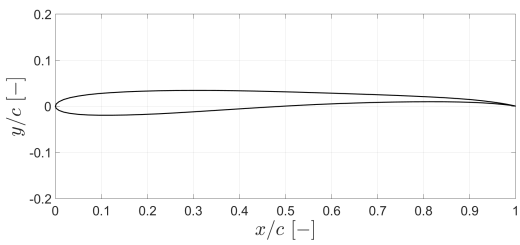

(a) Blade root section

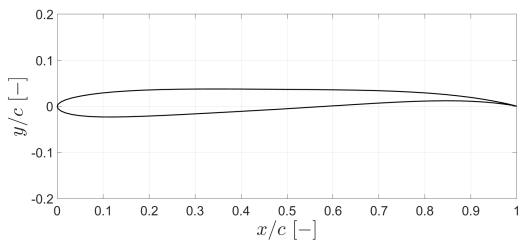

(b) Blade mid section

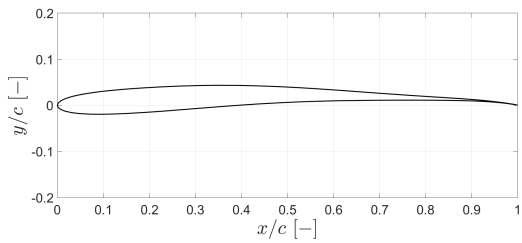

(c) Blade tip section

Figure 3.6: Blade optimized airfoils

The aerodynamic coefficients of lift, drag, and pitching moment were available for all the airfoils from CFD analyses, performed in a range of angles of attack between 0° and 9°. However, the rotor blades may be subject to reverse flow conditions. Thus, the CFD results have been extended with empirical methods to the range -180°/+180°, and the c81 tables have been created and imported into DUST [29] [13]. The following Figures

show the empirical extensions of lift, drag, and pitching moment coefficients of the root airfoil while the diagrams for mid and tip airfoils are gathered in Appendix A.

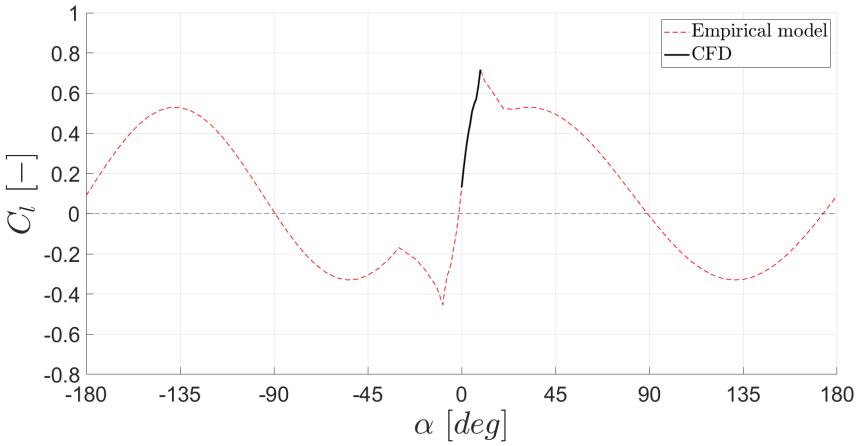

Figure 3.7: Lift coefficient for blade root airfoil

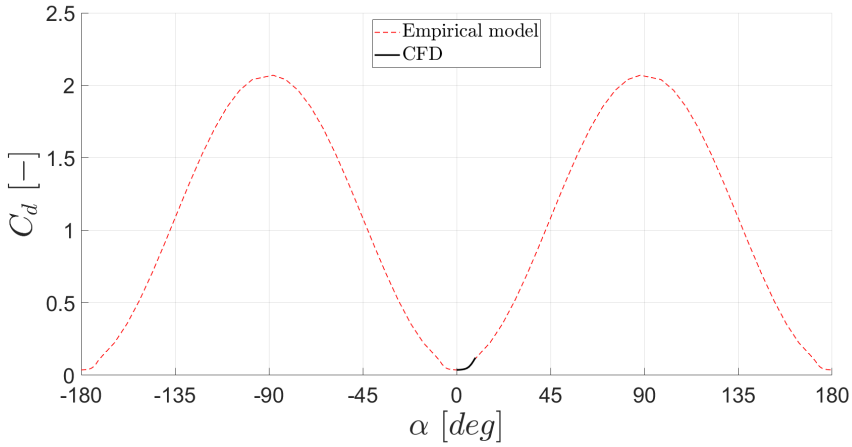

Figure 3.8: Drag coefficient for blade root airfoil

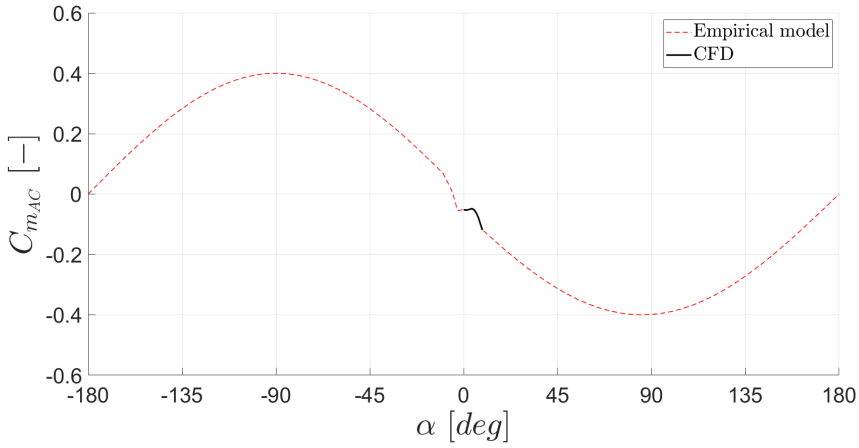

Figure 3.9: Pitching moment coefficient for blade root airfoil

3.8. DUST model

Several simulations have been performed with DUST for an isolated rotor at hovering to validate the rotor design, representing the strictest condition regarding numerical convergence. The rotor blades have been modeled in DUST as lifting line elements, which resort to tabulated data, namely the c81 tables of the optimized airfoils. This representation allows us to catch the viscous effects and the stall phenomenon properly. The baseline blade geometry, prior to the convergence study, consists of 20 lifting line elements. The simulations also require a discretization in time, initially set to 20 time steps per rotor revolution, for a total of 30 revolutions. Other data must be provided, such as the rotor angular velocity, asymptotic velocity, atmospheric pressure, speed of sound, density, dynamic viscosity.

The Fast Multipole Method (FMM), with the computational domain divided into boxes, and the Hover Convergence Augmentation System (HCAS) have been enabled to speed up the simulations and improve convergence. In addition, the lifting line damping factor and the lifting line stall regularization settings have been tuned to help convergence. The wake has been modeled with two panels attached to the blade trailing edges that later turn into wake particles. As suggested by the manual [5], the radius of the wake particles has been set equal to the dimension of a blade element, equal to the blade span divided by the number of lifting line elements.

3.9. Time and spatial convergence at hovering

The convergence study of the isolated rotor at hovering consists of defining the number of rotor revolutions, the value of the time step and the number of lifting line elements. The solution must be independent of these parameters. Firstly, the time discretization has been set to 20 time steps per revolution, and the spatial discretization to 20 lifting line elements per blade, as already mentioned. The rotor RPMs have been set to their maximum, 4,000, related to the blade tip Mach number limitation and blade span.

One simulation has been carried out, providing the results shown in Figure 3.10, Figure 3.11, and Figure 3.12.

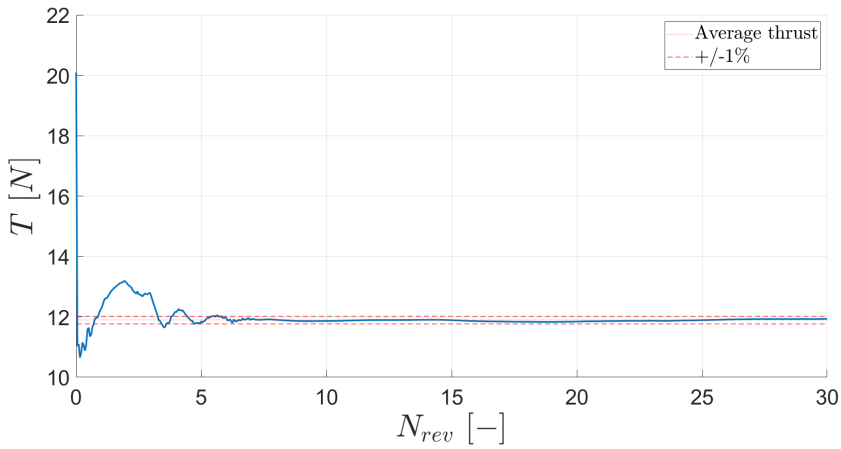

Figure 3.10: Rotor thrust vs Number of revolutions

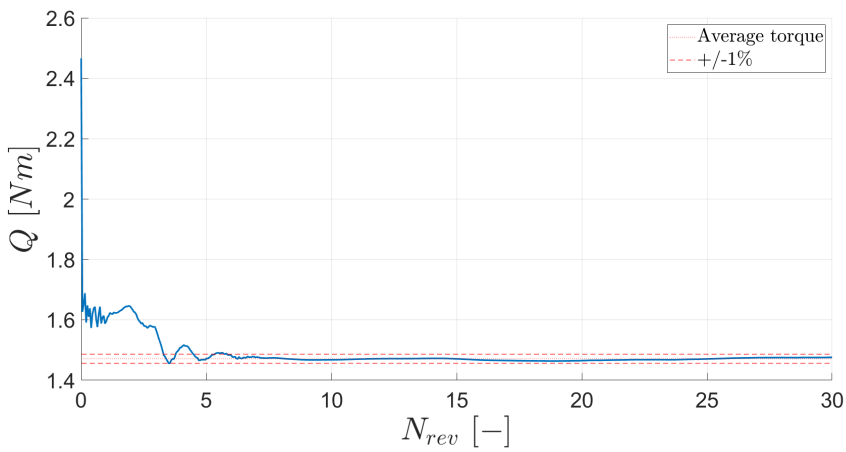

Figure 3.11: Rotor torque vs Number of revolutions

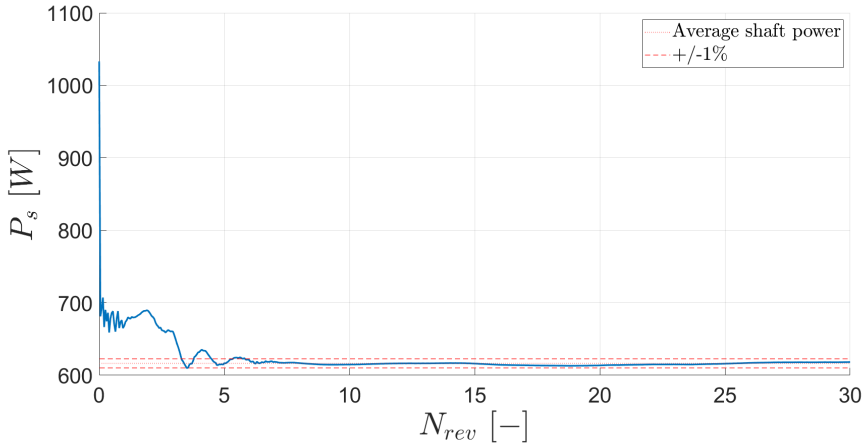

Figure 3.12: Rotor shaft power vs Number of revolutions

The thrust, torque, and shaft power trends show that after about 8 revolutions, the solution levels out and stays inside a +/-1% tolerance. To be conservative, 10 rotor revolutions were employed in the subsequent simulations. At this stage, several simulations have been performed with different time step values, ranging from 20 to 120. The average values of thrust, torque, and shaft power have been calculated over the last 2 rotor revolutions and plotted in Figure 3.13, Figure 3.14, and Figure 3.15.

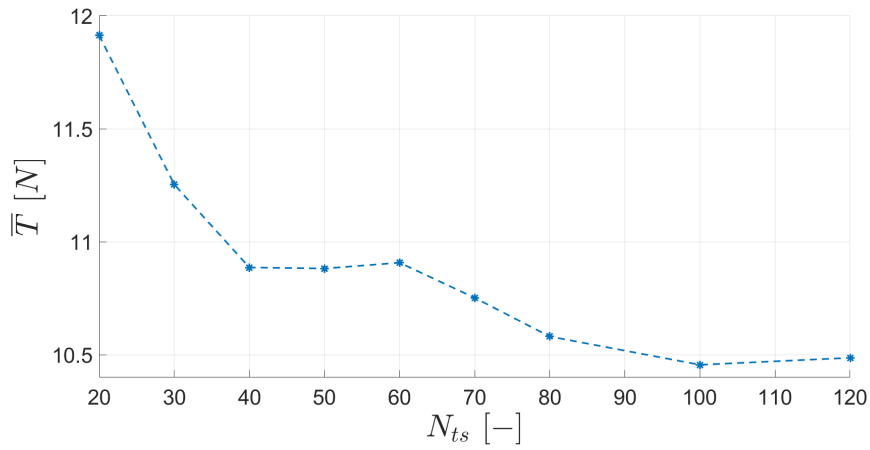

Figure 3.13: Rotor average thrust vs Number of time steps per revolution

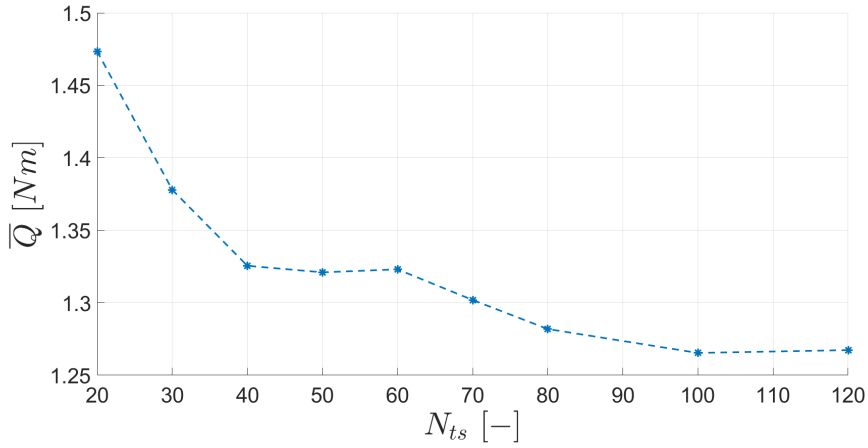

Figure 3.14: Rotor average torque vs Number of time steps per revolution

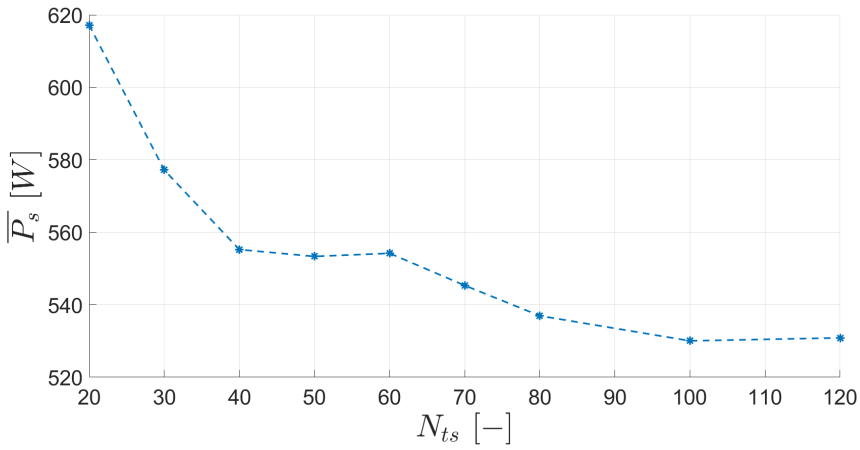

Figure 3.15: Rotor average shaft power vs Number of time steps per revolution

The trend appears stable with 60 time steps, but the time convergence is reached at 100 time steps. This result is in accordance with a study conducted on the XV-15 tiltrotor [31], where the time convergence is obtained with 40 time steps in a rotor with three blades rotating at lower RPMs. Finally, other simulations have been performed with a variable number of lifting line elements, from 10 to 40. The results are illustrated in Figure 3.16, Figure 3.17, and Figure 3.18.

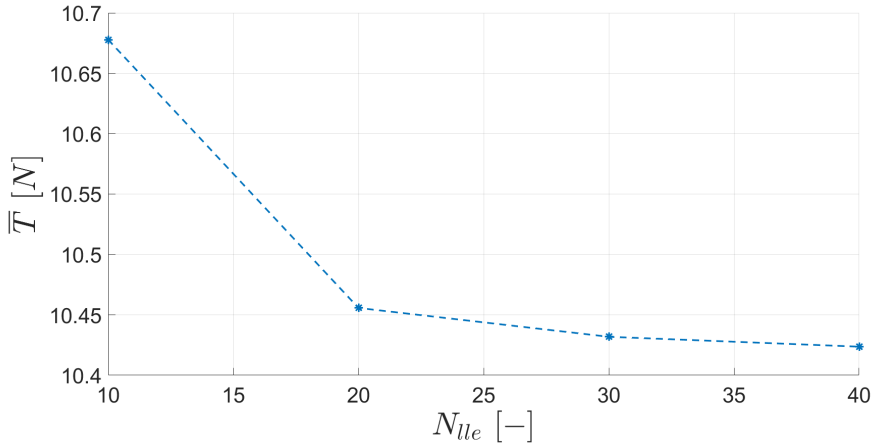

Figure 3.16: Rotor average thrust vs Number of lifting line elements per blade

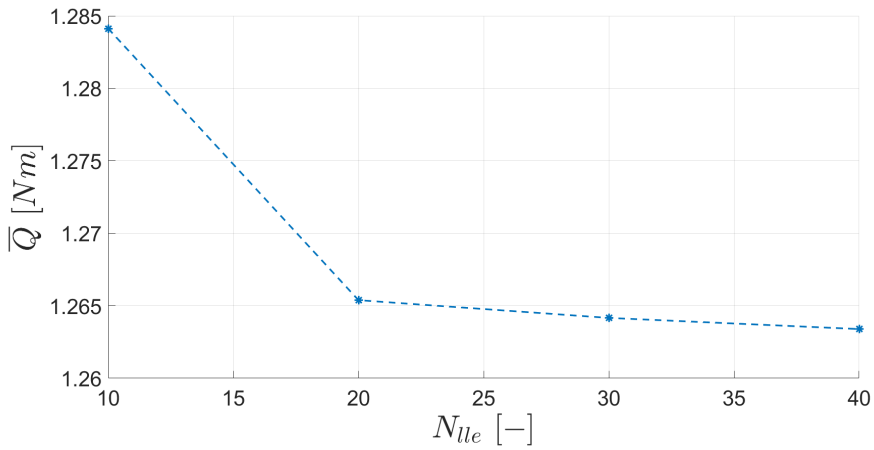

Figure 3.17: Rotor average torque vs Number of lifting line elements per blade

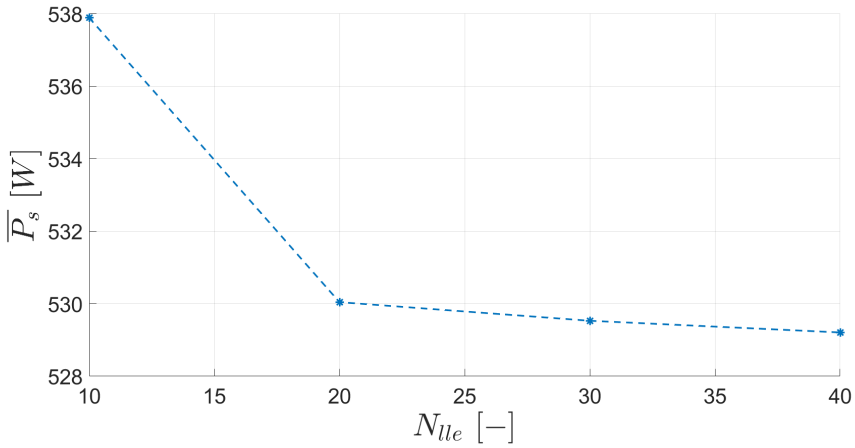

Figure 3.18: Rotor average shaft power vs Number of lifting line elements per blade

The baseline geometry, with 20 lifting line elements, is already at spatial convergence. This is confirmed by the XV-15 analysis as well, where 20 lifting line elements are used for a longer blade.

To summarize, with 28° of collective pitch and 4,000 RPMs the thrust, torque, and shaft power generated by the isolated rotor at time and spatial convergence are collected in Table 3.3, together with the non-dimensional coefficients and the figure of merit.

T	Q	P_s	C_T	C_Q	C_P	FM
10.46 N	1.265 Nm	530.0 W	0.03285	0.008695	0.008695	48.4%

Table 3.3: Rotor parameters at hovering at convergence

The UAV must be able to accelerate upwards during take-off at maximum RPMs. The thrust required in this phase equals the thrust required at hovering, shown in Table 3.1, multiplied by an incremental factor. With a 20% excess of thrust, each rotor must generate 11.3 N. To meet this requirement the collective pitch of the rotor has been fixed to 30° for the following simulations. When hovering, the RPMs are slightly reduced.

Besides the rotor integral loads, plotting the blade lift coefficient distribution at time and spatial convergence is also interesting. Figure 3.19 shows that in the reference section, the lift coefficient value is in accordance with the estimation provided by Stepniewski with the generic method and Wald's method [25]. Furthermore, the tip loss with reduction of angle of attack is visible.

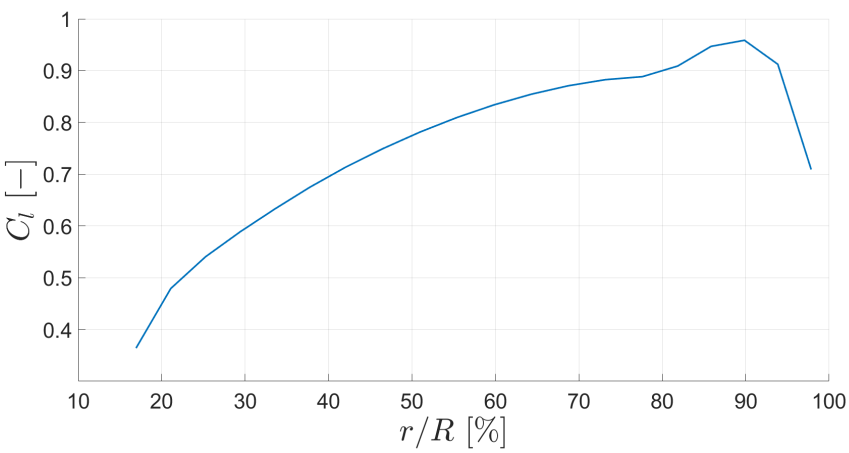

Figure 3.19: Blade lift coefficient vs Spanwise location

Two visualizations have been created to reproduce the numerical wake particle dimensions,

the distribution of pressure (Figure 3.20) and singularity intensity (Figure 3.21) on the blades. In this context, namely the lifting line elements, the pressure is correlated to the lift. The higher the pressure, the higher the local lift, for example, at the blade tips. The singularity intensity represents the intensity of the surface/point solution on the different elements. It is greater at the blade root, where the twist angle is higher. The tip loss phenomenon is visible thanks to the reduction of both pressure and singularity intensity.

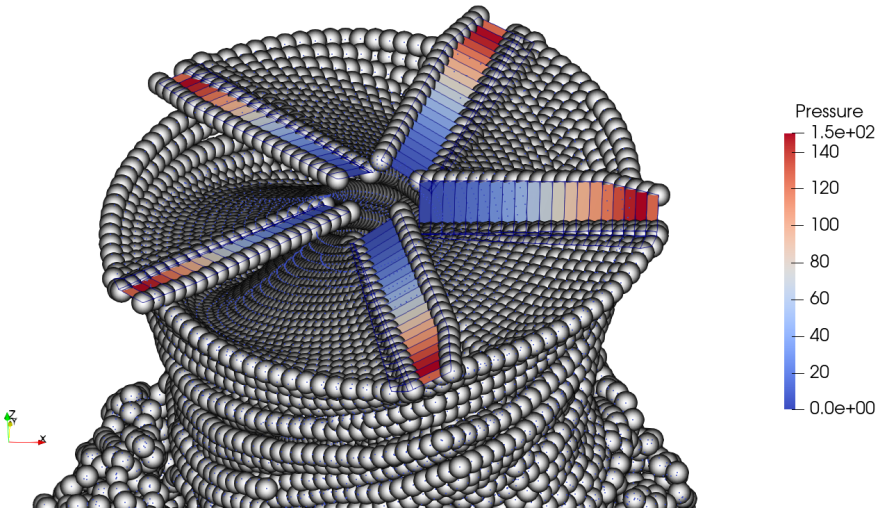

Figure 3.20: Rotor pressure and wake particles at hovering at convergence

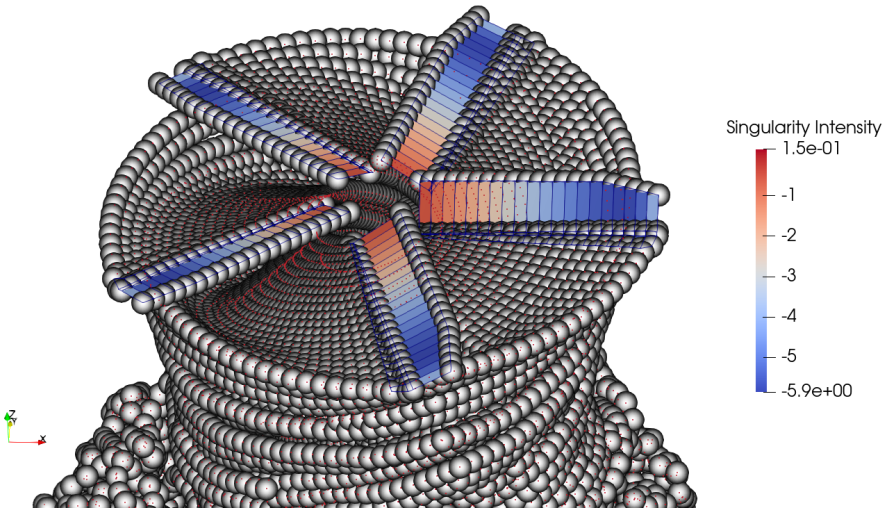

Figure 3.21: Rotor singularity intensity and wake particles at hovering at convergence

Figure 3.22 shows the wake evolution in time from a lateral perspective, respectively after 1, 5, and 10 revolutions. After the initial transient the wake is fully developed and the solution becomes steady.

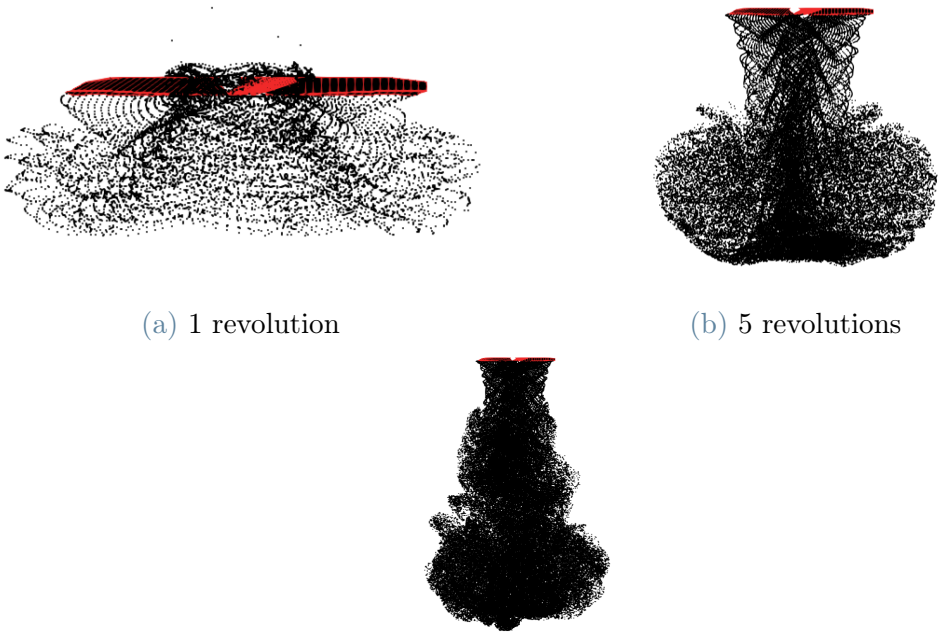

(a) 1 revolution

(b) 5 revolutions

(c) 10 revolutions

Figure 3.22: Rotor wake evolution at hovering - lateral view

3.10. Cruise

After the complete characterization of the isolated rotor at hovering, it is necessary to consider its performance in cruise conditions. The cruising phase is performed at high speed, 90 m/s thus variable pitch rotors/propellers are mandatory. Figure 3.23 provides some insights about the order of magnitude of the tilted rotor advance angle and ideal twist angle in cruise, calculated with a blade tip Mach number fixed to 0.6. The advance angle is retrieved from the velocity triangle of asymptotic velocity and blade tip speed. In contrast, the ideal twist angle curve is translated by 4°, the angle of attack that guarantees the maximum lift-to-drag ratio for the optimized airfoils. At the reference section, namely 75% of the radius, the twist angle is about 50°, confirming that a variable pitch tilting rotor is needed to meet hover and cruise requirements.

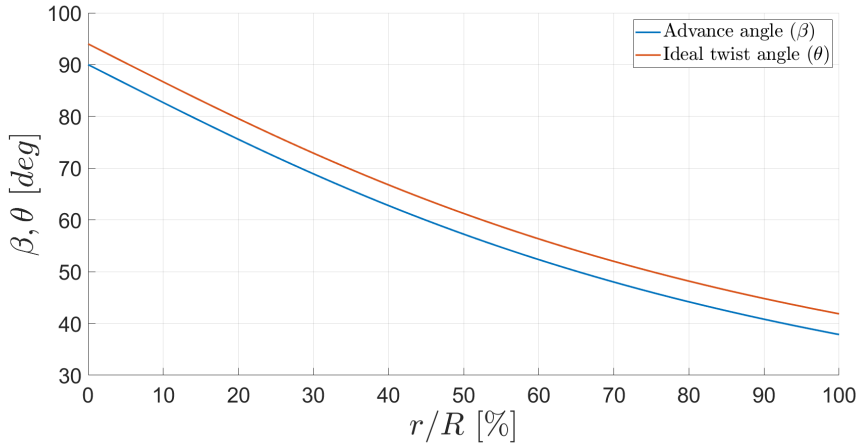

Figure 3.23: Blade advance angle and ideal twist angle vs Spanwise location

When the rotor is tilted horizontally, it is handled as a propeller. A new set of non-dimensional coefficients for thrust, torque, and shaft power must be introduced. Equation 3.7 collects the Rénard's expressions.

$$\begin{cases} C_T = \dfrac{T}{\rho n^2 D^4} \\ C_Q = \dfrac{Q}{\rho n^2 D^5} \\ C_P = \dfrac{P_s}{\rho n^3 D^5} \end{cases} \tag{3.7}$$

where n is equivalent to the revolutions per second (RPSs) in [1/s]. The thrust, torque, and shaft power coefficients are typically functions of the advance ratio, defined in Equation 3.8.

$$J = \frac{U_\infty}{nD} \tag{3.8}$$

Many simulations have been carried out with collective pitch set to 50°, 55°, and 60°. The advantage of a variable pitch propeller is its capability of continually operating at high efficiency. The propeller efficiency, defined in Equation 3.9, is the ratio between the available power and the shaft power.

$$\eta = \frac{P_a}{P_s} = \frac{TU_\infty}{Q\omega} = \frac{C_T}{C_P} J \tag{3.9}$$

Figure 3.24 and Figure 3.25 show the thrust coefficient as function of the advance ratio and the curves of cruise and climb equilibrium with respectively 4 and 2 tilted rotors.

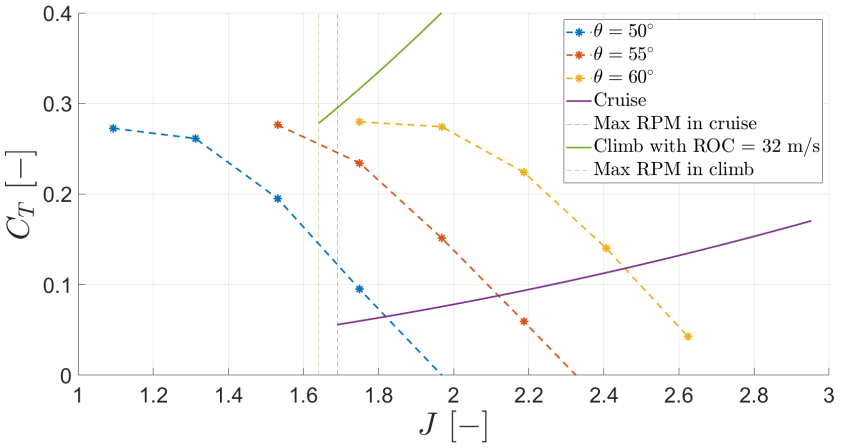

Figure 3.24: Propeller thrust coefficient vs Advance ratio (4 propellers)

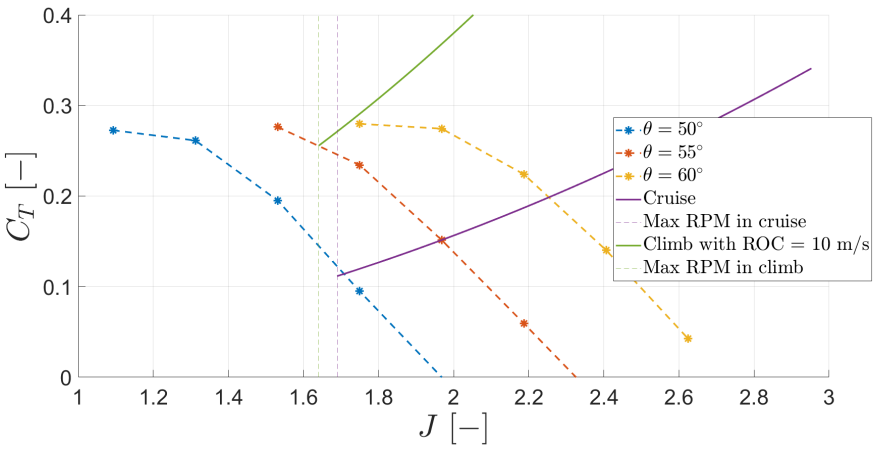

Figure 3.25: Propeller thrust coefficient vs Advance ratio (2 propellers)

The initial climb requirement of 32 m/s of the rate of climb cannot be met with only two tilted rotors. It should be relaxed to 10 m/s, which still represents a good climb performance. However, as explained in section 3.11, the number of tilted rotors chosen for the UAV is dictated by other requirements.

Figure 3.26 and Figure 3.27 respectively show the torque and shaft power coefficients as function of the advance ratio. In particular, the shaft power coefficient equals the torque coefficient multiplied by 2π.

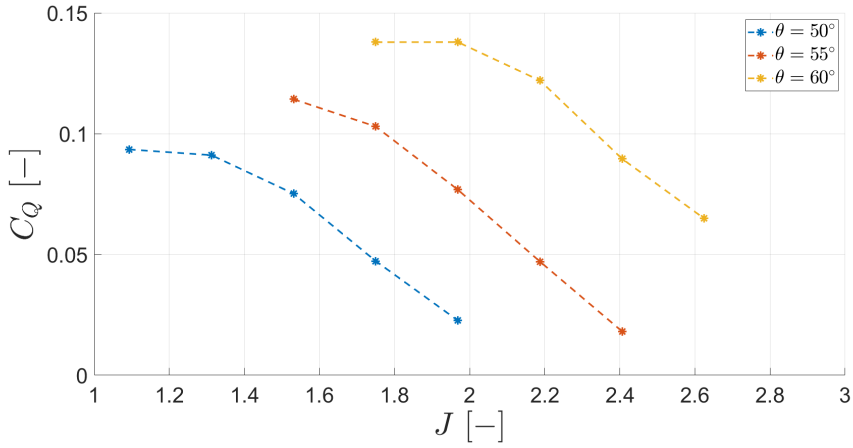

Figure 3.26: Propeller torque coefficient vs Advance ratio

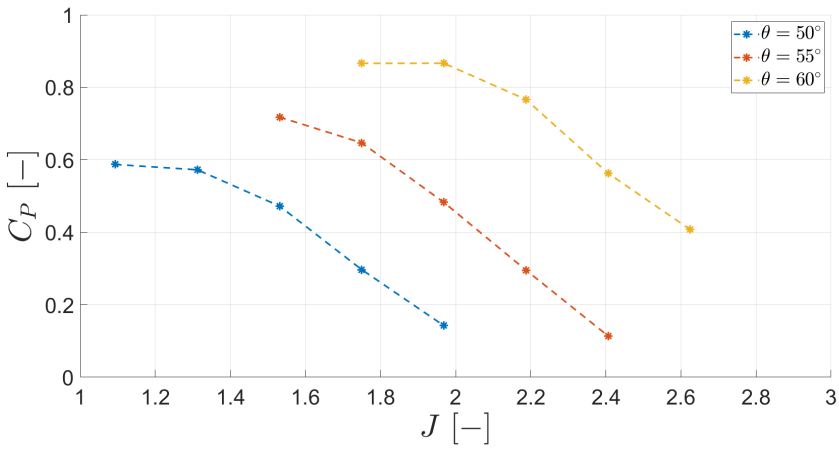

Figure 3.27: Propeller shaft power coefficient vs Advance ratio

Finally, the tilted rotor efficiency curves have been created (Figure 3.28). The equilibrium conditions calculated before correspond to a propeller efficiency range between 0.55 and 0.60. Despite the low-Reynolds regime caused by the Martian atmosphere it can be considered a good result.

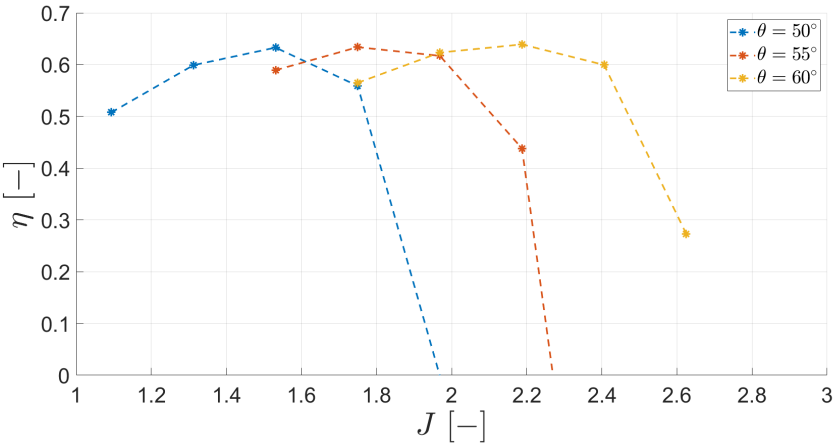

Figure 3.28: Propeller efficiency vs Advance ratio

3.11. Transition

The transition phase of the Martian UAV consists of progressively tilting either 2 or 4 front rotors, which provide both vertical thrust to sustain the UAV and horizontal thrust to accelerate. In contrast, the rear rotors stay in hover configuration with fixed collective pitch, similar to the Archer Midnight prototype shown in Figure 3.29.

(a) Helicopter mode - Hover

(b) Airplane mode - Cruise

Figure 3.29: Archer Midnight in different flight phases [1]

The UAV aerodynamic forces, namely lift and drag, proportionally increase with airspeed until the trim condition in cruise is obtained. The pitching moment must be kept null throughout the whole phase using elevator control. The angle between the rotor rotation axis and the UAV body x-axis, which is typically called "nacelle angle" when dealing with tilting rotors, has been called ϕ. Its value is 90° at hovering and 0° in cruise. To correctly address the transition problem, it is important to calculate the RPMs limitation

due to the blade tip Mach number as a function of airspeed and nacelle angle. Figure 3.30 shows that for all rotor inclinations, the limitation on the RPMs becomes stricter when the airspeed increases. In addition, if the rotor remains in hover configuration, namely 90° of inclination, the limitation is much greater than the case of a tilted rotor.

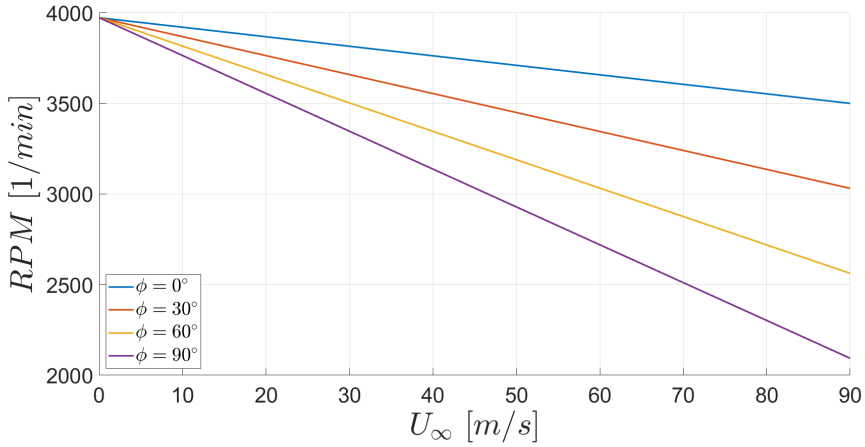

Figure 3.30: Rotor max RPM vs True airspeed

As stated before, different values of collective pitch are needed for the tilting rotors. In particular, 30° are employed in hover and 60° in cruise. To ease the problem, a linear relation has been used to correlate the rotor inclination and the collective pitch, as shown in Figure 3.31.

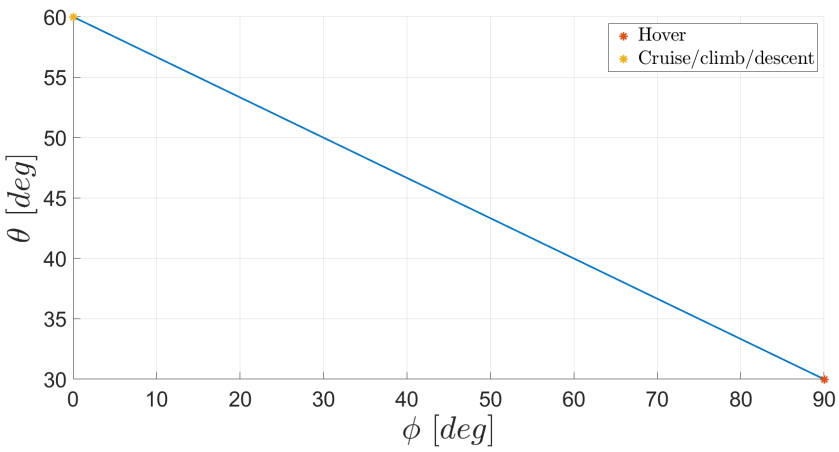

Figure 3.31: Rotor collective pitch angle vs Rotor inclination angle

The transition phase is supposed to be performed at low altitude and at a constant angle of attack, thus at constant lift and drag coefficients. In principle, the angle of attack can

be arbitrarily chosen. However, a high angle of attack attitude cannot be maintained at low speed because the elevator still does not have sufficient authority. A lower angle of attack, such as the 2° employed for the cruise, is more realistic. As shown in Figure 3.32, the drone lift equals the maximum take-off weight at the cruising speed of 90 m/s. The corresponding lift and drag coefficients are 0.55 and 0.052.

When the vertical equilibrium is reached, the rear rotors are shut down, and the tilted front rotors continue to run. After this operation, the drone can also slow down in airplane mode up to the stalling speed of 70 m/s by changing the angle of attack and the elevator deflection. Figure 3.32 also shows the overall required vertical thrust during the transition, calculated as the difference between the maximum take-off weight and the quadratic lift at cruising attitude.

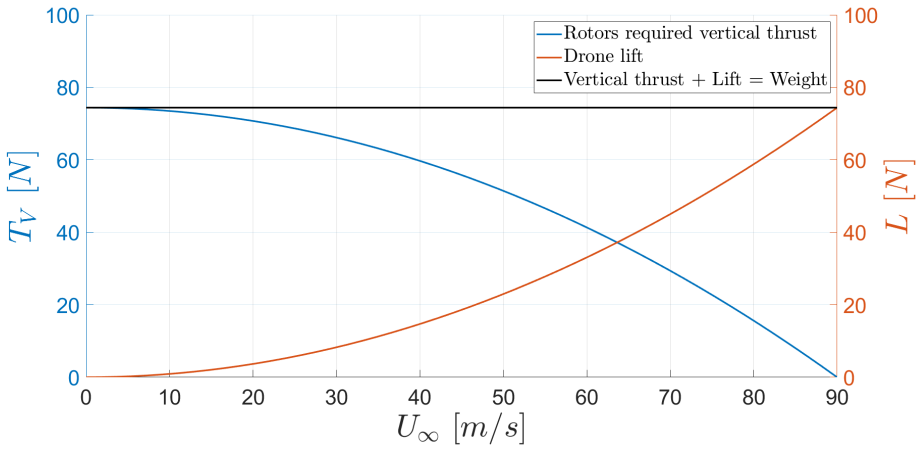

Figure 3.32: Rotors required vertical thrust and Drone lift vs True airspeed

Both front and rear rotors must provide the required vertical thrust. As already mentioned, the rear rotors feature a fixed collective pitch of 30° and do not tilt. Some simulations have been performed with DUST at the maximum RPMs, considering the limitation in Figure 3.30, to make sure there is sufficient vertical thrust to sustain the drone during the transition phase. Figure 3.33 shows the required vertical thrust of one rotor and its thrust generated at maximum RPMs.

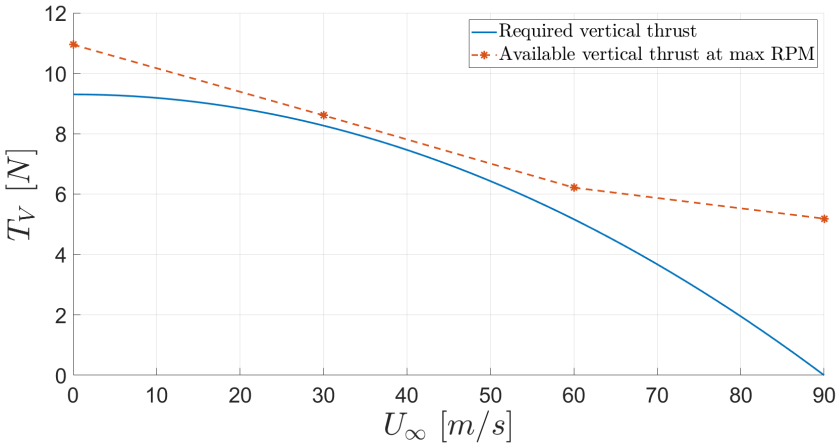

Figure 3.33: Rear rotor required and available vertical thrust vs True airspeed

The RPMs have to be reduced to find the precise trim condition. This procedure is detailed in chapter 4. Figure 3.34 and Figure 3.35 show the wake evolution of the isolated rear rotor at 30 m/s after 1, 4, and 8 revolutions.

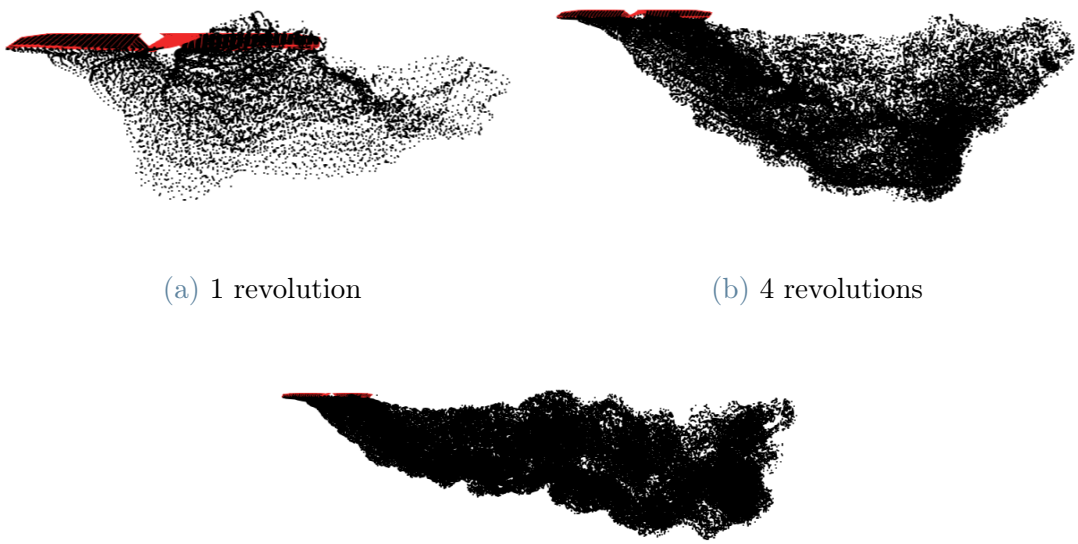

(a) 1 revolution

(b) 4 revolutions

(c) 8 revolutions

Figure 3.34: Rear rotor wake evolution in transition at 30 m/s - lateral view

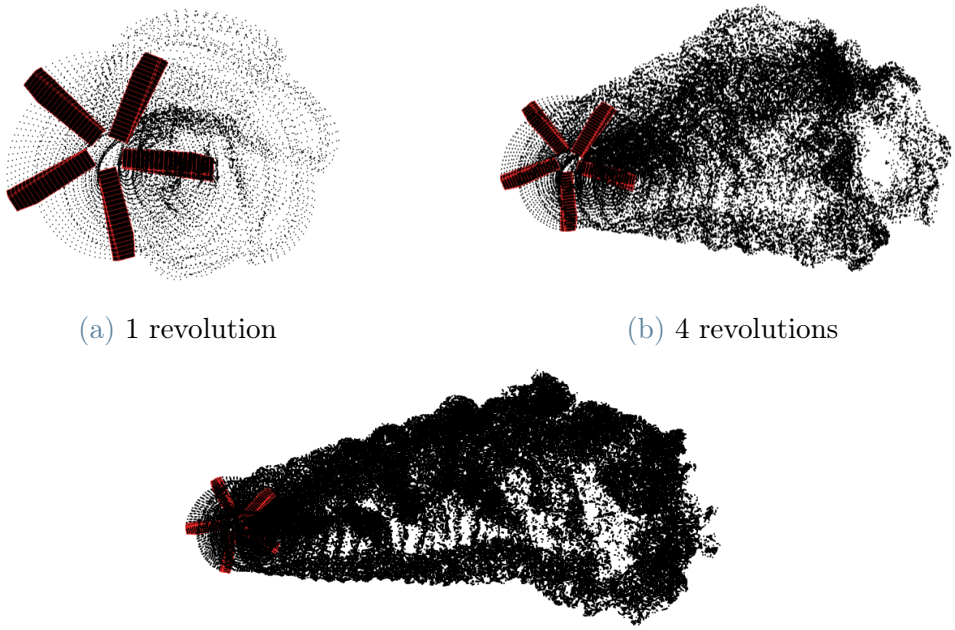

(a) 1 revolution

(b) 4 revolutions

(c) 8 revolutions

Figure 3.35: Rear rotor wake evolution in transition at 30 m/s - top view

At this stage, the curves displayed in Figure 3.33 have been used to calculate a first guess of the inclination of the tilted rotors without considering the change of collective pitch. Indeed, the excess of vertical thrust can be roughly transformed into an inclination angle, according to Equation 3.10.

$$\phi = \arcsin\left(\frac{T_V^{req}}{T_V}\right) \tag{3.10}$$

Figure 3.36 shows the tilted rotor inclination as a function of airspeed. The curve must be corrected at low speeds since the hover configuration features an inclination angle of 90°, and the excess thrust is used to accelerate upwards. This non-linear law has been used as a first guess to set the simulation parameters of the isolated tilted rotor.

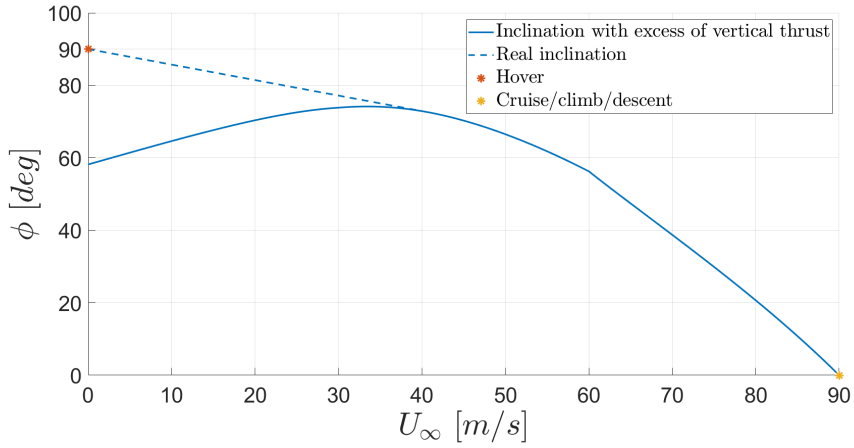

Figure 3.36: Rotor inclination angle vs True airspeed

With maximum allowed RPMs and variable collective pitch as function of the inclination angle, the tilted rotors provide a sufficient amount of vertical thrust, as illustrated in Figure 3.37.

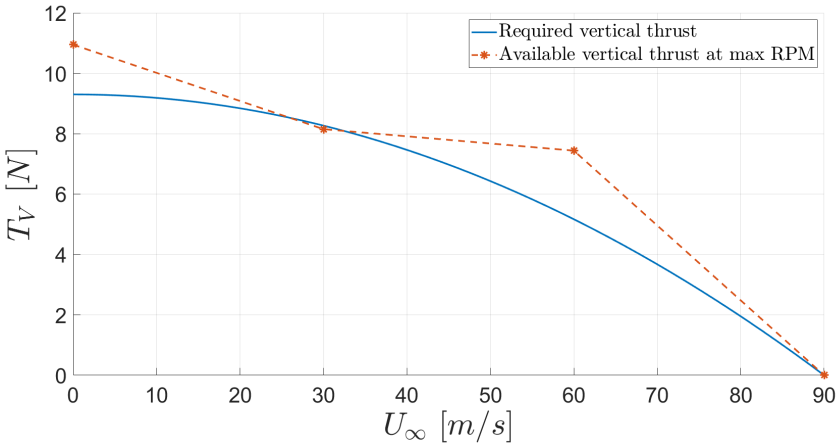

Figure 3.37: Front rotor required and available vertical thrust vs True airspeed

Figure 3.38 and Figure 3.39 show the wake evolution of the isolated tilted front rotor at 30 m/s after 1, 4, and 8 revolutions.

(a) 1 revolution

(b) 4 revolutions

(c) 8 revolutions

Figure 3.38: Front rotor wake evolution in transition at 30 m/s - lateral view

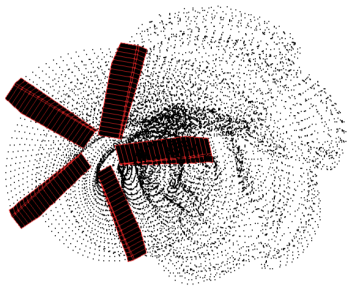

(a) 1 revolution

(b) 4 revolutions

(c) 8 revolution

Figure 3.39: Front rotor wake evolution in transition at 30 m/s - top view

Figure 3.40 shows the wake evolution of the isolated tilted front rotor at 90 m/s after 1,

4, and 8 revolutions.

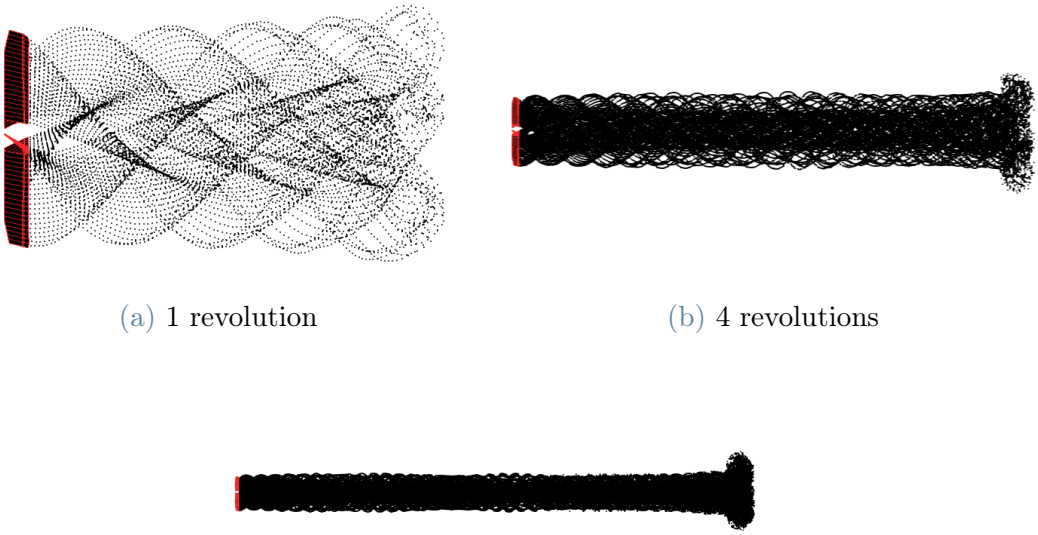

(a) 1 revolution (b) 4 revolutions

(c) 8 revolutions

Figure 3.40: Front rotor wake evolution in cruise at 90 m/s - lateral view

Figure 3.41 shows the pressure and the singularity intensity distributions on the tilted rotor blades. The first 2 panels of the wake, before is turns into particles, are visible.

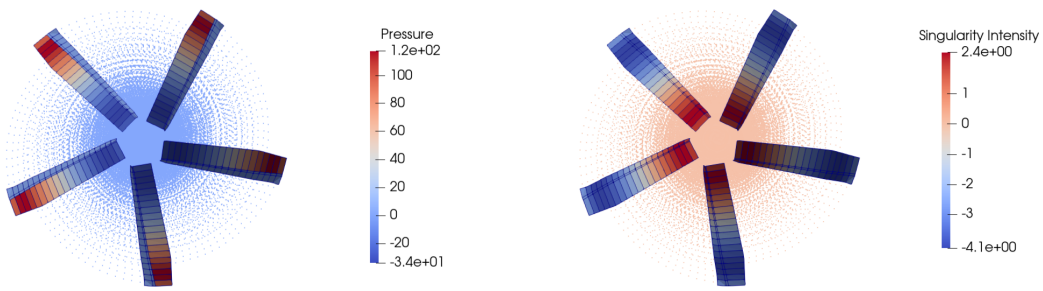

(a) Pressure (b) Singularity intensity

Figure 3.41: Front rotor in cruise at 90 m/s - front view

The tilted rotors have to satisfy the vertical required thrust and the horizontal required thrust, which is composed of the UAV drag (parasitic and lift-induced components) and the rotating rear rotors' drag (profile and induced drag). In fact, during the transition the rear rotors operate as helicopter rotors, with asymptotic wind in the plane of the

disk. The advancing blades produce more local drag than the retreating blades, causing an overall drag component that must be summed to the clean drone drag. Figure 3.42 and Figure 3.43 respectively show the required and the available horizontal thrust when 4 and 2 tilting rotors are employed.

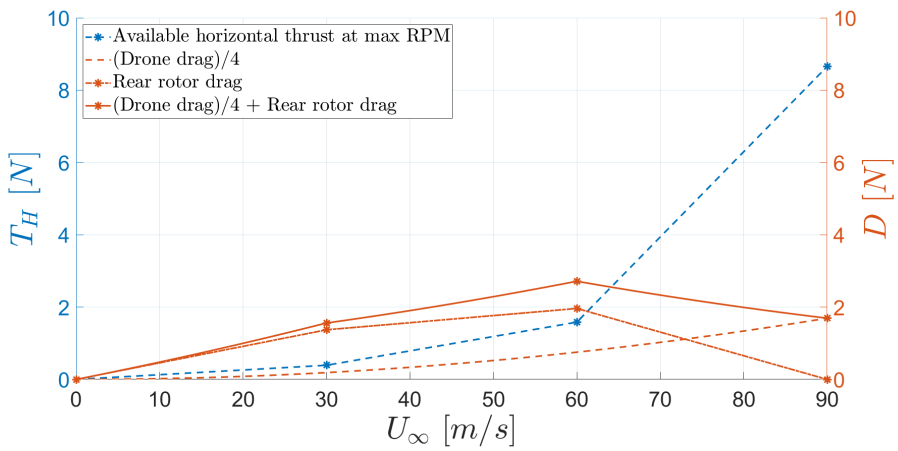

Figure 3.42: Front rotor available horizontal thrust and Drone drag vs True airspeed (4 rotors)

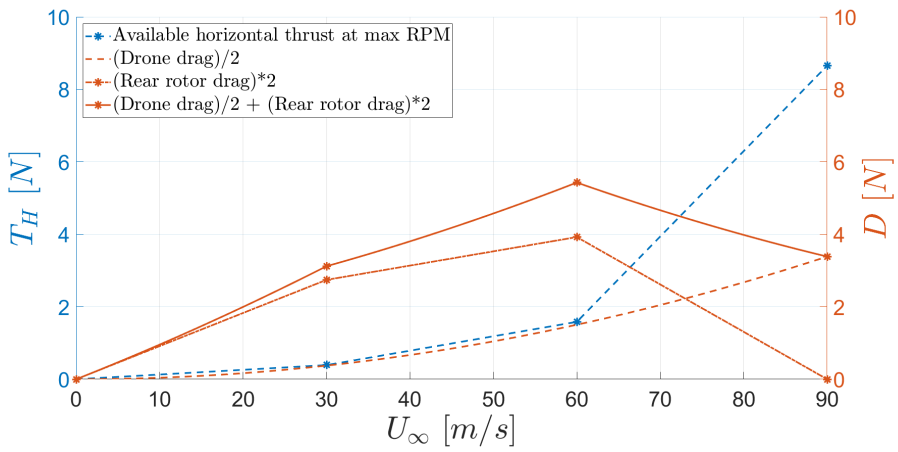

Figure 3.43: Front rotor available horizontal thrust and Drone drag vs True airspeed (2 rotors)

It is straightforward to notice that, in both cases, there is no sufficient horizontal thrust to accelerate and complete the transition. The configuration with only 2 tilting rotors is therefore discarded. The configuration with 4 tilting rotors, instead, requires a few adequate modifications to be satisfactory. The critical condition occurs at low speed when the inclination angle is still too large, according to the law shown in Figure 3.36.

If a linear law is adopted (Figure 3.44), the inclination at low speed is reduced, but also higher values of RPMs are allowed before exceeding the blade tip Mach number limitation.

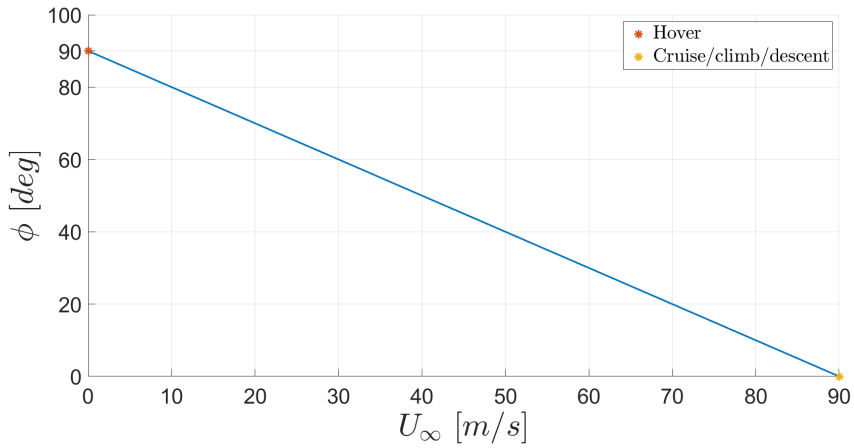

Figure 3.44: Rotor inclination angle vs True airspeed

The following chapter discusses the correct trim settings for the full model, including the inclination angle, the collective pitch angle, and the RPMs for all flight phases.

4 | Full model aerodynamic analysis

In this chapter, the UAV surface mesh and the isolated rotor geometry are combined to create the complete configuration. The positioning of the eight rotors is decided first. Afterwards, a few simulations of the full model are performed with specific trim settings, and the results are analyzed.

4.1. Rotors positioning

The position of the front and rear rotors is not entirely arbitrary because the UAV must maintain a level attitude while hovering. This implies that the moments generated by the thrust of the eight rotors about the center of gravity must cancel out. Furthermore, it is preferable not to have rotors located above the lifting surfaces not to obstruct their wake. In Figure 4.1, the UAV CAD model, augmented with the eight rotors, is illustrated.

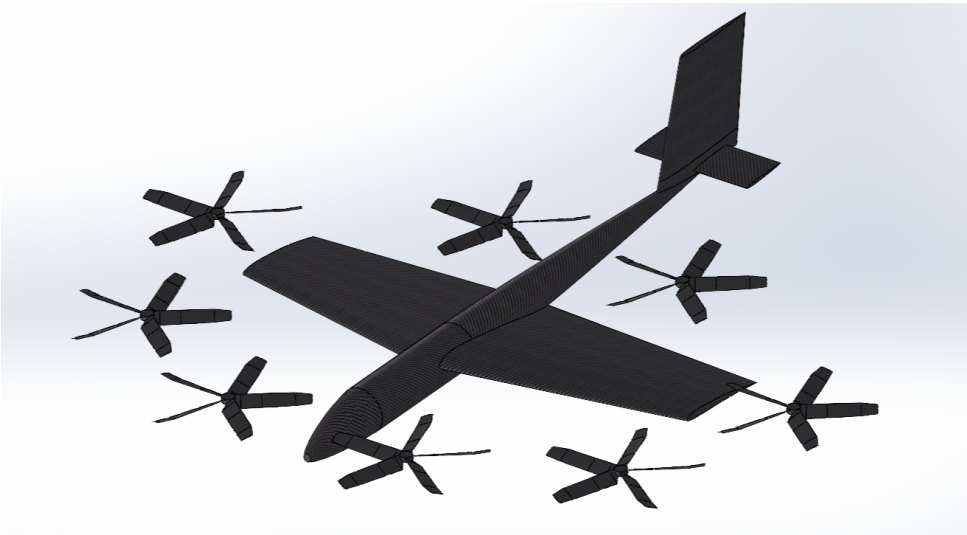

Figure 4.1: 3D CAD model with rotors

The front right and rear left rotors rotate anticlockwise, while the front left and rear

right rotors rotate clockwise. In this manner, the resultant of all torques is null, and differential thrust can be employed to maneuver in helicopter mode. In addition, when the front rotors are tilted in airplane mode, they are all inboard-up rotating, counteracting the effect of wingtip vortices and making the wing more aerodynamically efficient [15].

Figure 4.2 shows the top view of the definitive configuration with the relative dimensions with respect to the center of gravity.

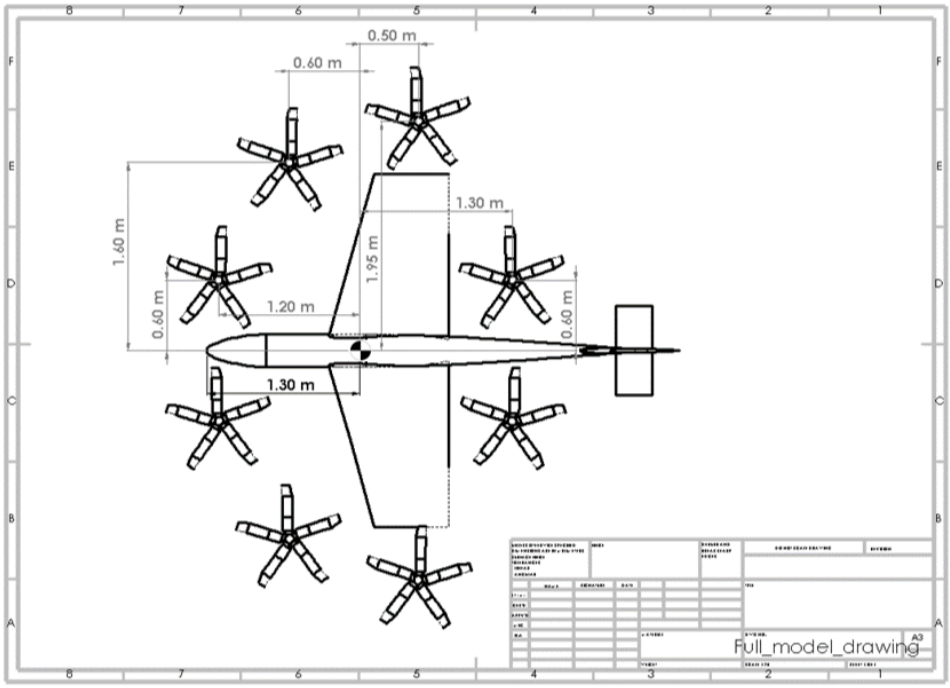

Figure 4.2: Technical drawings with rotors

All rotors must be attached to the wing or the fuselage using dedicated pods. Besides structural purposes, inside the pods, there must be space for electric wires to connect the battery pack and the electric motors. Concerning the variable collective pitch of the front rotors, it is necessary to employ a miniaturized and customized copy of an electric variable pitch hub such as the one developed by Sensenich Propellers [23], shown in Figure 4.3.

Figure 4.3: Electric variable pitch hub

Finally, it is interesting to point out the strong similarity, in terms of rotor positioning, between the Martian UAV and the Joby Aviation eVTOL illustrated in Figure 4.4.

Figure 4.4: Joby Aviation eVTOL rotor configuration [12]

4.2. Trim settings

Similarly to the isolated rotor, four simulations have been performed for the complete model, with the trim settings reported in Table 4.1. As described in the previous chapter, linear relations have been used between the airspeed and the inclination angle (Figure 3.44) and between the inclination angle and the collective pitch angle of the front rotors (Figure 3.31). The RPMs are regulated to match the requirements of vertical and horizontal thrust.

Flight phase	Hover	Transition	Transition	Cruise
Airspeed [m/s]	0	30	60	90
Rear rotor inclination [deg]	90	90	90	90
Front rotor inclination [deg]	90	60	30	0
Rear rotor collective pitch [deg]	30	30	30	30
Front rotor collective pitch [deg]	30	40	50	60
Rear rotor RPMs [1/min]	3,800	3,500	2,400	-
Front rotor RPMs [1/min]	3,800	3,600	3,100	2,400

Table 4.1: Trim settings

4.3. Thrust, torque, and shaft power analysis

Vertical and horizontal thrust trim targets are illustrated in Figure 4.5 and Figure 4.6.

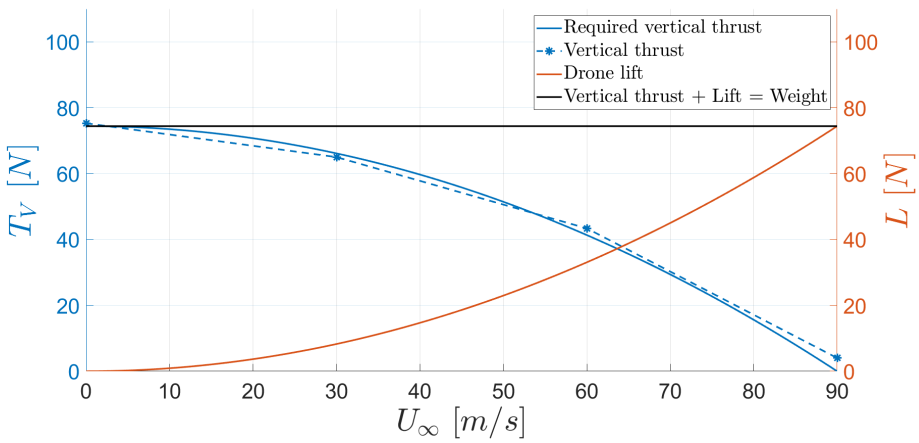

Figure 4.5: Vertical equilibrium of forces vs True airspeed

The vertical thrust generated by the rotors correctly matches the required vertical thrust in all flight phases.

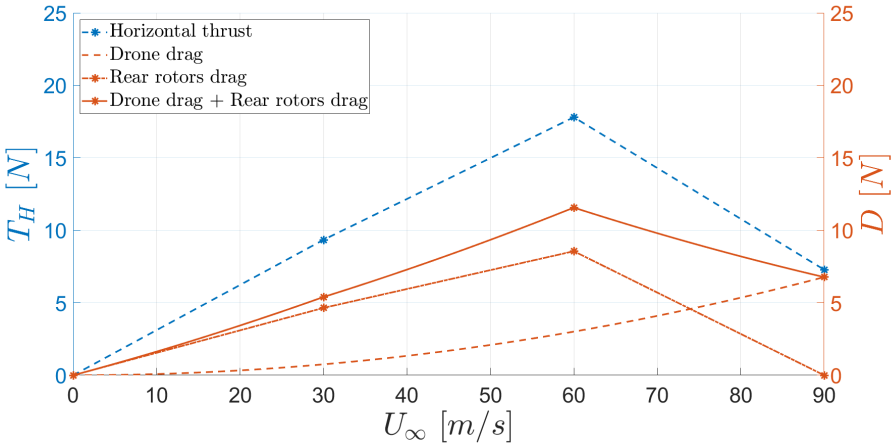

Figure 4.6: Horizontal equilibrium of forces vs True airspeed

The horizontal thrust is greater than the required horizontal thrust in transition, providing an adequate longitudinal acceleration, while equals the UAV drag in cruise. Moreover, Figure 4.7 and Figure 4.8 show the average torque and shaft power of all rotors in all flight phases.

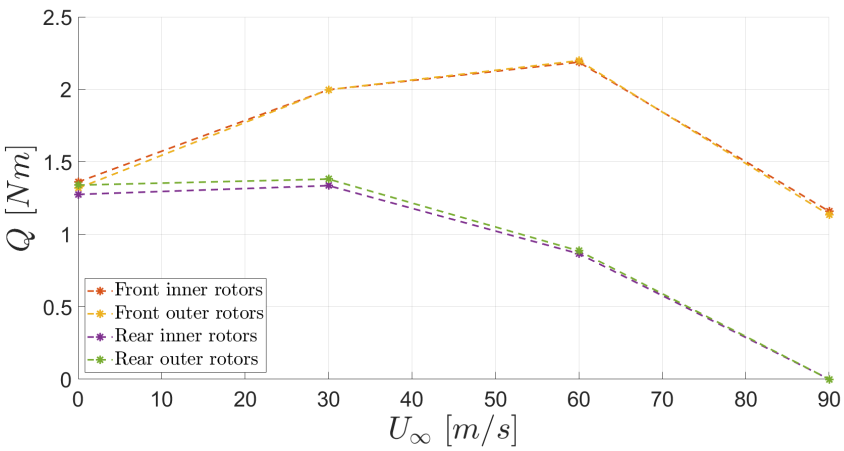

Figure 4.7: Rotor torque vs True airspeed

Due to the different trim settings, the torque features distinct trends for the front and rear rotors. At the same time, there is an almost negligible variation among the inner and the outer rotor positions.

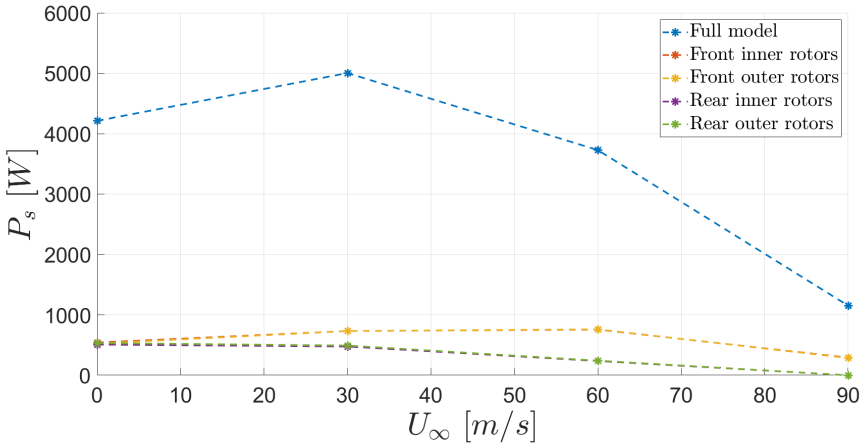

Figure 4.8: Overall shaft power vs True airspeed

The same considerations hold for the shaft power diagram, which also contains the overall shaft power required by the propulsive system. Interestingly, the shaft power in transition at low speed is greater than the shaft power needed at hovering. At low speed, in this case, 30 m/s, the lift generated by the drone is still almost negligible. The propulsive system must generate nearly the same vertical thrust as the hover condition, plus a certain amount of horizontal thrust, that is responsible for the increased shaft power.

4.4. Airplane mode - Cruise

A deeper analysis has been conducted for the cruise phase, especially to understand the mutual interaction between the body and the front rotors. Thanks to its perfect symmetry, only the right part of the drone has been considered.

4.4.1. Loads on the wing

Firstly, the effect of the front rotors on the wing has been investigated. Figure 4.9 shows the velocity flow field in Z-direction on a plane, parallel to the wing leading edge and located at approximately 10 cm distance. The blade tip sections generate an upwash effect when they move upwards, increasing the local angle of attack of the wing. The blade root sections, instead, cause a decrease in local lift in the inboard regions.

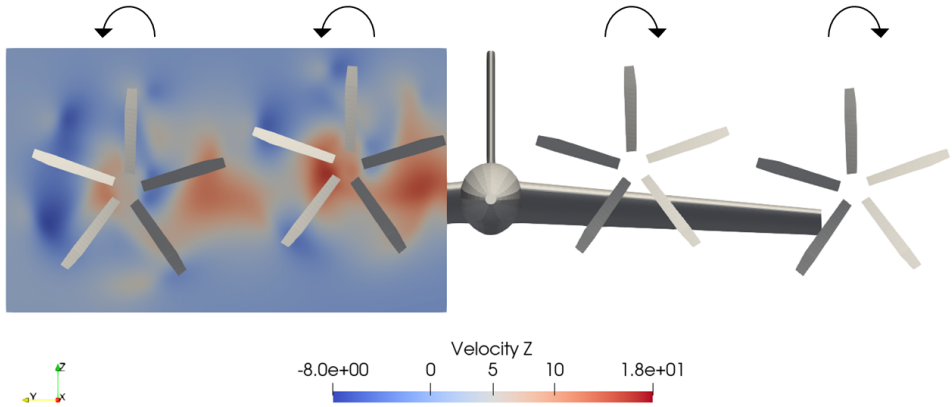

Figure 4.9: Z-direction velocity flow field - front view

Figure 4.10 and Figure 4.11 confirm that the wing portions invested by the helical wakes of the rotors feature, in general, increased surface velocity and reduced pressure coefficient, with some differences due to the inboard-up and the outboard-down blade rotations.

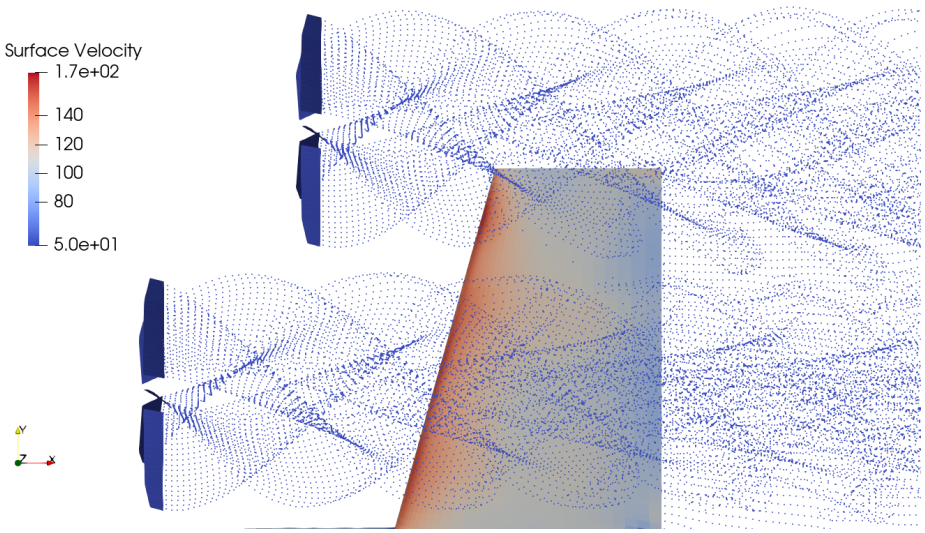

Figure 4.10: Wing surface velocity distribution

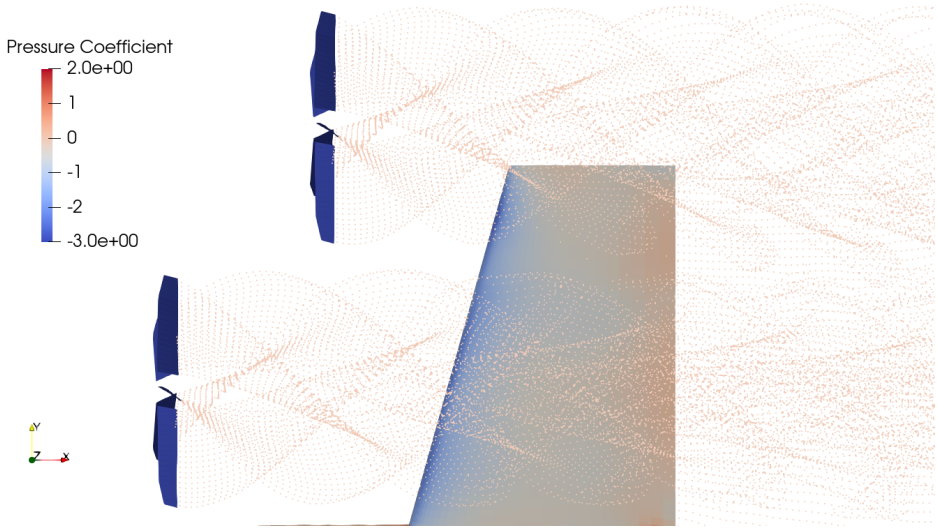

Figure 4.11: Wing pressure coefficient distribution

The latest DUST version still does not allow to retrieve the spanwise loads on an externally generated mesh. Thus, it is not possible to plot the wing lift distribution with and without the presence of the rotors. However, when the rotors are installed, a slightly higher local lift is expected in the inboard-up regions and a lower local lift in the outboard-down regions. The integral loads can be extracted as simulation results. The overall UAV lift generated at an angle of attack of 2° has been retrieved in both cases. Without rotors, the generated lift is 75.5 N, while with rotors, the lift, averaged over the last revolution, is 81.5 N. There is an 8% increment related to the general increased dynamic pressure on the wing.

4.4.2. Loads on the rotors

The global loads generated by the front rotors, averaged over the last revolution, are presented in Table 4.2. Both inner and outer rotors feature increased thrust and shaft power when the wing and the fuselage are present. Moreover, it must be noticed that the outer rotor generates more thrust than the inner rotor despite a lower increase in shaft power. This is probably due to the interaction between its wake and the wingtip vortex, which further enhances its performance.

	ΔT	ΔP_s
Inner rotor	0.06 N (+3.2%)	0.05 W (+4.0%)
Outer rotor	0.09 N (+5.3%)	0.02 W (+1.9%)

Table 4.2: Front rotor variation of thrust and shaft power

Subsequently, the sectional loads on the blades have been analyzed. Figure 4.12a and Figure 4.12b are the contour of the blade non-dimensional normal force, function of the spanwise and the azimuthal locations. Both inner and outer rotor blades generate more thrust at the tip sections with an azimuth angle of approximately 90°.

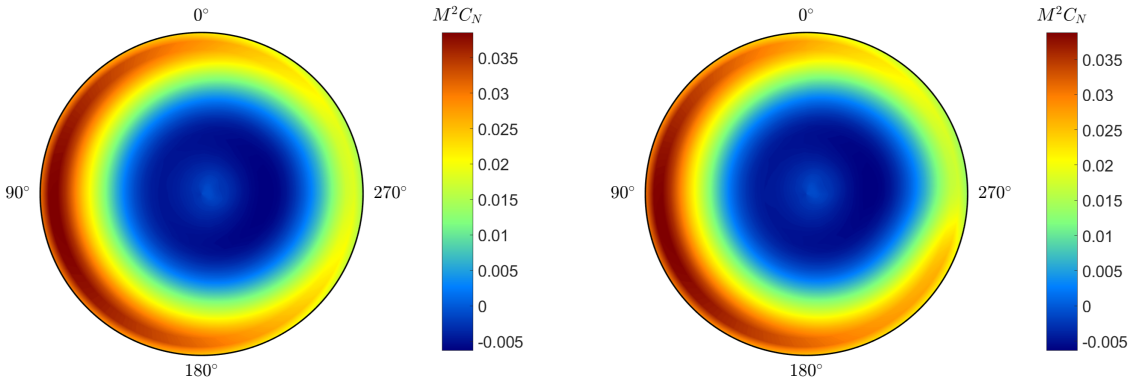

(a) Outer rotor (b) Inner rotor

Figure 4.12: Blade non-dimensional normal force - right side, front view

At this point, it must be mentioned that the UAV flies in cruise with an angle of attack of 2°. Thus, the rotor disk is not perfectly perpendicular to the freestream. When the azimuth angle is 90°, the blade goes down and is subject to an increased velocity component in the plane of the disk, proportional to $sin(\alpha) \approx \alpha$. Conversely, when the azimuth angle is 270° the blade is going up, and the velocity component in the plane of the disk is slightly reduced.

This phenomenon is visible in Figure 4.13a and Figure 4.13b, where the sinusoidal trend of the blade non-dimensional normal force as a function of the azimuth angle is displayed at various spanwise locations. The black ellipses highlight the interaction of the blade of the outer rotor with the wake of the inner rotor and the interaction of the blade of the inner rotor with the fuselage nose, that is more stressed.

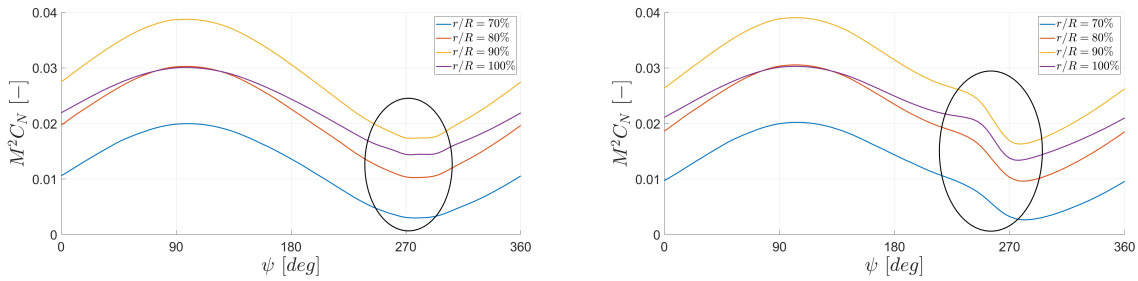

(a) Outer rotor (b) Inner rotor

Figure 4.13: Blade non-dimensional normal force vs Azimuth angle - right side, front view

Figure 4.14a and Figure 4.14b illustrate the blade non-dimensional normal force as a function of the spanwise location for different azimuth angles, with particular attention to the tip losses.

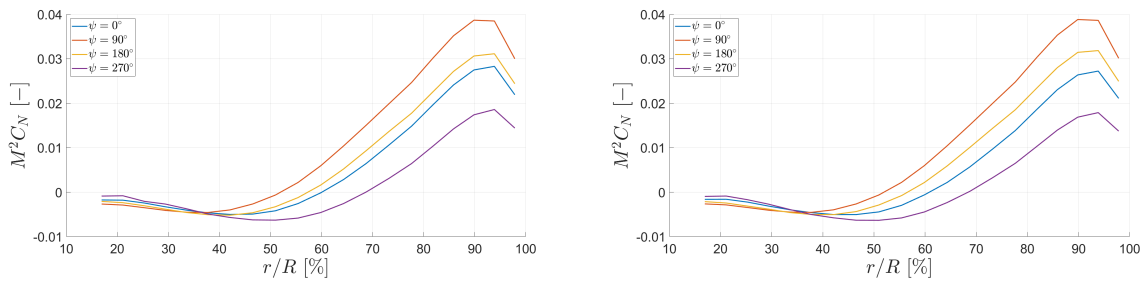

(a) Outer rotor (b) Inner rotor

Figure 4.14: Blade non-dimensional normal force vs Spanwise location - right side, front view

4.5. Transition mode

The transition phase is characterized by complex and strong interactions, with the wake of the front rotors, made of disk vortices, investing both the wing and the rear rotors, as displayed in Figure 4.15. Considering the right side of the UAV, the tilting front rotors rotate anticlockwise with relatively high collective pitch angles while the fixed rear rotors rotate clockwise.

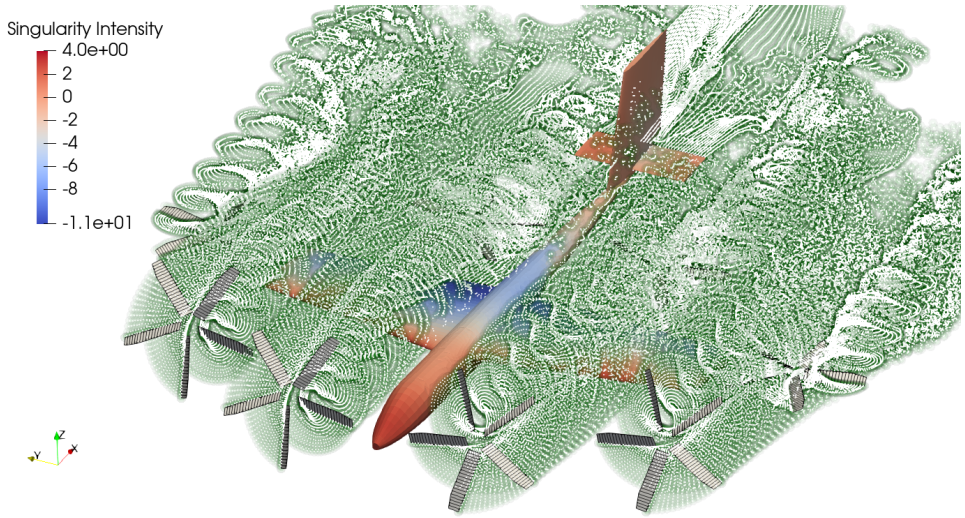

Figure 4.15: Full model in transition at 60 m/s - rotor wake and singularity intensity distribution

The blade non-dimensional normal force of all rotors in this configuration is illustrated in Figure 4.16 and Figure 4.17. Regarding the rear rotors, subject to freestream in the plane of the disk, their contour plots are split into two halves, showing the difference between the advancing blade, which generates most of the thrust, and the retreating blade, with a reverse flow area close to the hub.

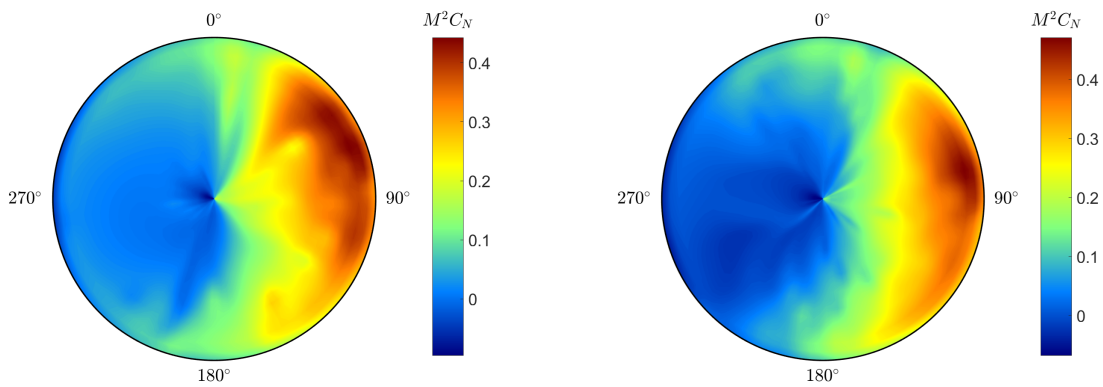

(a) Outer rotor (b) Inner rotor

Figure 4.16: Blade non-dimensional normal force - right rear side, front view

The normal force of the front rotors, similar to what happens in cruise conditions, has a sinusoidal trend as a function of the azimuthal location due to the nacelle inclination angle. This causes higher thrust generation when the blade is at around 90° azimuth angle.

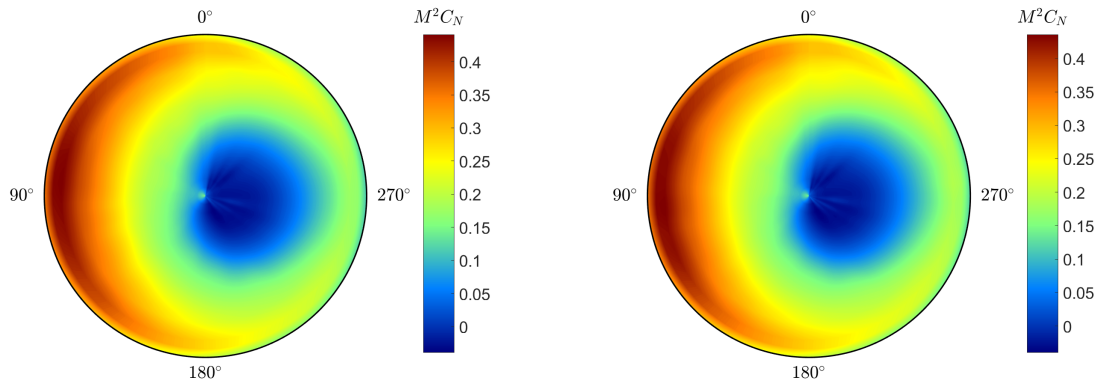

(a) Outer rotor (b) Inner rotor

Figure 4.17: Blade non-dimensional normal force - right front side, front view

4.6. Helicopter mode - Hover

The UAV helicopter mode is characterized by high thrust and shaft power generated by the rotors, whose wakes do not impact any other surface but are free to develop downwards, as illustrated in Figure 4.18. Consequently, the loads generated by the lifting surfaces, particularly the vertical drag, are negligible.

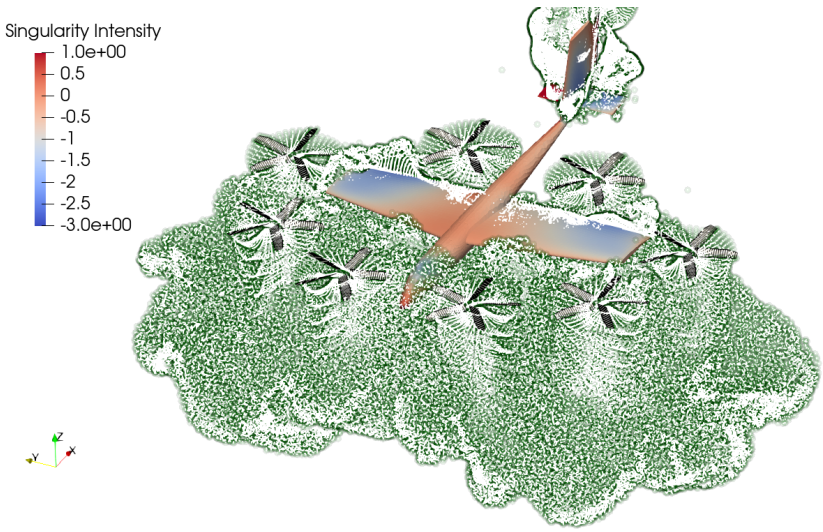

Figure 4.18: Full model at hovering - rotor wake and singularity intensity distribution

DUST well captures the vertical velocity flow field at hover, that is not perfectly symmetrical. Figure 4.19a and Figure 4.19b show the slices passing through the outer and the inner front rotors at convergence. The downward velocity reaches up to about 75 m/s in this flight condition.

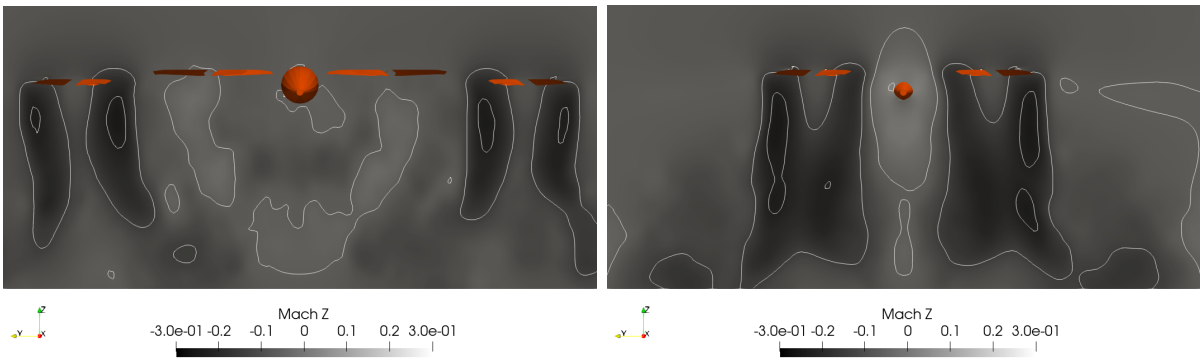

(a) Plane through front outer rotors (b) Plane through front inner rotors

Figure 4.19: Z-direction Mach flow field - front view

Interestingly, the fountain flow above the fuselage with re-ingestion of the flow inside the rotors, typical of tiltrotors, is not present in the Martian UAV. As already mentioned, the wakes of all rotors do not impact the wing and the formation of this phenomenon is not possible. The upwash effect above the fuselage, visible in Figure 4.19b, represents the deviation of the freestream due to the nose shape. When present, the fountain flow develops above the fuselage in correspondence to the wing attachment.

5 | Propulsive system

During the conceptual design phase, performed in [2], the maximum installed shaft power was calculated to be 3,500 W with blade element and momentum theory. This method underestimated the shaft power. Indeed, the mid-fidelity approach with DUST simulations revealed that slightly more than 5,000 W are needed to accomplish the vertical take-off and the transition. Although widely used for Terrestrial rotorcraft, the blade element and momentum theory is quite inefficient at catching the aerodynamic phenomena of the Martian atmosphere, causing such non-negligible discrepancy in the shaft power estimation. Thus, the complete propulsive system, including the battery pack and the electric motors, must be revised and, if needed, modified. Initially, a Li-Metal cell manufactured by Sion Power [24] was adopted, whose specifications are reported in Table 5.1.

Parameter	**Symbol**	**Value**
Gravimetric energy	e^*	450 Wh/kg
Gravimetric power	p^*	1,200 W/kg
Nominal capacity	C	17.5 Ah
Nominal voltage	V	3.8 V
Max C-rate (continuous)	C_{con}^{max}	1 1/h
Max C-rate (180s)	C_{180}^{max}	3 1/h
Mass	M	0.170 kg
Mass factor	ω	0.85

Table 5.1: Technical specifications of Sion Power Li-Metal cell in ideal operative conditions

The battery pack was composed by four cells in series and six cells in parallel, for a total of twenty-four cells and a mass of 4.8 kg. In addition, eight electric motors produced by T-MOTOR [26] were selected. In particular, the model AT2826 3D F3A Fixed Wing Long Shaft Brushless Motor-KV900, whose specifications are reported in Table 5.2, was considered.

Parameter	Symbol	Value
Voltage	V	3S/4S
Max power (180s)	P_s^{max}	800 W
Max current (180s)	i^{max}	57 A
RPMs per Volt	KV	900 RPMs/V
Internal resistance	R_a	0.024 Ω
Mass	M	0.175 kg

Table 5.2: Technical specifications of T-MOTOR AT2826 3D F3A Fixed Wing Long Shaft Brushless Motor-KV900

Firstly, an accurate model of the electric motor, based on its specifications, has been developed to understand whether the propulsive system was still suitable to power the UAV. The torque curve of the electric motor has been created according to Equation 5.1.

$$C_m = \left(\frac{k}{R_a}\right) V_a - \left(\frac{k^2}{R_a}\right) \omega \tag{5.1}$$

where C_m is the motor torque in [Nm], R_a is the internal resistance in [Ω], V_a is the input voltage in [V] regulated by the Electronic Speed Controller (ESC), ω is the rotational speed in [rad/s], and k, expressed in [Nm/A], is related to the KV factor according to Equation 5.2.

$$k = \frac{1}{KV}\left(\frac{60}{2\pi}\right) \tag{5.2}$$

In a DC motor the torque is proportional to the current by means of k, as reported in Equation 5.3.

$$C_m = k \cdot i \tag{5.3}$$

Equation 5.1, parameterized by various input voltages, is shown in Figure 5.1, together with the operative conditions of the motor. The red asterisks represent the resistant torques from the rotors in hover, transition, and climb.

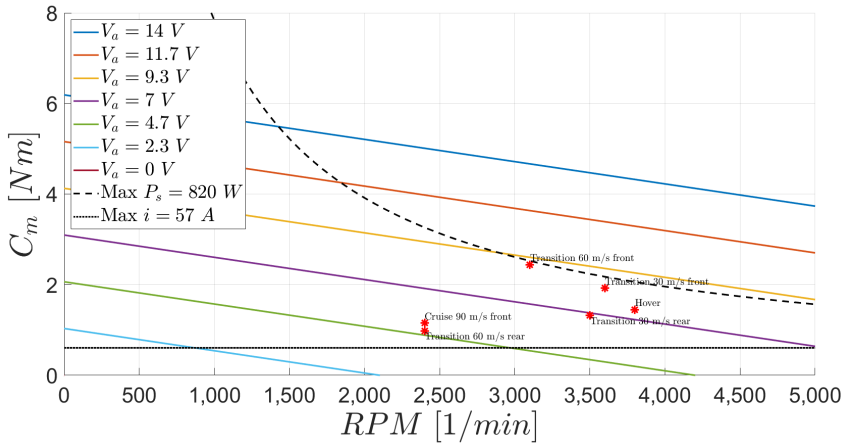

Figure 5.1: Original motor torque curves

The current limitation of the motor prevents the UAV from performing all the flight phases. To overcome this problem, another electric motor, still manufactured by T-MOTOR, has been selected. The KV factor reported in Table 5.2 indicates the number of revolutions per second per Volt that the motor performs when it is load-free, meaning without any rotor attached. Generally, a rotor with a large diameter, such as the one employed for the Martian UAV, is subject to a larger resistant torque and rotates slower than a rotor with a smaller diameter. Low KV values are more appropriate for rotors requiring high torque and with low RPM values. The model MN705-S IP45 Navigator Type UAV Multi-Motor KV260 -2PCS/SET has been chosen. Its specifications are listed in Table 5.3.

Parameter	Symbol	Value
Voltage	V	6S
Max power (180s)	P_s^{max}	2,000 W
Max current (180s)	i^{max}	80 A
RPMs per Volt	KV	260 RPMs/V
Internal resistance	R_a	0.016 Ω
Mass	M	0.450 kg

Table 5.3: Technical specifications of T-MOTOR MN705-S IP45 Navigator Type UAV Multi-Motor KV260 -2PCS/SET

This motor, unlike the previous one, requires six cells in series. In addition, its mass is almost three times higher. Later in this chapter, some considerations about the mass

increment of the propulsive system are made. The torque curves of the new motor are illustrated in Figure 5.2.

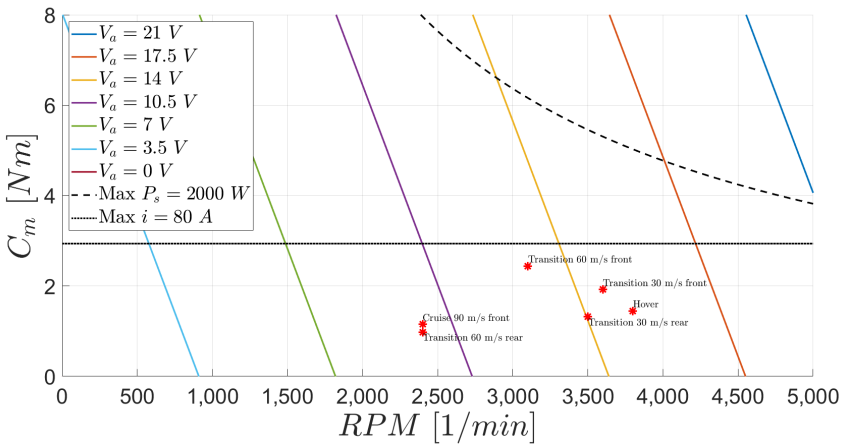

Figure 5.2: New motor torque curves

The new motor satisfies all requirements regarding resistant torque since all flight phases are below the current limitation line. After modifying the number of cells in series from four to six, it is necessary to check whether the original six cells in parallel are sufficient. The number of cells in parallel is dictated by the current and power constraints, which are equivalent if the cell nominal voltage is used, and by the capacity constraint. Considering an average current of 60 A through all motors as the most demanding scenario, the battery pack must supply 480 A. With six cells in parallel, 80 A must be supplied by each cell. According to Table 5.1, the maximum current is about 50 A for at most 180 s and 17.5 A continuously.

In conclusion, the number of cells in parallel should be increased to nine, for a total of fifty-four cells and a mass of 10.8 kg. This is a critical issue. The mass of the battery pack has increased from 4.8 kg to 10.8 kg.
The limiting factor is the low C-rate of the cell, which does not allow a high current supply. It is necessary to find a cell with higher C-rate values. A Li-Metal cell produced by CRG [3] in the U.S. is optimal for low-temperature applications. Its specifications are reported in Table 5.4.

Parameter	Symbol	Value
Gravimetric energy	e^*	260 Wh/kg
Gravimetric power	p^*	4,100 W/kg
Nominal capacity	C	6.1 Ah
Nominal voltage	V	3.8 V
Max C-rate (continuous)	C_{con}^{max}	16 1/h
Mass	M	0.090 kg
Mass factor	ω	0.90

Table 5.4: Technical specifications of CRG Li-Metal cell in ideal operative conditions

It must be pointed out that these specifications are only valid when the cell operates in ideal conditions. The effects of temperature and discharge rate are illustrated in Figure 5.4 and Figure 5.3.

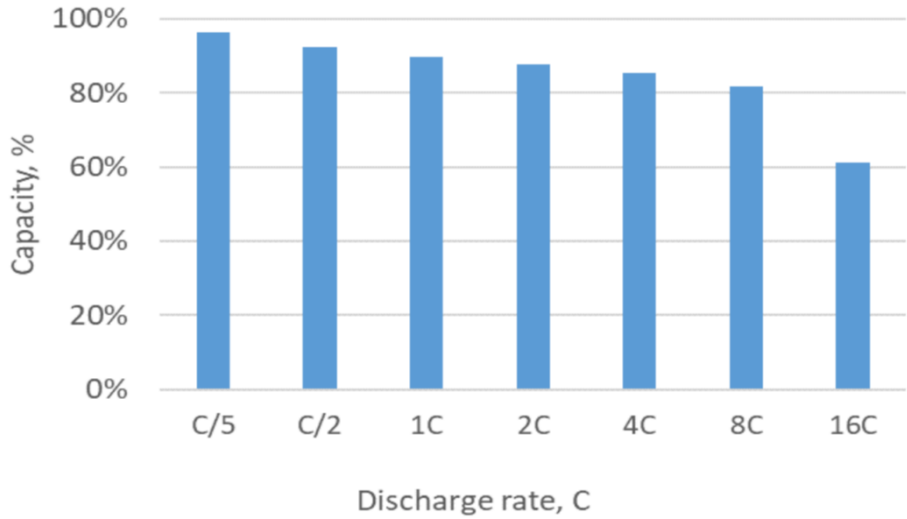

Figure 5.3: C-rate performance. Charge: C/2, 4.5 V. Discharge: 2.7 V [3]

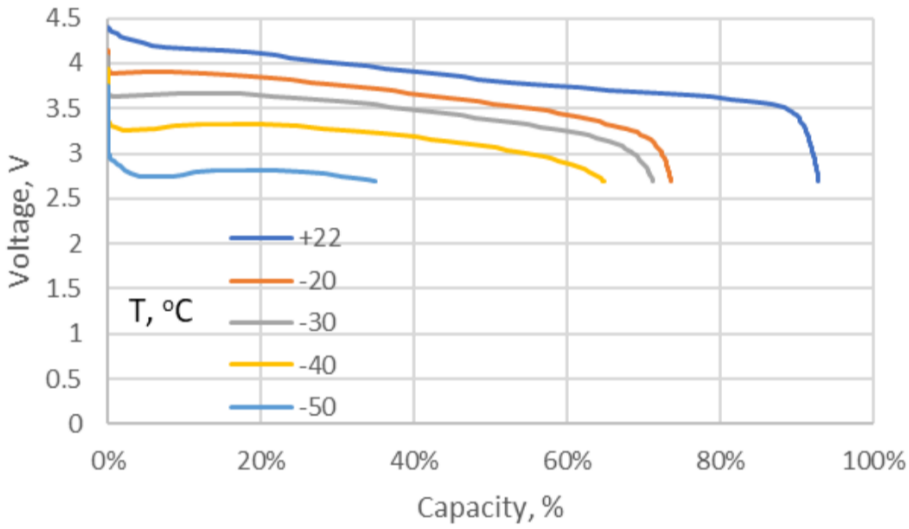

Figure 5.4: Temperature performance. Charge: C/2, 4.5 V. Discharge: C/2, 2.7 V [3]

According to the experiments carried out by the manufacturer, the nominal capacity is reduced by 40% when high C-rates are used to discharge the cell and by 30% at -30 °C. Moreover, due to low temperatures, the nominal voltage is about 3.5 V. Table 5.5 contains the specifications of the cell when it is employed in such operative conditions.

Parameter	Symbol	Value
Gravimetric energy	e^*	100 Wh/kg
Gravimetric power	p^*	1,600 W/kg
Nominal capacity	C	2.6 Ah
Nominal voltage	V	3.5 V
Max C-rate (continuous)	C_{con}^{max}	16 1/h
Mass	M	0.090 kg
Mass factor	ω	0.90

Table 5.5: Technical specifications of CRG Li-Metal cell in Mars operative conditions

Figure 5.5 illustrates the life cycle performance of the cell in ideal conditions. It is safe to assume that 100 life cycles can be achieved in the Martian environment.

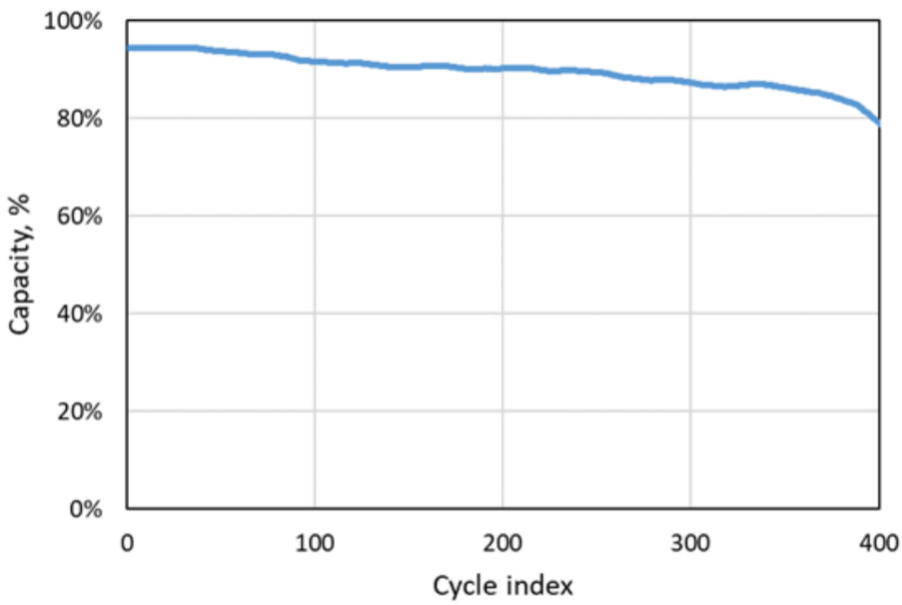

Figure 5.5: Life cycle performance. Room temperature. Charge: C/5, 4.5 V. Discharge: C/5, 2.7 V [3]

At this point, a new battery pack must be sized. According to the electric motor requirement, the number of cells in series has been fixed to six. Adopting the previous procedure, the number of cells in parallel has been set to twelve. The maximum current supplied by every cell in flight is 40 A, which corresponds to a C-rate of about 15 1/h, consistent with the specifications. The mass of the definitive battery pack, composed of seventy-two cells, is 7.2 kg, reasonably higher than the initial mass estimated in the conceptual design (4.8 kg) but lower than the mass of the modified battery pack with old cells (10.8 kg). The capacity of the battery pack, with twelve cells in parallel, is 31.2 Ah. The energy stored, considering six cells in series, is 655 Wh. The initial requirement of 200 km mission range must be relaxed to 70 km due to the higher shaft power absorbed in all flight phases. Table 5.6 contains the shaft power and energy breakdown.

Flight phase	Average shaft power [W]	Time [s]	Energy [Wh]
Take-off	5,100	30	42
Transition	4,400	60	73
Climb	2,500	30	21
Cruise (70 km)	1,100	780	250
Descent	500	60	9
Transition	2,200	60	37
Landing	4,200	30	35
Overall mission	-	1,050	467

Table 5.6: Flight phase shaft power and energy requirements

Considering a 90% efficiency for the electric motors, 520 Wh of energy must be used. The mission is expected to be completed with at least a 20% state of charge. Concerning the mass of the new propulsive system, an increment of 4.6 kg, 2.4 kg for the battery pack, and 2,2 kg for the electric motors must be managed. Thanks to technological advancements in aerospace materials and constructive methods, it might be possible to reduce the masses of the wing and the fuselage slightly. Nevertheless, constructing a prototype is mandatory to estimate the real masses of all components and their structural properties. It is also possible to reduce the surface, and therefore the mass, of the solar panels, but more time would be required to recharge the battery pack. Furthermore, in the next 10/15 years, a significant improvement may be expected for electric components and miniaturized equipment.

These considerations justify the fact that the maximum take-off mass of the UAV has not been modified but kept to 20 kg, as decided in the conceptual design.

6 | Stability analysis

In this chapter, the mid-fidelity software DUST is used to compute the UAV static and dynamic stability derivatives. Firstly, the numerical model is presented, and subsequently, the UAV rigid modes and its flying qualities in cruise are analyzed.

6.1. Numerical model

Under the hypothesis of linear aerodynamics, the forces and moments acting on the UAV have a linear behavior with respect to the angle of attack and its derivative, to the angle of sideslip and its derivative, and the three angular rates. Moreover, thanks to the symmetry of the UAV and its traditional tail-aft configuration, it is assumed that the longitudinal and lateral-directional dynamics can be fully decoupled.

The static stability derivatives, depending on the angle of attack and the angle of sideslip, have been calculated by performing static simulations at several angles. The dynamic stability derivatives, depending on the rate-of-change of the angle of attack and sideslip and angular rates, have been calculated by imposing sinusoidal motions about the roll, pitch, and yaw axes and by using the single-point method [10]. It must be pointed out that the oscillations in pitch and yaw only allow to retrieve the composed derivatives in $(q + \dot{\alpha})$ and in $(r - \dot{\beta})$. Vertical plunge and lateral plunge motions have to be applied to obtain the derivatives in $(\dot{\alpha})$ and $(\dot{\beta})$, and the corresponding decoupled contributions in (q) and (r). The body reference frame, with conventions for angles, angular rates, forces, and moments, is illustrated in Figure 6.1. The relation between the forces expressed in the body reference frame and the aerodynamic forces, assuming small angles, is reported in Equation 6.1.

$$\begin{cases} X \approx -D + L\alpha - S\beta \\ Y \approx -S \\ Z \approx -L \end{cases} \tag{6.1}$$

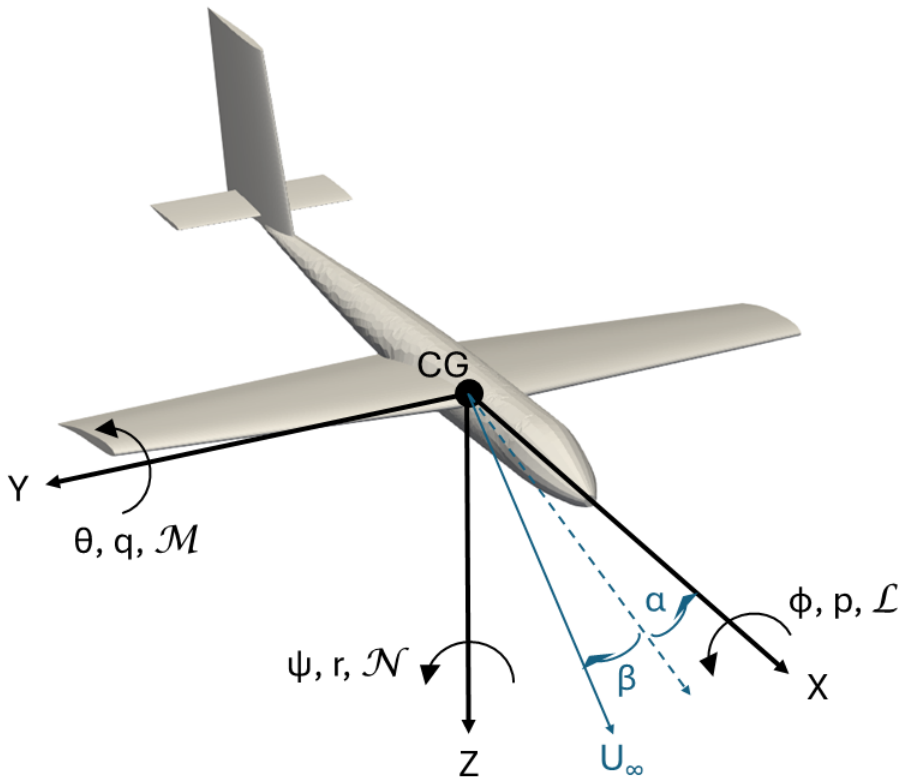

Figure 6.1: Body reference frame with sign conventions

All the simulations described in this chapter have been advanced in time for 2 s with an asymptotic velocity of 90 m/s. The frequency of the dynamic roll, pitch, and yaw oscillations and the plunge motions has been set to 1 Hz, and a sensitivity analysis on the time step has been performed. 160 time steps per period have been adopted to obtain time-independent and accurate solutions. In addition, the domain length has been set to 30 m, representing about 35 chords, since the wake is not supposed to affect the loads on the UAV at greater distances. Table 6.1 contains detailed information about the settings used to perform the static and dynamic simulations.

Motion	α_0 [deg]	β_0 [deg]	Δs [m]	$\Delta\phi$ [deg]	$\Delta\theta$ [deg]	$\Delta\psi$ [deg]
Static α	-2 to 8	0	-	-	-	-
Static β	0	-5 to 5	-	-	-	-
Roll	2	0	-	-5 to 5	0	0
Pitch	2	0	-	0	-5 to 5	0
Yaw	2	0	-	0	0	-5 to 5
Vertical plunge	0	0	-1.25 to 1.25	-	-	-
Lateral plunge	0	0	-1.25 to 1.25	-	-	-

Table 6.1: Stability derivative simulation settings

6.2. Calculation of static stability derivatives

For all the static simulations, the integral loads have been extracted at the end of the initial transient when the solution reached stationary conditions.

6.2.1. Static angle of attack

Figure 6.2 shows the trends of the longitudinal and vertical forces and the pitching moment coefficients as a function of the angle of attack.

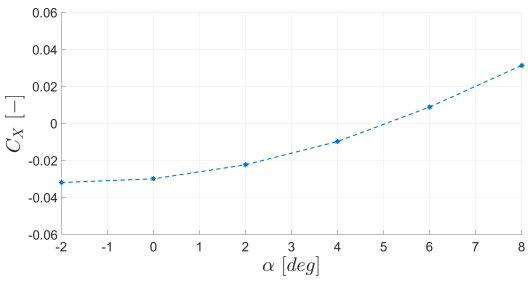

(a) Longitudinal force coefficient vs AoA

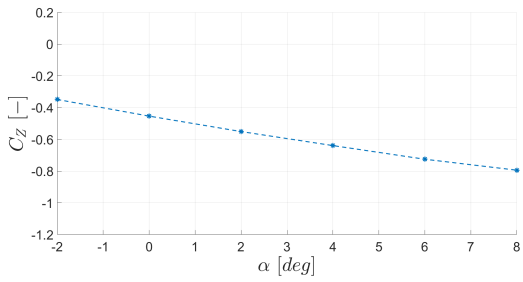

(b) Vertical force coefficient vs AoA

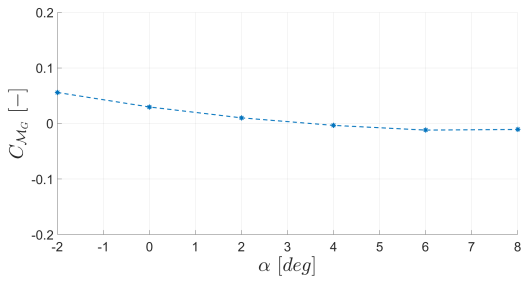

(c) Pitching moment coefficient vs AoA

Figure 6.2: Static angle of attack simulations

The static stability derivatives have been calculated by means of linear approximation about the cruising attitude of 2° and reported in Table 6.2. The longitudinal static stability criterion, which requires the pitching moment coefficient derived with respect to alpha to be negative, is satisfied.

Stability derivative	Value [-]
C_{X_α}	0.36
C_{Z_α}	-2.56
$C_{\mathcal{M}_{G_\alpha}}$	-0.39

Table 6.2: Static angle of attack stability derivatives

6.2.2. Static angle of sideslip

The results obtained from the static simulations for the angle of sideslip, with the same format used for the angle of attack, are shown in Figure 6.3.

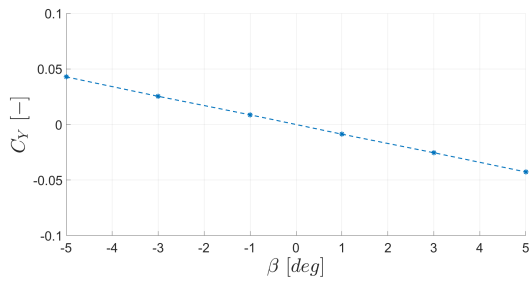

(a) Lateral force coefficient vs AoS

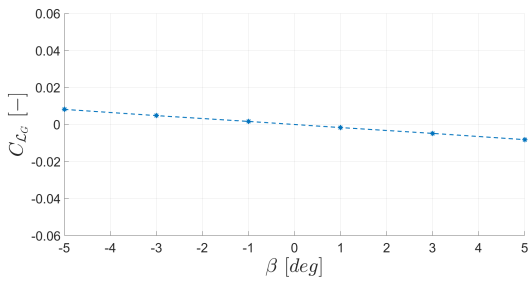

(b) Rolling moment coefficient vs AoS

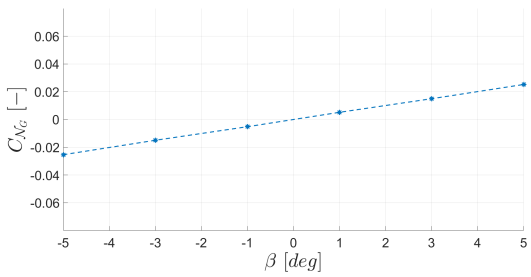

(c) Yawing moment coefficient vs AoS

Figure 6.3: Static angle of sideslip simulations

The lateral and the directional static stability criteria, respectively, require the rolling moment coefficient and the yawing moment coefficient derived with respect to beta to be negative and positive. Both requirements are met, as reported in Table 6.3.

Stability derivative	Value [-]
C_{Y_β}	-0.49
$C_{\mathcal{L}_{G_\beta}}$	-0.09
$C_{\mathcal{N}_{G_\beta}}$	0.29

Table 6.3: Static angle of sideslip stability derivatives

6.3. Calculation of dynamic stability derivatives

This section presents the results obtained with DUST about the dynamic stability derivatives involving periodic oscillations about the roll, pitch, and yaw axes.

6.3.1. Roll oscillation

Equation 6.2 represents the imposed sinusoidal rolling motion, with an amplitude of 5° and a frequency of 1 Hz. The roll rate is related to the derivative of the roll angle.

$$\begin{cases} \Delta\phi(t) = \phi_A \sin(\omega t) \\ p(t) = \Delta\dot{\phi}(t) = \phi_A \omega \cos(\omega t) \end{cases} \tag{6.2}$$

The visualization of the periodic oscillation about the roll axis is shown in Figure 6.4. The motion-induced variation of the pressure coefficient on the upper surface of the wing is evident.

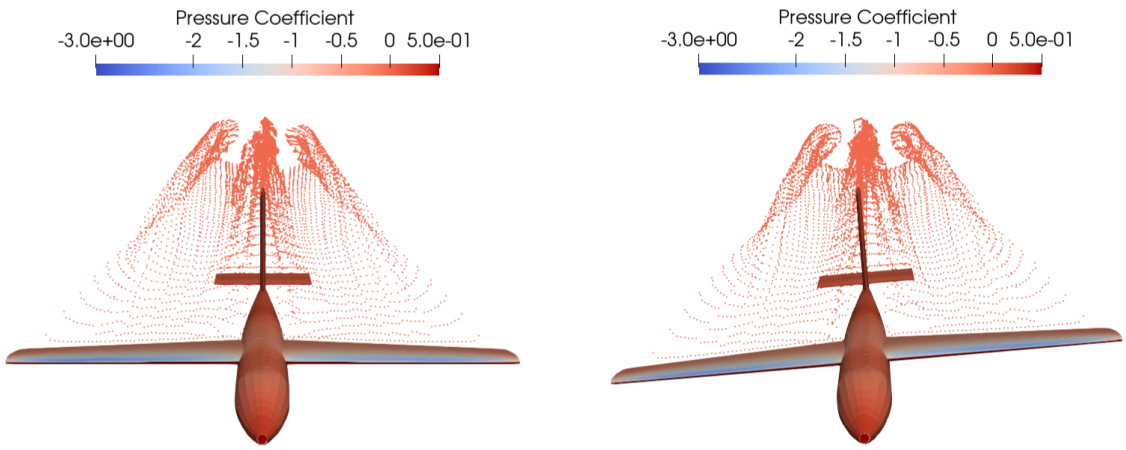

(a) $\Delta\phi = 0°, t = 0T$ (b) $\Delta\phi = 5°, t = 0.25T$

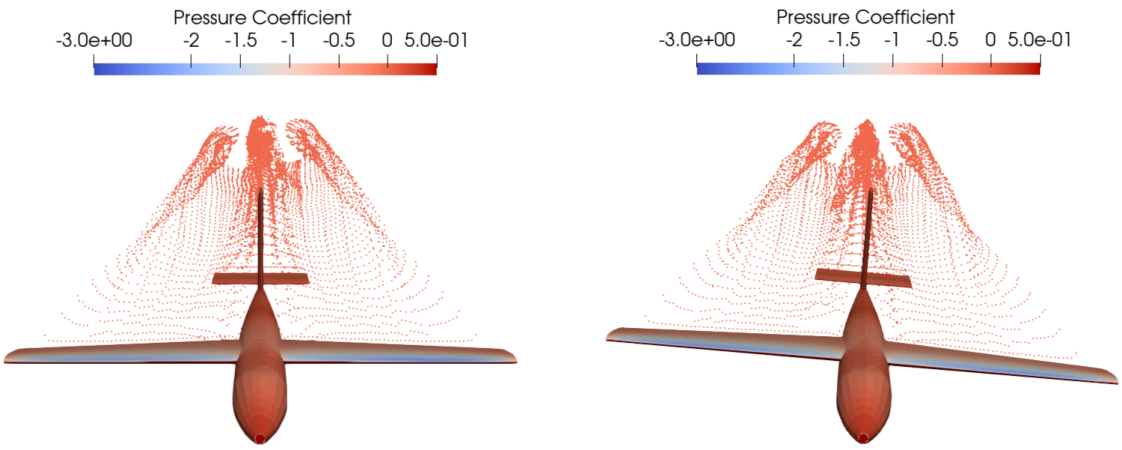

(c) $\Delta\phi = 0°, t = 0.50T$ (d) $\Delta\phi = -5°, t = 0.75T$

Figure 6.4: Roll oscillation

The resulting integral loads of the lateral-directional dynamics are illustrated in Figure 6.5. All forces and moments feature elliptic shapes whose amplitudes at the reference condition are strictly related to the dynamic stability derivatives.

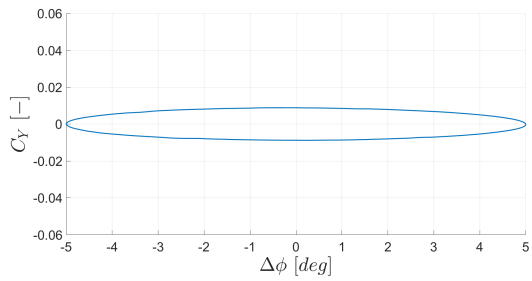

(a) Lateral force coefficient vs Roll angle

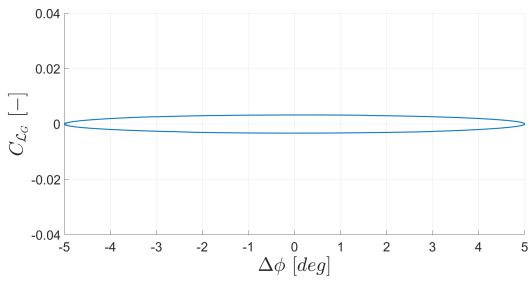

(b) Rolling moment coefficient vs Roll angle

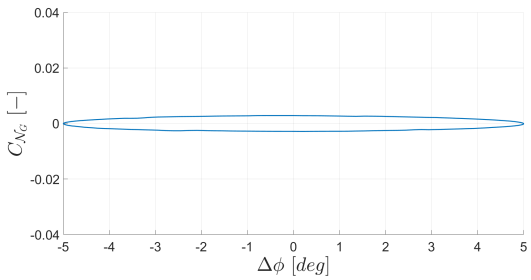

(c) Yawing moment coefficient vs Roll angle

Figure 6.5: Dynamic roll simulations

The dynamic stability derivatives with respect to the roll rate, calculated with the single point method, are reported in Table 6.4.

Stability derivative	Value [-]
C_{Y_p}	-0.96
$C_{\mathcal{L}_{G_p}}$	-0.36
$C_{\mathcal{N}_{G_p}}$	-0.31

Table 6.4: Dynamic roll stability derivatives

6.3.2. Pitch oscillation

The sinusoidal pitching motion, with the same amplitude and frequency used for the rolling motion, is described by Equation 6.3. The variation of pitch angle is equal to the variation of angle of attack, since null climb angle has been considered.

$$\begin{cases} \Delta\theta(t) = \Delta\alpha(t) = \theta_A \sin(\omega t) \\ q(t) = \Delta\dot{\theta}(t) = \Delta\dot{\alpha}(t) = \theta_A \omega \cos(\omega t) \end{cases} \tag{6.3}$$

The pitching motion is visualized in Figure 6.6. Highly negative pressure coefficient on the upper surface of the wing is visible with pitch-up attitude and pitch-down velocity (Figure 6.6b).

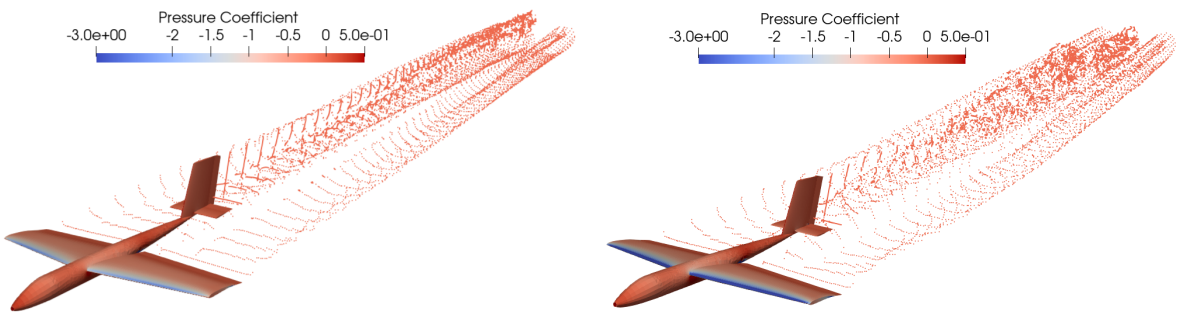

(a) $\Delta\theta = 0°, t = 0T$ (b) $\Delta\theta = 5°, t = 0.25T$

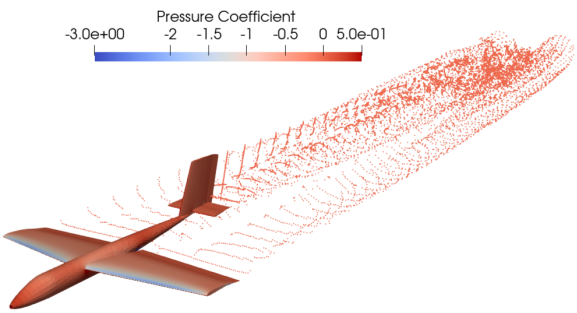

(c) $\Delta\theta = 0°, t = 0.50T$

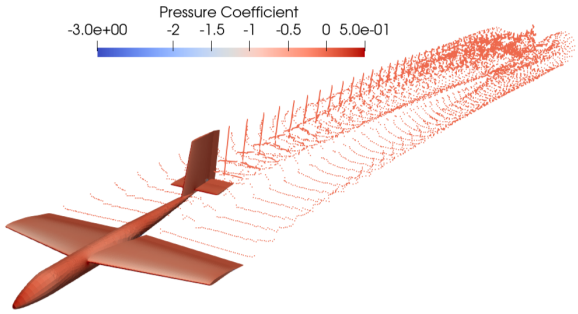

(d) $\Delta\theta = -5°, t = 0.75T$

Figure 6.6: Pitch oscillation

The coefficients of longitudinal and vertical forces and pitching moment are illustrated in Figure 6.7. Unlike the perfectly symmetrical behavior of the loads for the rolling motion, in this case, there are non-uniform trends.

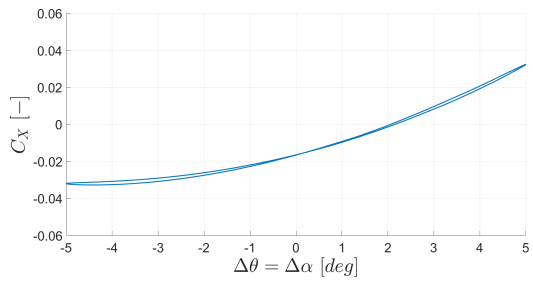

(a) Longitudinal force coefficient vs Pitch angle

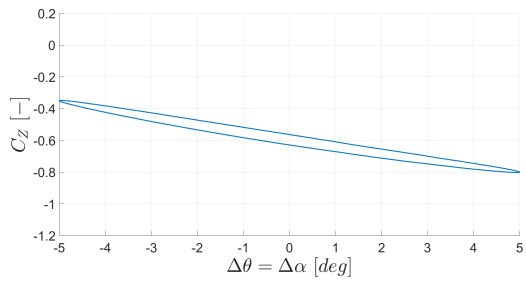

(b) Vertical force coefficient vs Pitch angle

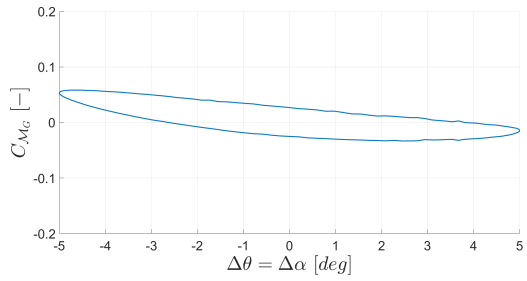

(c) Pitching moment coefficient vs Pitch angle

Figure 6.7: Dynamic pitch simulations

The composed dynamic stability derivatives with respect to pitch rate and rate-of-change of the angle of attack are gathered in Table 6.5.

Stability derivative	Value [-]
$C_{X_q} + C_{X_{\dot{\alpha}}}$	-0.26
$C_{Z_q} + C_{Z_{\dot{\alpha}}}$	-10.93
$C_{\mathcal{M}_{G_q}} + C_{\mathcal{M}_{G_{\dot{\alpha}}}}$	-9.66

Table 6.5: Dynamic pitch stability derivatives

6.3.3. Yaw oscillation

The sinusoidal yawing motion, with the same previous numerical characteristics, is reported in Equation 6.4. The variation of the yaw angle is equal and opposite to the variation of the angle of the sideslip, according to the definition of the body reference frame.

$$\begin{cases} \Delta\psi(t) = -\Delta\beta(t) = \psi_A \sin(\omega t) \\ r(t) = \Delta\dot{\psi}(t) = -\Delta\dot{\beta}(t) = \psi_A \omega \cos(\omega t) \end{cases} \tag{6.4}$$

The yawing motion is shown in Figure 6.8. Mild variations of pressure coefficient are visible on the upper surface of the wing due to the either increased or reduced velocity caused by the motion.

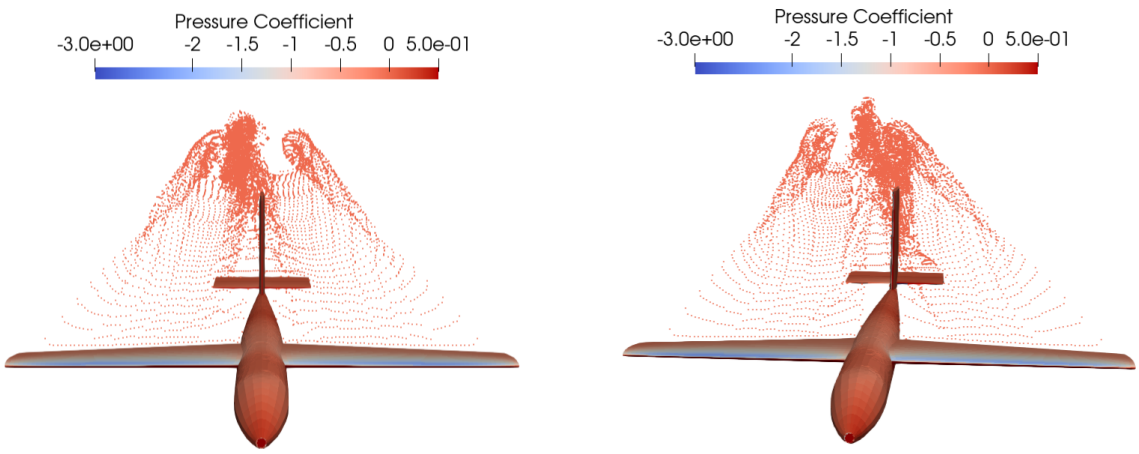

(a) $\Delta\psi = 0°, t = 0T$ (b) $\Delta\psi = 5°, t = 0.25T$

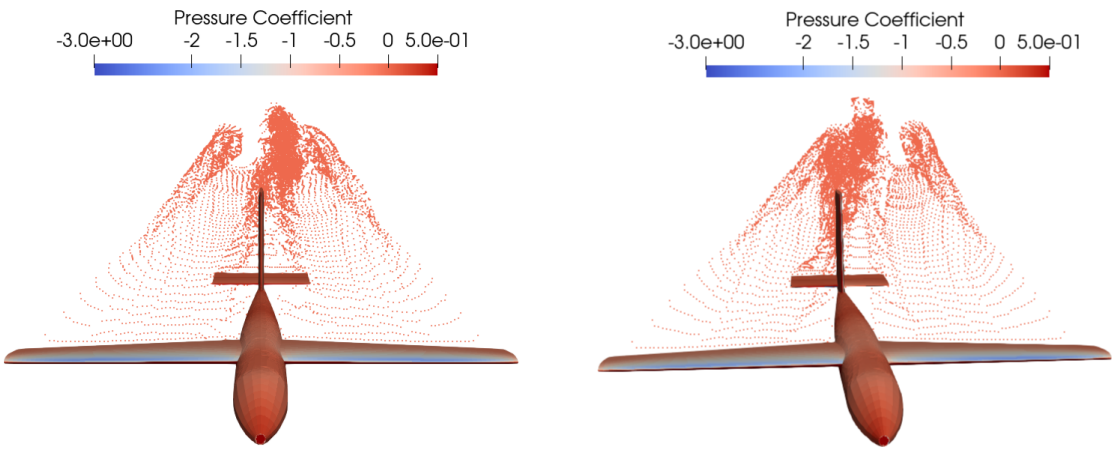

(c) $\Delta\psi = 0°, t = 0.50T$ (d) $\Delta\psi = -5°, t = 0.75T$

Figure 6.8: Yaw oscillation

The coefficients of lateral force and rolling and yawing moments are illustrated in Figure 6.9, with symmetrical behavior as well as for the rolling motion.

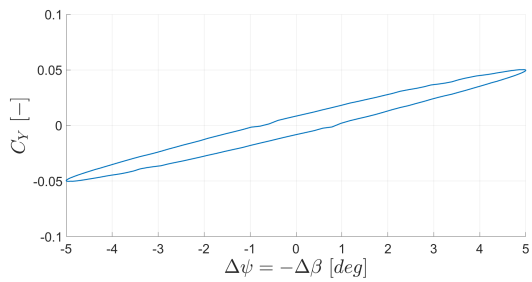

(a) Lateral force coefficient vs Yaw angle

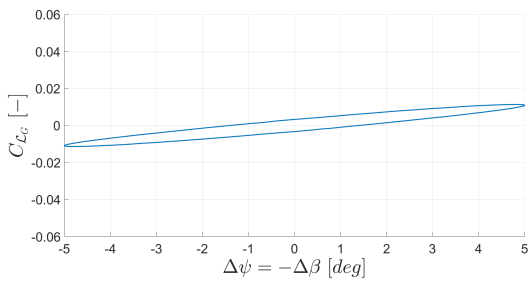

(b) Rolling moment coefficient vs Yaw angle

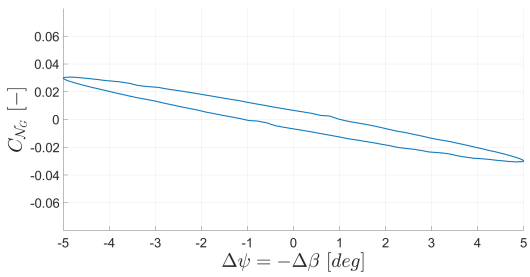

(c) Yawing moment coefficient vs Yaw angle

Figure 6.9: Dynamic yaw simulations

Table 6.6 contains the composed dynamic stability derivatives with respect to yaw rate and rate-of-change of angle of sideslip.

Stability derivative	Value [-]
$C_{Y_r} - C_{Y_{\dot{\beta}}}$	0.81
$C_{\mathcal{L}_{G_r}} - C_{\mathcal{L}_{G_{\dot{\beta}}}}$	0.34
$C_{\mathcal{N}_{G_r}} - C_{\mathcal{N}_{G_{\dot{\beta}}}}$	-0.67

Table 6.6: Dynamic yaw stability derivatives

6.3.4. Vertical plunge oscillation

The vertical plunge motion is characterized by a null variation of pitch angle. Conversely, the angle of attack changes according to the vertical motion expression, summarized in Equation 6.5. In particular, the angle of attack presents a phase with respect to the vertical position, whose value is $\pi/2$.

$$\begin{cases} \Delta z(t) = z_A \sin(\omega t) \\ \Delta \dot{z}(t) = z_A \omega \cos(\omega t) \\ \alpha_A = \dfrac{z_A \omega}{U_\infty} \\ \alpha_P = \dfrac{\pi}{2} \\ \Delta \alpha(t) = \alpha_A \sin(\omega t + \alpha_P) \\ \Delta \dot{\alpha}(t) = \alpha_A \omega \cos(\omega t + \alpha_P) \end{cases} \tag{6.5}$$

As previously mentioned, the vertical plunge motion is needed to decouple the longitudinal dynamic stability derivatives. Each decoupled contribution, obtained with the same methods applied to the periodic loads, is reported in Table 6.7.

Stability derivative	Value [-]
$C_{X_{\dot{\alpha}}}$	-0.15
C_{X_q}	-0.11
$C_{Z_{\dot{\alpha}}}$	-3.41
C_{Z_q}	-7.52
$C_{\mathcal{M}_{G_{\dot{\alpha}}}}$	-4.27
$C_{\mathcal{M}_{G_q}}$	-5.39

Table 6.7: Vertical plunge stability derivatives

6.3.5. Lateral plunge oscillation

Similarly, the lateral plunge motion, characterized by a null variation of yaw angle, is required to decouple the lateral-directional dynamic stability derivatives. Similar expressions have been used to define the motion, as illustrated in Equation 6.6.

$$\begin{cases} \Delta y(t) = y_A \sin(\omega t) \\ \Delta \dot{y}(t) = y_A \omega \cos(\omega t) \\ \beta_A = \dfrac{y_A \omega}{U_\infty} \\ \beta_P = \dfrac{\pi}{2} \\ \Delta \beta(t) = \beta_A \sin(\omega t + \beta_P) \\ \Delta \dot{\beta}(t) = \beta_A \omega \cos(\omega t + \beta_P) \end{cases} \tag{6.6}$$

All the decoupled contributions are put together in Table 6.8 for completeness. As expected, the contributions related to the rate-of-change of the angle of sideslip are almost negligible compared to those related to the yaw rate.

Stability derivative	Value [-]
$C_{Y_{\dot{\beta}}}$	-0.13
C_{Y_r}	0.68
$C_{\mathcal{L}_{G_{\dot{\beta}}}}$	-0.01
$C_{\mathcal{L}_{G_r}}$	0.33
$C_{\mathcal{N}_{G_{\dot{\beta}}}}$	0.08
$C_{\mathcal{N}_{G_r}}$	-0.59

Table 6.8: Lateral plunge stability derivatives

6.4. Eigenvalues and flying qualities

The primary objective of the calculation of the stability derivatives is the comprehensive depiction of both longitudinal modes (phugoid, short period) and lateral-directional modes (roll subsidence, dutch roll, spiral, zero-root), whose corresponding eigenvalues provide useful information about the UAV dynamic stability. The following expressions have been used to extract the natural frequency and the damping ratio of the complex and conjugate eigenvalues and the real part of the real eigenvalues.

$$\begin{cases} \omega_{PH} = \sqrt{2}\dfrac{g}{U_0} \\ \xi_{PH} = \dfrac{1}{\frac{L}{D}\sqrt{2}} \end{cases} \tag{6.7}$$

$$\begin{cases} \omega_{SP} = \sqrt{\dfrac{c_1\, C_{Z_\alpha}\, C_{\mathcal{M}_q}}{m_1\, J_{y_1}} - \dfrac{C_{\mathcal{M}_\alpha}}{J_{y_1}}} \\ \xi_{SP} = -\dfrac{\frac{C_{Z_\alpha}}{m_1} + \frac{c_1}{J_{y_1}}(C_{\mathcal{M}_q} + C_{\mathcal{M}_{\dot\alpha}})}{2\omega_{SP}} \end{cases} \tag{6.8}$$

$$\left\{ \lambda_R = \frac{b_1\, C_{\mathcal{L}_p}}{J_{x_1}} \right. \tag{6.9}$$

$$\left\{ \lambda_{SPI} = \frac{b_1}{J_{z_1}} \frac{1}{C_{\mathcal{L}_\beta}} (C_{\mathcal{L}_\beta} C_{\mathcal{N}_r} - C_{\mathcal{L}_r} C_{\mathcal{N}_\beta}) \right. \tag{6.10}$$

$$\begin{cases} \omega_{DR} = \sqrt{\dfrac{b_1 C_{Y_\beta} C_{\mathcal{N}_r} + C_{\mathcal{N}_\beta}(m_1 - b_1 C_{Y_r})}{m_1 J_{z_1}}} \\ \xi_{DR} = -\dfrac{1}{2\omega_{DR}} \left(\dfrac{C_{Y_\beta}}{m_1} + \dfrac{b_1 C_{\mathcal{N}_r}}{J_{z_1}} \right) \end{cases} \tag{6.11}$$

where U_0 and ρ_0 are the airspeed and the density in the reference condition and c_1, b_1, m_1, J_{x_1}, J_{y_1}, J_{z_1} are defined in Equation 6.12.

$$\begin{cases} c_1 = \dfrac{c}{2U_0} \\ b_1 = \dfrac{b}{2U_0} \\ m_1 = \dfrac{M}{\frac{1}{2}\rho_0 U_0 S} \\ J_{x_1} = \dfrac{J_{xx}}{\frac{1}{2}\rho_0 U_0^2 S b} \\ J_{y_1} = \dfrac{J_{yy}}{\frac{1}{2}\rho_0 U_0^2 S c} \\ J_{z_1} = \dfrac{J_{zz}}{\frac{1}{2}\rho_0 U_0^2 S b} \end{cases} \tag{6.12}$$

Figure 6.10 and Figure 6.11 respectively show the maps of the longitudinal and the lateral-directional eigenvalues in cruise. All eigenvalues have negative real part, except for the spiral mode. However, typically, a mild instability is accepted. The next step consists of assessing the flying qualities of the UAV and discussing the implementation of a Stability Augmentation System (SAS).

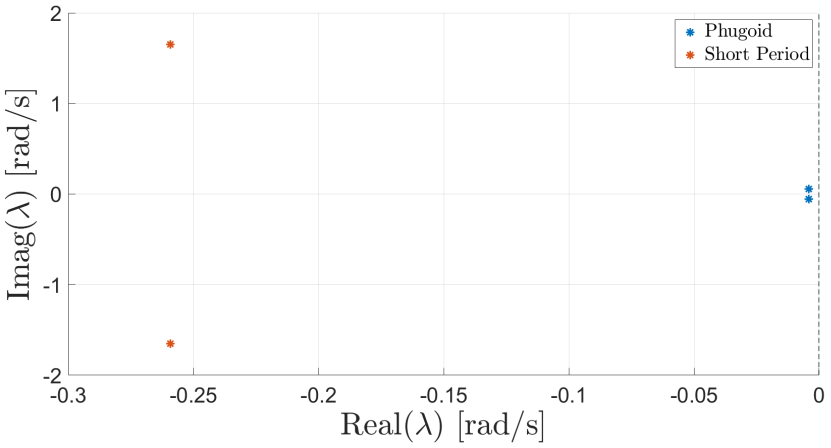

Figure 6.10: Map of longitudinal eigenvalues

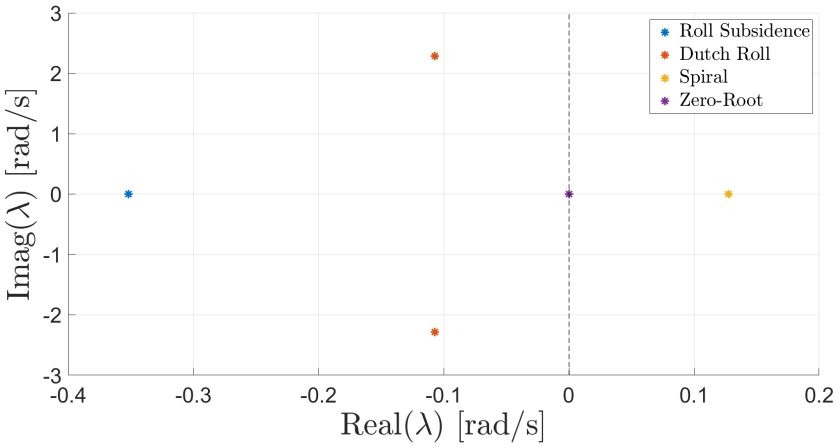

Figure 6.11: Map of lateral-directional eigenvalues

Unfortunately, no clear guidelines exist to assess the flying qualities of a low-weight fixed-wing eVTOL UAV. The evaluation of the aircraft flying qualities is therefore based on the United States Defense Specification document (MIL-STD [28]) for Class I Aircraft. The Class I Aircraft, namely small/light aircraft, has been considered the most appropriate category among the available ones. In addition, the flight phase category for cruise is B, namely non-terminal phase with gradual actions on controls.

According to the diagrams gathered in Appendix B, the flying quality level of each mode in cruise has been calculated and reported in Table 6.9.

Mode	FQ level
Phugoid (ξ)	1
Short Period (ω_n)	1
Short Period (ξ)	3
Roll Subsidence (τ)	2
Dutch Roll (ω_n)	1
Dutch Roll (ξ)	2
Dutch Roll ($\omega_n\xi$)	2
Spiral (T_2)	3

Table 6.9: Level of flying qualities in cruise

Implementing a control system would be appropriate to improve certain flying qualities. In particular, a longitudinal SAS would increase the short period damping ratio, and a lateral-directional SAS, also called a yaw damper, would increase the roll subsidence natural frequency and the dutch roll damping ratio. The longitudinal SAS affects the longitudinal static stability derivative ($C_{\mathcal{M}_{G_\alpha}}$) with the α-loop and the pitch damping derivative ($C_{\mathcal{M}_{G_q}}$) with the q-loop. The lateral-directional SAS affects the roll damping derivative ($C_{\mathcal{L}_{G_p}}$) with the p-loop and the yaw damping derivative ($C_{\mathcal{N}_{G_r}}$) with the r-loop. The typical architectures of such control systems are shown in Figure 6.12 and Figure 6.13. Nevertheless, the detailed modeling of sensors, filters and actuators, and the tuning of all PID controllers might be the focus of a future work.

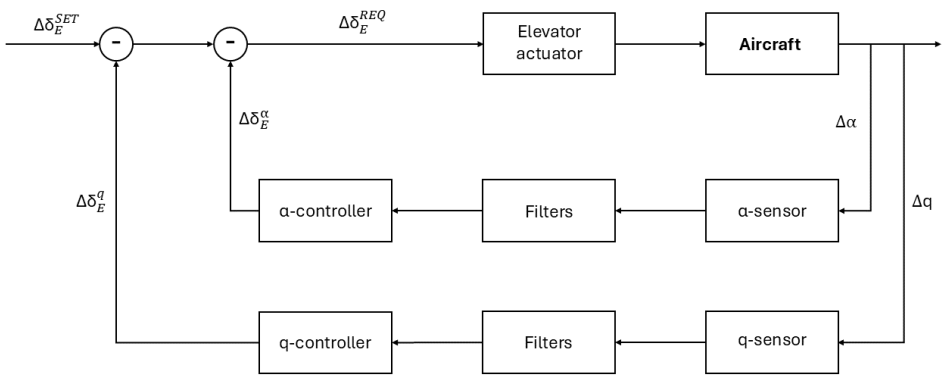

Figure 6.12: Architecture of a longitudinal Stability Augmentation System

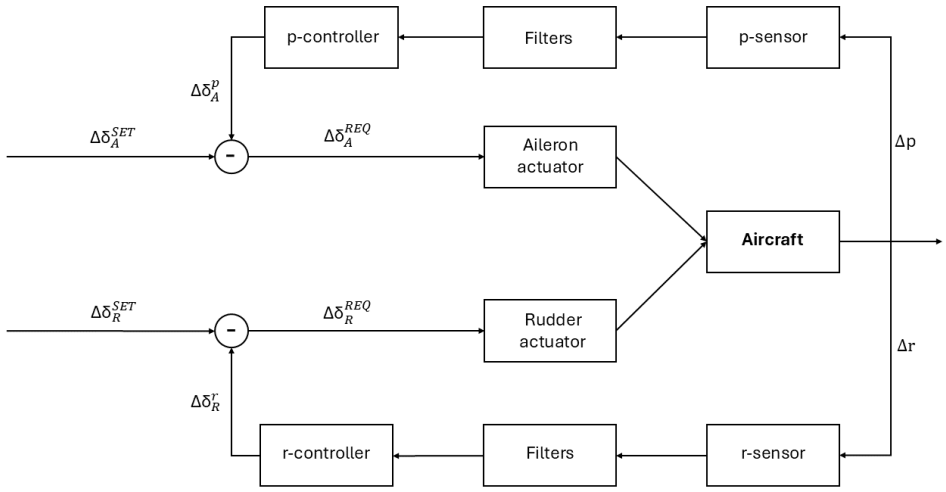

Figure 6.13: Architecture of a lateral-directional Stability Augmentation System

7 Aeroelastic analysis

This chapter concludes the technical development of the thesis with the preliminary investigation of the flutter phenomenon of the clamped wing. After choosing the constructive methodology and the materials, a simple beam model was created in MBDyn, and aeroelastic simulations were performed with DUST-MBDyn coupled software.

7.1. DUST - MBDyn coupling

DUST and MBDyn can be coupled using the Precise Code Interaction Coupling Environment (preCICE), a coupling library written in C++ that also offers bindings for C, Fortran, MATLAB, and Python. The communication scheme between the two software, which supports the exchange of information regarding position, orientation, velocity, angular velocity, force, and moment, is illustrated in Figure 7.1.

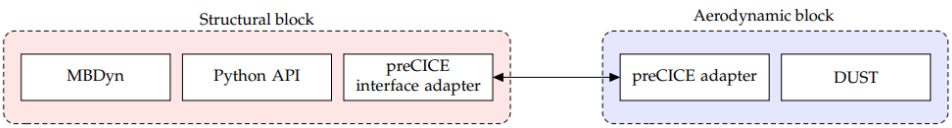

Figure 7.1: DUST-MBDyn communication scheme

A more precise description of the coupling can be found in [22].

7.2. Structural characteristics

The constructive methodology of fixed-wing UAVs can vary from the usage of low-performance, high-weight materials such as balsa wood to the implementation of composite materials and new-generation foams, as in modern airplanes. Figure 7.2 shows the traditional semi-monocoque internal structure of a wing, with spars, ribs, and thin skin.

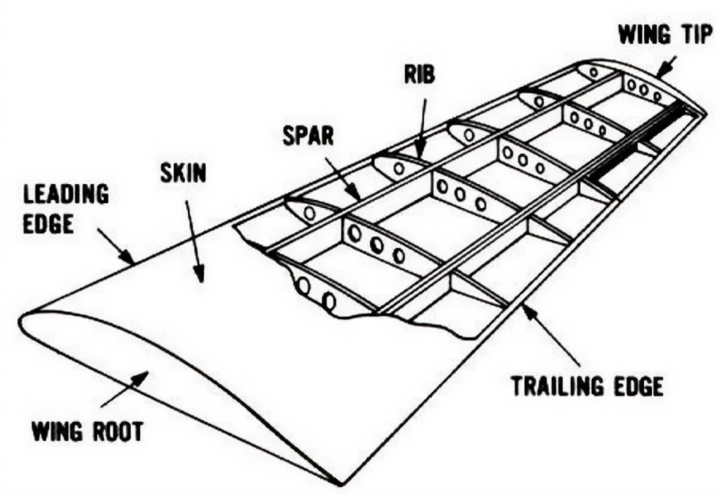

Figure 7.2: Traditional semi-monocoque wing structure

The Martian UAV must employ state-of-the-art materials like those produced by the European company Easy Composites [7]. Several datasheets have been investigated, and the following choices have been made for the wing:

- One spar located at 33% of the chord, made of a 25 mm external diameter (1.5 mm thickness) Carbon Fiber Tube.
- Eleven ribs, with 30 cm pitch, made of sandwich panels (Figure 7.3). The sandwich panel is composed by a 3.2 mm Cell Aramid Honeycomb and two 1 mm Carbon Fiber Prepreg plies per side.
- One 1 mm Carbon Fiber Prepreg ply and one 1 mm Rohacell ply for the external skin.

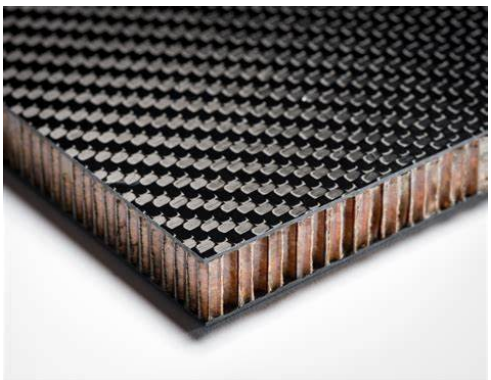

Figure 7.3: Sandwich panel

According to Evonik [8], the rohacell is an innovative lightweight foam with exceptional

mechanical performance for aerospace applications. Figure 7.4 provides an example of a combination between composite materials and rohacell.

Figure 7.4: Combination between carbon fiber composite material and rohacell foam

Considering the densities of all the materials reported in the datasheets, namely 0.125 km/m for the wing spar tube, 0.93 km/m^2 for the overall sandwich panel, and 0.26 kg/m^2 for the external skin, the wing mass amounts to 2.7 kg. When tolerances, glue, control surfaces, electric wires and servos are added, the final mass is a little less than the 3.6 kg hypothesized in the conceptual design mass breakdown. This might partially compensate for the increment of mass of the propulsive system. At this point, the semi-monocoque model of the airfoil with thin panels and lumped masses has been adopted to calculate the mass and the polar inertia per unit span and the axial, bending, shear, and torsional stiffness of the wing. Table 7.1 contains all the important structural information of the wing beam model, with the x-axis aligned along the beam from root to tip and the y-axis from the trailing edge towards the leading edge.

Parameter	**Symbol**	**Value**
Aerodynamic center position	P_{AC}	25% c
Elastic axis position	P_{EA}	33% c
Center of gravity position	P_{CG}	45% c
Mass per unit span	m	1.22 kg/m
Polar inertia per unit span	j_P	0.074 kg $\cdot$ m
Axial stiffness	EA	$2.3 \cdot 10^8$ N/m^2
Bending stiffness	EJ_{yy}	$1.5 \cdot 10^5$ N $\cdot$ m^2
Bending stiffness	EJ_{zz}	$2.2 \cdot 10^7$ N $\cdot$ m^2
Shear stiffness	GA_y	$1.2 \cdot 10^7$ N/m^2
Shear stiffness	GA_z	$1.4 \cdot 10^7$ N/m^2
Torsional stiffness	GJ_t	$3.3 \cdot 10^4$ N $\cdot$ m^2

Table 7.1: Wing structural characteristics

With the same approach, the structural characteristics of the horizontal tail and the vertical tail have been retrieved. However, considering the order of magnitude of the loads on Mars, they are not expected to undergo significant aeroelastic phenomena. The fuselage can be safely modeled as a rigid body.

7.3. Coupled model

The clamped wing illustrated in Figure 7.5 has been parametrically modeled with aerodynamic surface panels in DUST, with the same discretization used for the previous simulations, namely 30 panels chordwise and 50 panels spanwise. The structural model created in MBDyn consists of 5 structural nodes and 2 3-node beams along the elastic axis, representing a more refined discretization than the typical Goland's wing example at convergence [22].

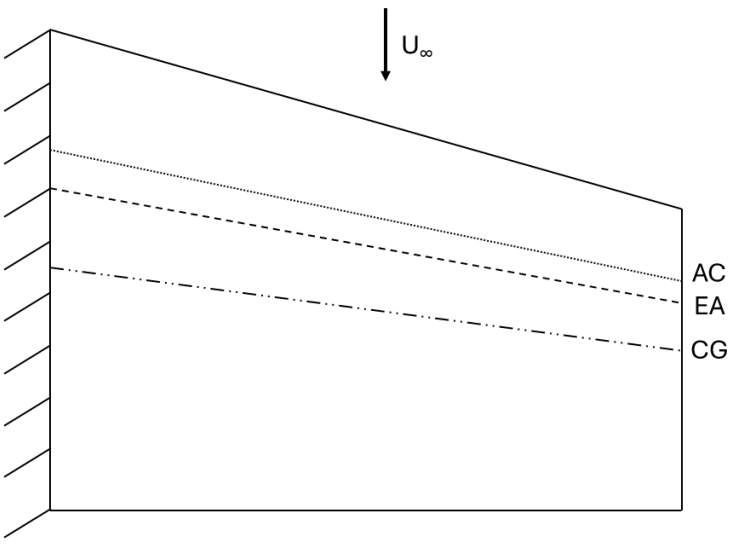

Figure 7.5: Clamped wing model

The time discretization has been set to 0.0005 s, with 300 time steps, up to 0.15 s with a fully developed particle wake. The simulations have been performed with an angle of attack of 3°, representing the cruising condition, and with several airspeeds, to depict the v-f and v-g diagrams.

7.4. Results

Firstly, the time history of the wingtip vertical displacement has been extracted, as shown in Figure 7.6. For all simulations, the oscillatory motion of the last structural node features a slightly damped behavior, with different amplitudes according to the increased airspeed.

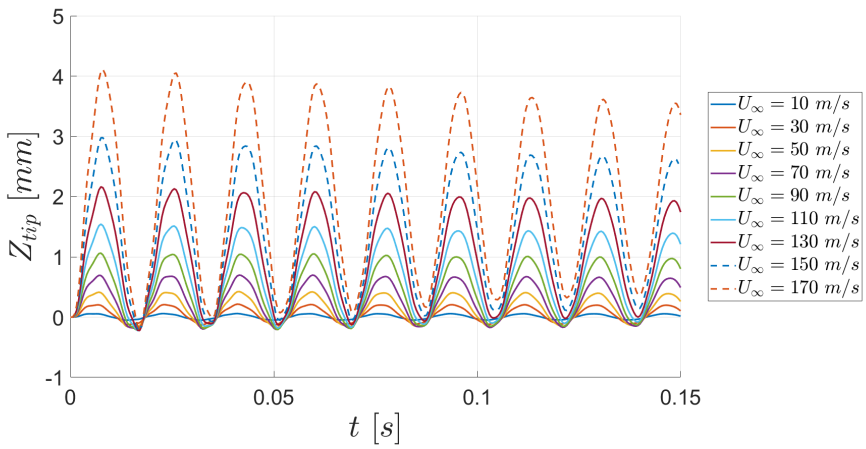

Figure 7.6: Wingtip vertical displacement vs Time

The MATLAB System Identification Toolbox has been used to retrieve the natural frequencies and the damping factors of both bending and torsion modes. In particular, an iddata object, which stores time-domain data, has been used to create an ARX model of the system. Figure 7.7 and Figure 7.8 respectively illustrate the trends of frequencies and damping factors with airspeed.

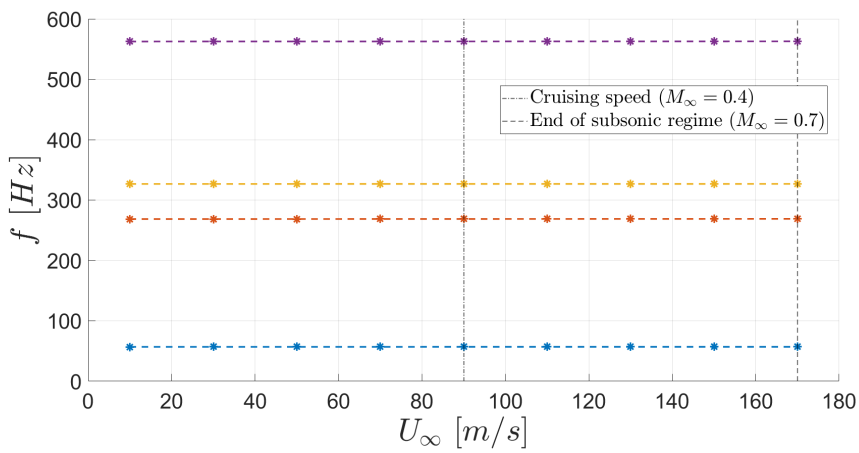

Figure 7.7: V-f diagram

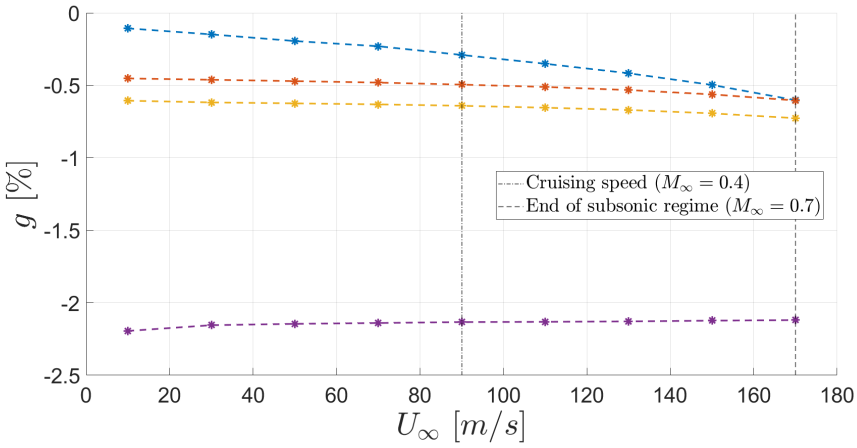

Figure 7.8: V-g diagram

It must be pointed out that only the subsonic regime has been investigated since DUST resorts to numerical corrections for compressibility. The results in the transonic regime cannot be deemed reliable, also considering the transonic dip of the flutter speed due to shock waves. Moreover, a little digression is needed to analyze the results better. Equation 7.1 represents the governing equation of a generic system subject to pitch and plunge motions with Theodorsen quasi-steady aerodynamics.

$$\left(\underline{\underline{M}} - \frac{q_\infty}{U_\infty^2}\underline{\underline{M_A}}\right)\underline{\ddot{x}}(t) \;+\; \left(\underline{\underline{C}} - \frac{q_\infty}{U_\infty}\underline{\underline{C_A}}\right)\underline{\dot{x}}(t) \;+\; \left(\underline{\underline{K}} - q_\infty\underline{\underline{K_A}}\right)\underline{x}(t) \;=\; \underline{0} \tag{7.1}$$

where $\underline{\underline{M}}$, $\underline{\underline{C}}$, $\underline{\underline{K}}$ are the mass, damping, and stiffness matrices of the structural part of the system, $\underline{\underline{M_A}}$, $\underline{\underline{C_A}}$, $\underline{\underline{K_A}}$ are the aerodynamic mass, damping, and stiffness matrices. The vector $\underline{x}$ contains the degrees of freedom of the system. The aerodynamic contributions are proportional to either the dynamic pressure or a combination of dynamic pressure and airspeed. Considering the same drone in cruising condition on Earth and on Mars, Table 7.2 has been created, with some relevant parameters, to get some insights about the aerodynamic contributions to the aeroelastic problem.

Parameter	Symbol	Value on Earth	Value on Mars
UAV mass [kg]	M	20	20
Gravity acceleration [m/s^2]	g	9.81	3.72
UAV weight [N]	W	200	75
Density [kg/m^3]	ρ	1.225	0.0132
Dynamic pressure [Pa]	q_∞	**130**	**50**
Airspeed [m/s]	U_∞	15	90
- [Pa/(m/s)]	$\frac{q_\infty}{U_\infty}$	**9**	**0.6**
- [Pa/(m/s)^2]	$\frac{q_\infty}{U_\infty^2}$	**0.6**	**0.006**

Table 7.2: Comparison between operative conditions on Earth and on Mars

On Mars, the contribution of the aerodynamic stiffness is about 3 times lower than on Earth, the contribution of the aerodynamic damping is approximately 15 times lower, and the contribution of the aerodynamic inertia is 100 times lower. This explains the almost negligible variation of frequencies and damping factors in the previous diagrams, leading to a flutter-free flight envelope.

8 | Conclusions and future developments

This research highlighted the challenges and the opportunities associated with the design of a fixed-wing eVTOL UAV for operations in the Martian atmosphere.

Firstly, the rotors were sized to allow the helicopter, transition, and airplane modes, considering several limitations and adopting optimized airfoils and blade shape. Secondly, all flight phases were thoroughly analyzed in terms of aerodynamic loads and trim settings, with particular attention paid to the loads generated by the rotors and the wing in cruise.

Afterwards, the battery pack and the electric motors had to be modified to comply with the shaft power and the torque requirements in different flight phases, leading to a 4.6 kg increased mass compared to the initial estimation. The distance covered in-flight dropped to 70 km, still, a successful outcome, while the maximum take-off mass of the drone, initially set to 20 kg, could only be achieved with the employment of state-of-the-art materials, such as carbon fiber composites, rohacell foam and sandwich panels, and miniaturized lightweight electronics.

Then, the estimation of all stability derivatives and the calculation of the flying quality levels confirmed that the UAV is suitable for flight in the Martian environment. Nevertheless, the implementation of some control systems might enhance flight capabilities.

Lastly, an aeroelastic analysis proved that the wing of the drone, built with a specific constructive method and with innovative materials, was not prone to flutter phenomenon. Experimental tests in the wind tunnel, with an accurate structural model and a precise aerodynamic similarity, might verify the results.

In conclusion, there are multiple challenges to overcome but the research carried out in this work and in the previous ones can confirm that the future missions on the Red Planet can exploit this new technology of drones. This project may still be improved with the creation of a detailed CAD model, an in-depth study of all junctions, and a FEM analysis. In addition, the control systems may be tuned and applied to the aircraft dynamics.

Bibliography

[1] Archer. Archer Midnight, 2024. URL https://www.archer.com/. Website.

[2] M. Bertani. Preliminary design of a fixed wing VTOL UAV for Martian flight. Master's thesis, Politecnico di Milano, 2023.

[3] CRG. Li-Metal cells, 2024. URL https://www.crgrp.com/. Website.

[4] DAER, Politecnico di Milano. MBDyn, 2001. URL https://www.mbdyn.org. Software.

[5] DAER, Politecnico di Milano. DUST, 2017. URL https://www.dust.polimi.it. Software.

[6] Dassault Systèmes. SolidWorks, 1995. URL https://www.solidworks.com. Software.

[7] easycomposites. The European home of advanced composites, 2024. URL https://www.easycomposites.eu/. Website.

[8] Evonik. Foams for aerospace applications, 2024. URL https://performance-foams.evonik.com/en. Website.

[9] C. Geuzaine and J.-F. Remacle. Gmsh, 2003. URL https://gmsh.info/. Software.

[10] D. Granata, A. Savino, and A. Zanotti. Numerical Evaluation of Aircraft Aerodynamic Static and Dynamic Stability Derivatives by a Mid-Fidelity Approach. *Aerospace*, 11, 03 2024. doi: 10.3390/aerospace11030213.

[11] A. Guardone et al. SU2, 2012. URL https://su2code.github.io/. Software.

[12] Joby Aviation. Joby Aviation eVTOL UAV, 2024. URL https://www.jobyaviation.com/. Website.

[13] W. Johnson. CAMRAD - A Comprehensive Analytical Model of Rotorcraft Aerodynamics and Dynamics, 1994. URL https://api.semanticscholar.org/CorpusID:109453171. Accessed via Semantic Scholar.

[14] W. Johnson, S. Withrow, L. Young, C. Malpica, W. Koning, W. Kuang, M. Fehler, A. Chan, A. Datta, C. Chi, R. Lumba, D. Escobar, and J. Balaram. Mars Science Helicopter Conceptual Design. Technical report, NASA Ames Research Center, 03 2020.

[15] Y. C. Krishna and T. Venkatesh. Numerical investigation of aerodynamically efficient wing tip-mounted propeller configuration using coupled RANS–BEM approach. *Aircraft Engineering and Aerospace Technology*, 95, 02 2023. doi: 10.1108/AEAT-09-2022-0254.

[16] MathWorks. MATLAB, 1984. URL `https://it.mathworks.com/products/matlab.html`. Software.

[17] S. Maurice, B. Chide, N. Murdoch, R. Lorenz, D. Mimoun, R. Wiens, A. Stott, X. Jacob, T. Bertrand, F. Montmessin, N. Lanza, C. Álvarez Llamas, S. Angel, M. Aung, J. Balaram, O. Beyssac, A. Cousin, G. Delory, O. Forni, and P. Willis. In situ recording of mars soundscape. *Nature*, 605, 05 2022. doi: 10.1038/s41586-022-04679-0.

[18] R. A. McDonald and J. R. Gloudemans. OpenVSP, 2012. URL `https://openvsp.org/`. Software.

[19] N. Moreschi. Reynolds and Mach number effects on the aerodynamics and design of airfoils for the Martian atmosphere. Master's thesis, Politecnico di Milano, 2023.

[20] NASA. Ingenuity Mars Helicopter, 2024. URL `https://science.nasa.gov/mission/mars-2020-perseverance/ingenuity-mars-helicopter/`. Website.

[21] NASA. Mars Atmospheric Model, 2024. URL `https://www.grc.nasa.gov/www/k-12/airplane/atmosmrm.html`. Website.

[22] A. Savino, A. Cocco, A. Zanotti, M. Tugnoli, P. Masarati, and V. Muscarello. Coupling Mid-Fidelity Aerodynamics and Multibody Dynamics for the Aeroelastic Analysis of Rotary-Wing Vehicles. *Energies*, 14(21), 2021. ISSN 1996-1073. doi: 10.3390/en14216979. URL `https://www.mdpi.com/1996-1073/14/21/6979`.

[23] Sensenich Propellers. Electric variable pitch hub, 2024. URL `https://www.sensenich.com/`. Website.

[24] Sion Power. Licerion cells, 2024. URL `https://sionpower.com/`. Website.

[25] W. Z. Stepniewski. *Rotary-wing aerodynamics. Volume 1: Basic theories of rotor aerodynamics (with application to helicopters)*. NASA, 1979.

[26] T-MOTOR. Electric motors, 2024. URL `https://store.tmotor.com/`. Website.

[27] M. Tugnoli, D. Montagnani, M. Syal, G. Droandi, and A. Zanotti. Mid-fidelity approach to aerodynamic simulations of unconventional VTOL aircraft configurations. *Aerospace Science and Technology*, 115:106804, 2021. ISSN 1270-9638. doi: https://doi.org/10.1016/j.ast.2021.106804. URL `https://www.sciencedirect.com/science/article/pii/S127096382100314X`.

[28] U.S. Department of Defense. MIL-F-8785C, 1980.

[29] L. Viterna and D. Janetzke. Theoretical and experimental power from large horizontal-axis wind turbines. *NASA Technical Memorandum*, 10 1982.

[30] S. Withrow, W. Johnson, L. Young, H. Cummings, J. Balaram, and T. Tzanetos. An Advanced Mars Helicopter Design. Technical report, NASA Ames Research Center, 11 2020.

[31] A. Zanotti, A. Savino, M. Palazzi, M. Tugnoli, and V. Muscarello. Assessment of a Mid-Fidelity Numerical Approach for the Investigation of Tiltrotor Aerodynamics. *Applied Sciences*, 11(8), 2021. ISSN 2076-3417. doi: 10.3390/app11083385. URL `https://www.mdpi.com/2076-3417/11/8/3385`.

A | Empirical extension of lift, drag, and pitching moment coefficients

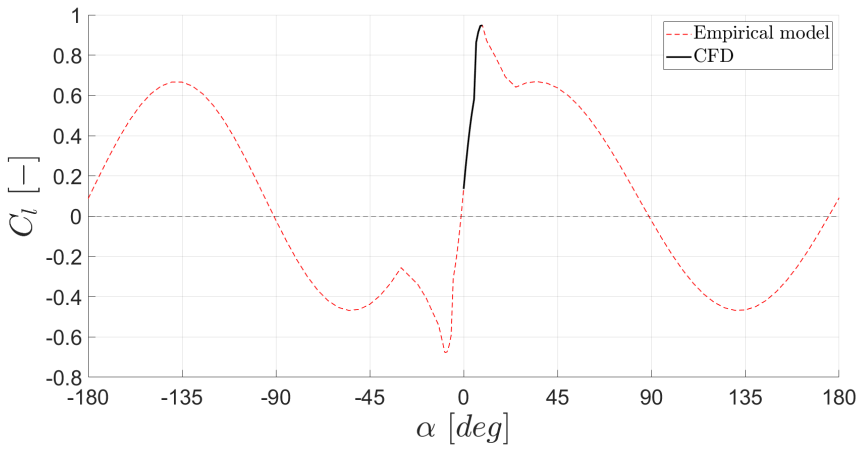

Figure A.1: Lift coefficient for blade mid airfoil

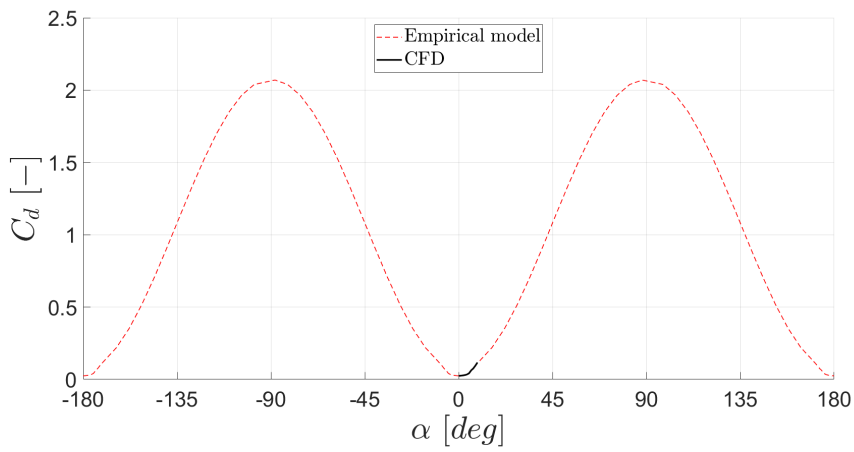

Figure A.2: Drag coefficient for blade mid airfoil

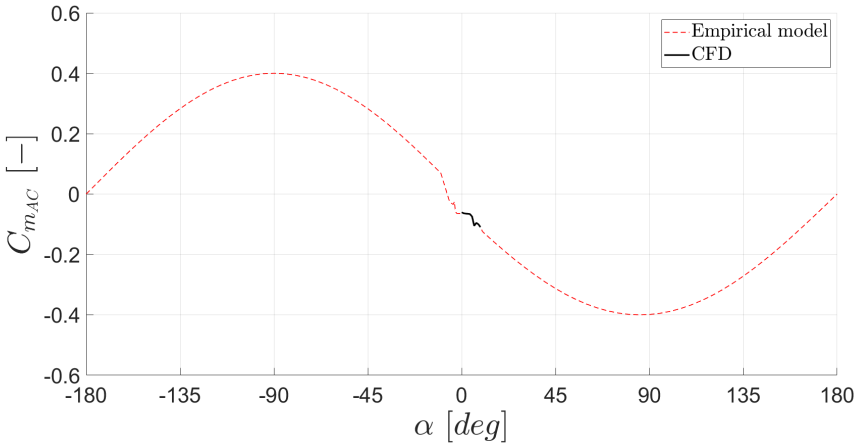

Figure A.3: Pitching moment coefficient for blade mid airfoil

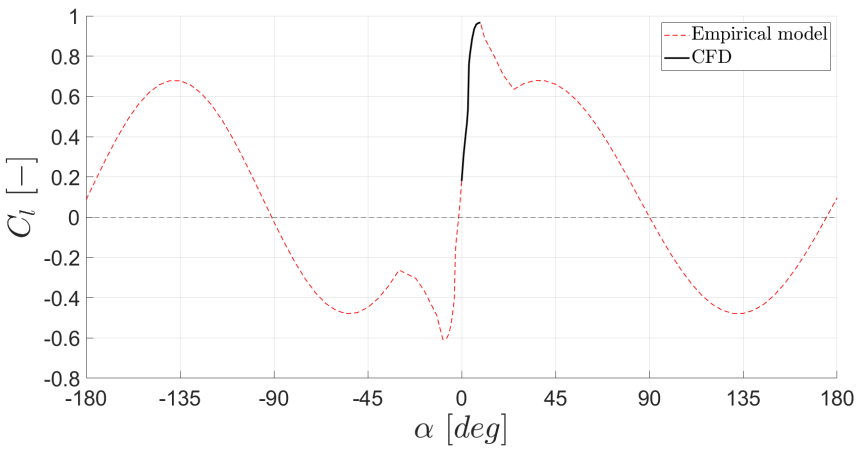

Figure A.4: Lift coefficient for blade tip airfoil

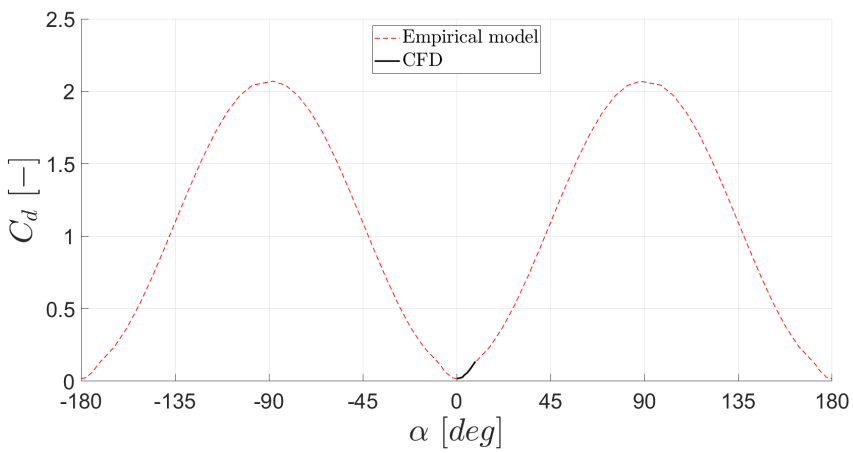

Figure A.5: Drag coefficient for blade tip airfoil

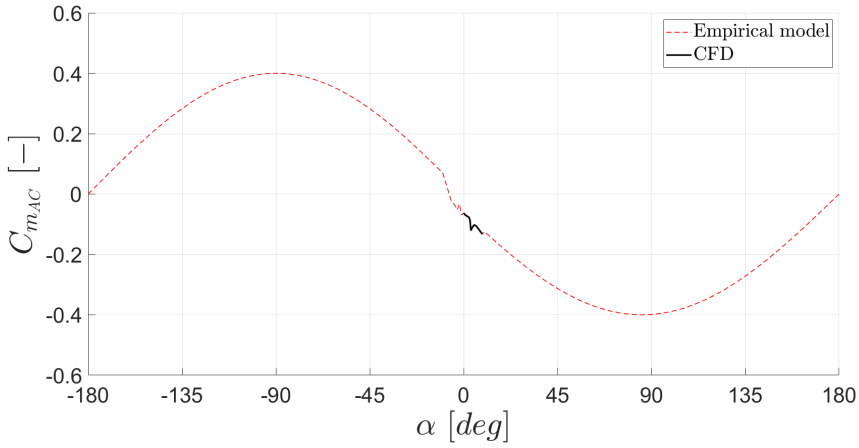

Figure A.6: Pitching moment coefficient for blade tip airfoil

B | MIL-STD - Flying qualities

a. Level 1 ----- ζ_p at least 0.04

b. Level 2 ----- ζ_p at least 0

c. Level 3 ----- T_2 at least 55 seconds

Figure B.1: Phugoid - damping ratio and time-to-double [28]

Level	Category A and C Flight Phases		Category B Flight Phases	
	Minimum	Maximum	Minimum	Maximum
1	0.35	1.30	0.30	2.00
2	0.25	2.00	0.20	2.00
3	0.15*	-	0.15*	-

Figure B.2: Short Period - damping ratio [28]

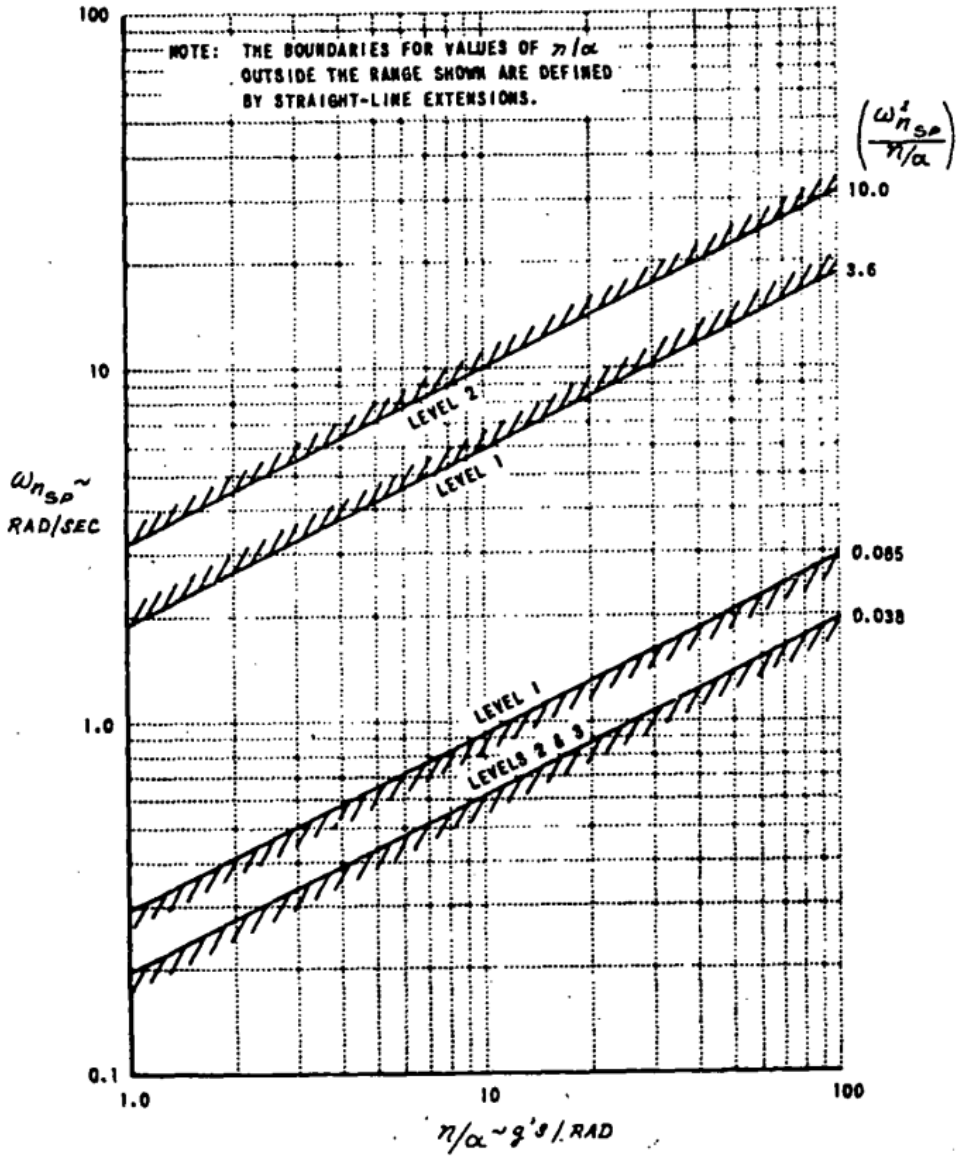

Figure B.3: Short Period - natural frequency [28]

Flight Phase Category	Class	Level 1	Level 2	Level 3
A	I, IV	1.0	1.4	
	II, III	1.4	3.0	
B	All	1.4	3.0	10
C	I, II-C, IV	1.0	1.4	
	II-L, III	1.4	3.0	

Figure B.4: Roll Subsidence - time constant [28]

Level	Flight Phase Category	Class	Min ζ_d*	Min $\zeta_d\omega_{n_d}$* rad/sec.	Min ω_{n_d} rad/sec.
1	A (CO and GA)	IV	0.4	-	1.0
	A	I, IV	0.19	0.35	1.0
		II, III	0.19	0.35	0.4**
	B	All	0.08	0.15	0.4**
	C	I, II-C, IV	0.08	0.15	1.0
		II-L, III	0.08	0.10	0.4**
2	All	All	0.02	0.05	0.4**
3	All	All	0	-	0.4**

Figure B.5: Dutch Roll - natural frequency and damping ratio [28]

Flight Phase Category	Level 1	Level 2	Level 3
A & C	12 sec	8 sec	4 sec
B	20 sec	8 sec	4 sec

Figure B.6: Spiral - time-to-double [28]

List of Figures

1.1 Ingenuity Mars Helicopter [20] 1
1.2 Mars 2
1.3 Mars topographic map 3
1.4 Mars main topographic features 3
1.5 Trends of atmospheric variables 5
1.6 Airfoil optimized for Re = 10,000 and Ma = 0.6 - shape 7
1.7 Airfoil optimized for Re = 10,000 and Ma = 0.6 - aerodynamic parameters 7
1.8 Preliminary configuration of the drone 8

2.1 3D CAD model 12
2.2 Technical drawings 13
2.3 STEP file curves 14
2.4 Full model surface mesh 15
2.5 Wing surface mesh 15

3.1 Blade ideal lift coefficient vs Spanwise location 19
3.2 Blade ideal twist angle vs Spanwise location 20
3.3 Blade planform 21
3.4 Blade chord distribution vs Spanwise location 22
3.5 Blade Reynolds and Mach number distribution vs Spanwise location 22
3.6 Blade optimized airfoils 23
3.7 Lift coefficient for blade root airfoil 24
3.8 Drag coefficient for blade root airfoil 24
3.9 Pitching moment coefficient for blade root airfoil 25
3.10 Rotor thrust vs Number of revolutions 26
3.11 Rotor torque vs Number of revolutions 26
3.12 Rotor shaft power vs Number of revolutions 27
3.13 Rotor average thrust vs Number of time steps per revolution 27
3.14 Rotor average torque vs Number of time steps per revolution 28
3.15 Rotor average shaft power vs Number of time steps per revolution 28

3.16 Rotor average thrust vs Number of lifting line elements per blade 29
3.17 Rotor average torque vs Number of lifting line elements per blade 29
3.18 Rotor average shaft power vs Number of lifting line elements per blade . . 29
3.19 Blade lift coefficient vs Spanwise location 30
3.20 Rotor pressure and wake particles at hovering at convergence 31
3.21 Rotor singularity intensity and wake particles at hovering at convergence . 31
3.22 Rotor wake evolution at hovering - lateral view 32
3.23 Blade advance angle and ideal twist angle vs Spanwise location 33
3.24 Propeller thrust coefficient vs Advance ratio (4 propellers) 34
3.25 Propeller thrust coefficient vs Advance ratio (2 propellers) 34
3.26 Propeller torque coefficient vs Advance ratio 35
3.27 Propeller shaft power coefficient vs Advance ratio 35
3.28 Propeller efficiency vs Advance ratio 36
3.29 Archer Midnight in different flight phases [1] 36
3.30 Rotor max RPM vs True airspeed 37
3.31 Rotor collective pitch angle vs Rotor inclination angle 37
3.32 Rotors required vertical thrust and Drone lift vs True airspeed 38
3.33 Rear rotor required and available vertical thrust vs True airspeed 39
3.34 Rear rotor wake evolution in transition at 30 m/s - lateral view 39
3.35 Rear rotor wake evolution in transition at 30 m/s - top view 40
3.36 Rotor inclination angle vs True airspeed 41
3.37 Front rotor required and available vertical thrust vs True airspeed 41
3.38 Front rotor wake evolution in transition at 30 m/s - lateral view 42
3.39 Front rotor wake evolution in transition at 30 m/s - top view 42
3.40 Front rotor wake evolution in cruise at 90 m/s - lateral view 43
3.41 Front rotor in cruise at 90 m/s - front view 43
3.42 Front rotor available horizontal thrust and Drone drag vs True airspeed (4 rotors) 44
3.43 Front rotor available horizontal thrust and Drone drag vs True airspeed (2 rotors) 44
3.44 Rotor inclination angle vs True airspeed 45

4.1 3D CAD model with rotors 47
4.2 Technical drawings with rotors 48
4.3 Electric variable pitch hub 49
4.4 Joby Aviation eVTOL rotor configuration [12] 49
4.5 Vertical equilibrium of forces vs True airspeed 50

4.6 Horizontal equilibrium of forces vs True airspeed 51
4.7 Rotor torque vs True airspeed 51
4.8 Overall shaft power vs True airspeed 52
4.9 Z-direction velocity flow field - front view 53
4.10 Wing surface velocity distribution 53
4.11 Wing pressure coefficient distribution 54
4.12 Blade non-dimensional normal force - right side, front view 55
4.13 Blade non-dimensional normal force vs Azimuth angle - right side, front view 56
4.14 Blade non-dimensional normal force vs Spanwise location - right side, front view 56
4.15 Full model in transition at 60 m/s - rotor wake and singularity intensity distribution 57
4.16 Blade non-dimensional normal force - right rear side, front view 57
4.17 Blade non-dimensional normal force - right front side, front view 58
4.18 Full model at hovering - rotor wake and singularity intensity distribution . 58
4.19 Z-direction Mach flow field - front view 59

5.1 Original motor torque curves 63
5.2 New motor torque curves 64
5.3 C-rate performance. Charge: C/2, 4.5 V. Discharge: 2.7 V [3] 65
5.4 Temperature performance. Charge: C/2, 4.5 V. Discharge: C/2, 2.7 V [3] . 66
5.5 Life cycle performance. Room temperature. Charge: C/5, 4.5 V. Discharge: C/5, 2.7 V [3] 67

6.1 Body reference frame with sign conventions 70
6.2 Static angle of attack simulations 71
6.3 Static angle of sideslip simulations 72
6.4 Roll oscillation 74
6.5 Dynamic roll simulations 74
6.6 Pitch oscillation 76
6.7 Dynamic pitch simulations 76
6.8 Yaw oscillation 78
6.9 Dynamic yaw simulations 78
6.10 Map of longitudinal eigenvalues 82
6.11 Map of lateral-directional eigenvalues 82
6.12 Architecture of a longitudinal Stability Augmentation System 83
6.13 Architecture of a lateral-directional Stability Augmentation System 84

7.1 DUST-MBDyn communication scheme 85
7.2 Traditional semi-monocoque wing structure 86
7.3 Sandwich panel 86
7.4 Combination between carbon fiber composite material and rohacell foam . 87
7.5 Clamped wing model 88
7.6 Wingtip vertical displacement vs Time 89
7.7 V-f diagram 89
7.8 V-g diagram 90

A.1 Lift coefficient for blade mid airfoil 99
A.2 Drag coefficient for blade mid airfoil 99
A.3 Pitching moment coefficient for blade mid airfoil 100
A.4 Lift coefficient for blade tip airfoil 100
A.5 Drag coefficient for blade tip airfoil 100
A.6 Pitching moment coefficient for blade tip airfoil 101

B.1 Phugoid - damping ratio and time-to-double [28] 103
B.2 Short Period - damping ratio [28] 103
B.3 Short Period - natural frequency [28] 104
B.4 Roll Subsidence - time constant [28] 105
B.5 Dutch Roll - natural frequency and damping ratio [28] 105
B.6 Spiral - time-to-double [28] 105

List of Tables

1.1 Performance requirements 6
1.2 Design specifications 6

2.1 Mesh elements 14

3.1 Thrust requirements 17
3.2 Blade airfoil characteristics 23
3.3 Rotor parameters at hovering at convergence 30

4.1 Trim settings 50
4.2 Front rotor variation of thrust and shaft power 54

5.1 Technical specifications of Sion Power Li-Metal cell in ideal operative conditions 61
5.2 Technical specifications of T-MOTOR AT2826 3D F3A Fixed Wing Long Shaft Brushless Motor-KV900 62
5.3 Technical specifications of T-MOTOR MN705-S IP45 Navigator Type UAV Multi-Motor KV260 -2PCS/SET 63
5.4 Technical specifications of CRG Li-Metal cell in ideal operative conditions . 65
5.5 Technical specifications of CRG Li-Metal cell in Mars operative conditions 66
5.6 Flight phase shaft power and energy requirements 68

6.1 Stability derivative simulation settings 71
6.2 Static angle of attack stability derivatives 72
6.3 Static angle of sideslip stability derivatives 73
6.4 Dynamic roll stability derivatives 75
6.5 Dynamic pitch stability derivatives 77
6.6 Dynamic yaw stability derivatives 79
6.7 Vertical plunge stability derivatives 79
6.8 Lateral plunge stability derivatives 80
6.9 Level of flying qualities in cruise 83

7.1 Wing structural characteristics 87
7.2 Comparison between operative conditions on Earth and on Mars 91

List of Symbols

Variable	Description	SI unit
a_r	blade airfoil lift curve slope	1/rad
b	wingspan	m
C	rotor torque or cell nominal capacity	Nm or Ah
C_N	blade normal force coefficient	-
C_P	rotor shaft power coefficient	-
C_Q	rotor torque coefficient	-
C_T	rotor thrust coefficient	-
C_l	2D blade lift coefficient	-
$\overline{C_l}$	2D blade average lift coefficient	-
C_d	2D blade drag coefficient	-
C_m	electric motor torque	Nm
$C_{m_{AC}}$	2D blade pitching moment coefficient	-
C_{con}^{max}	cell max continuous C-rate	1/h
C_{180}^{max}	cell max C-rate (180s)	1/h
c	wing chord	m
D	rotor diameter or drag	m or N
EA	wing axial stiffness	N/m^2
EJ_{yy}	wing in-plane bending stiffness	Nm^2
EJ_{zz}	wing out-of-plane bending stiffness	Nm^2
e^*	cell gravimetric energy	Wh/kg
FM	rotor figure of merit	%
f	wing mode frequency	Hz
GA_y	wing out-of-plane shear stiffness	N/m^2
GA_z	wing in-plane shear stiffness	N/m^2
GJ_t	wing torsional stiffness	Nm^2
g	gravity acceleration or wing mode damping factor	m/s^2 or -
i	current	A
i^{max}	electric motor max current (180s)	A

Variable	Description	SI unit
$\boldsymbol{J}$	propeller advance ratio	-
$\boldsymbol{J_{xx}}$	inertia in roll	Nm^2
$\boldsymbol{J_{yy}}$	inertia in pitch	Nm^2
$\boldsymbol{J_{zz}}$	inertia in yaw	Nm^2
$\boldsymbol{j_P}$	wing polar inertia per unit span	kgm
$\boldsymbol{k}$	electric motor constant	Nm/A
$\boldsymbol{L}$	lift	N
$\boldsymbol{\mathcal{L}}$	rolling moment	Nm
$\boldsymbol{M}$	mass	kg
$\boldsymbol{Ma}$	Mach number	-
$\boldsymbol{\mathcal{M}}$	pitching moment	Nm
$\boldsymbol{m}$	wing mass per unit span	kg/m
$\boldsymbol{N_b}$	number of rotor blades	-
$\boldsymbol{N_{lle}}$	number of lifting line elements	-
$\boldsymbol{N_{rev}}$	number of revolutions	-
$\boldsymbol{N_{ts}}$	number of time steps	-
$\boldsymbol{\mathcal{N}}$	yawing moment	Nm
$\boldsymbol{n}$	revolutions per second	1/s
$\boldsymbol{P_{AC}}$	wing aerodynamic center position	%c
$\boldsymbol{P_{CG}}$	wing center of gravity position	%c
$\boldsymbol{P_{EA}}$	wing elastic axis position	%c
$\boldsymbol{P_a}$	rotor available power	W
$\boldsymbol{P_s}$	rotor shaft power	W
$\boldsymbol{P_s^{max}}$	electric motor max shaft power (180s)	W
$\boldsymbol{p}$	roll rate	rad/s
$\boldsymbol{p^*}$	cell gravimetric power	W/kg
$\boldsymbol{Q}$	rotor torque	Nm
$\boldsymbol{q}$	pitch rate	rad/s
$\boldsymbol{q_\infty}$	dynamic pressure	Pa
$\boldsymbol{R}$	rotor radius	m
$\boldsymbol{ROC}$	rate of climb	m/s
$\boldsymbol{RPM}$	revolutions per minute	1/min
$\boldsymbol{Re}$	Reynolds number	-
$\boldsymbol{R_a}$	electric motor internal resistance	Ω
$\boldsymbol{r}$	yaw rate	rad/s
$\boldsymbol{r_e}$	rotor effective radius	-

Variable	Description	SI unit
r_i	rotor cutout radius	-
S	side force or wing surface	N or m^2
T	rotor thrust	N
T_H	rotor horizontal thrust	N
T_V	rotor vertical thrust	N
U_0	true airspeed (reference condition)	m/s
U_∞	true airspeed	m/s
V	cell nominal voltage	V
V_T	blade tip speed	m/s
V_a	electric motor input voltage	V
W	weight	N
X	longitudinal force	N
Y	lateral force	N
Z	vertical force	N
Z_{tip}	wingtip vertical displacement	m
α	angle of attack	deg
β	blade advance angle or angle of sideslip	deg
δ	control surface deflection angle	deg
η	propeller efficiency	-
θ	blade twist angle or pitch angle	deg
λ	pole real part	rad/s
ξ	damping ratio	-
ρ	air density	kg/m^3
σ	rotor solidity	-
τ	time constant	s
ϕ	rotor inclination angle or roll angle	deg
ψ	blade azimuth angle or yaw angle	deg
ω	angular speed or natural frequency or cell mass factor	rad/s or -